TECHNISCHE UNIVERSITÄT MÜNCHEN
Physik-Department

A novel ion chamber technology for quality assurance in external beam radiotherapy

Michele Togno

Vollständiger Abdruck der von der Fakultät für Physik der Technischen Universität München zur Erlangung des akademischen Grades eines

Doktors der Naturwissenschaften (Dr. rer. nat.)

genehmigten Dissertation.

Vorsitzender:	Univ.-Prof. Dr. Martin Zacharias
Prüfer der Dissertation:	
	1. Univ.-Prof. Dr. Jan J. Wilkens
	2. Univ.-Prof. Dr. Franz Pfeiffer

Die Dissertation wurde am 15.05.2017 bei der Technischen Universität München eingereicht und durch die Fakultät für Physik am 10.07.2017 angenommen

PHYSIK-DEPARTMENT

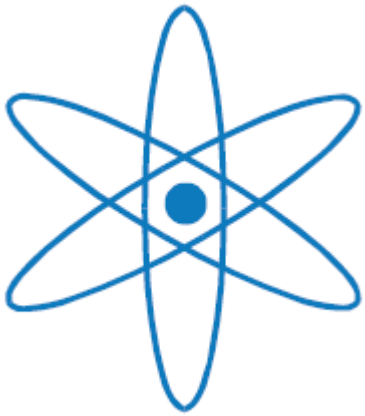

A NOVEL ION CHAMBER TECHNOLOGY FOR QUALITY ASSURANCE IN EXTERNAL BEAM RADIOTHERAPY

Dissertation
von

Michele Togno

− April 2017 −

TECHNISCHE UNIVERSITÄT MÜNCHEN

Abstract

Radiation therapy with external beams aims to cure cancer by means of dose deposition in the patient body. The number of cancer patients that could benefit from a radiation treatment is expected to grow significantly in the coming years. A number of different techniques have been recently developed to increase the precision of dose delivery to the target and to minimize the effects of the treatment on healthy organs. Examples of such innovative techniques include stereotactic radiosurgery (SRS) and intensity-modulated proton therapy (IMPT) with scanning pencil beams. As with the accuracy of the treatment, the complexity of the radiation delivery and of the machines themselves is also increased. Thus, high-level quality assurance is required to ensure the consistency of medical prescription to the patient and to improve the dosimetric and geometric accuracy of dose delivery. Moreover, quality assurance procedures play a fundamental role in decreasing the likelihood of accidents and errors, and they are a precondition for intercomparisons of data on a large scale among different radiotherapy centers.

A number of different devices have been developed to fulfill the requirements of fast and reliable machine quality assurance and patient quality assurance in external beam radiotherapy. However, the challenges introduced by new treatment practices necessitate the further and continuous development of such devices. The aim of this thesis is to investigate the suitability of an innovative technology to quality assurance applications in complex radiotherapy techniques.

The investigated technology is based on ionization chambers, which are arranged in a grid in the final detector design in order to cover a 2D surface. The choice of ionization chambers was driven by their intrinsic properties, such as energy independence, radiation hardness and possibility to measure absorbed dose to water. The main desired characteristics of the technology, besides those typical of standard dosimeters, are high sampling resolution and low sensitivity dependence on dose rate/dose per pulse. These features are essential to

properly resolving dose distributions, which are delivered with time-varying parameters, high dose rate/dose per pulse, and steep gradients.

The development process is divided into three major phases. In each phase, a detector prototype is built and tested under different types of radiation. The first prototype is tested mainly with continuous gamma radiation in order to optimize performances and design through a step-by-step approach. The second prototype is built to consolidate the achievements made using the first prototype, and it comes with new frontend electronics and a design which allows for independent and reliable tests. The detector is deeply tested with clinical MV X-rays at different beam qualities and dose rates, with clinical proton beams at different energies and currents. It is also benchmarked to state of the art detectors. Moreover, performances of the detector are evaluated in a clinical environment for the sake of machine quality assurance controls (e.g. output factors, beam profiling, depth dose curves…) and pre-treatment patient plan verification. Thanks to the encouraging results of this research phase, a third prototype is designed and the proof of concept started with preliminary validation in clinical proton beams.

The investigated technology is proven to have great potential for applications in radiation dosimetry. It is demonstrated to be a valuable option in addressing the need for innovative tools that arises from the increasing complexity and effectiveness of modern radiotherapy techniques. Furthermore, the recommendations of international dosimetric protocols can also be fulfilled. Nevertheless, some improvements and additional developments are required, and these are identified in three main research branches, as described in the conclusion of the present work.

Zusammenfassung

Perkutane Strahlentherapie dient der Behandlung von Krebs durch Bestrahlung des Patientenkörpers mit hochenergetischer Strahlung, wobei Dosis im Tumor deponiert wird. Die Anzahl der Krebspatienten, welche von dieser Behandlungsmethode profitieren, wird in den nächsten Jahren stark steigen. Verschiedenste Verfahren wurden in letzter Zeit entwickelt, um einerseits die Genauigkeit der Dosisverteilung im Zielvolumen zu verbessern und andererseits die Nebenwirkungen auf gesundes Gewebe und Risikoorgane zu minimieren. Einige Beispiele für diese neuen Behandlungstechniken sind *stereotaktische Radiochirurgie* (SRS, stereotactic radiosurgery) und *Intensitätsmoduliertes Protonenbeam-Scanning* (IMPT, intensity modulated proton therapy with scanning pencil beams).

Mit der Genauigkeit der Behandlung steigt auch die Komplexität der Bestrahlungstechniken und der Behandlungsgeräte an. Aus diesem Grund benötigt man umfangreiche Qualitätssicherungsmaßnahmen, um Fehlbestrahlungen und Behandlungsunfälle zu vermeiden und die korrekte Dosisapplizierung dosimetrisch und geometrisch für den Patienten sicherzustellen. Außerdem können die QS-Daten zum Vergleich unterschiedlicher Strahlentherapieeinrichtungen verwendet werden.

Es wurde bereits eine Reihe von Geräten entwickelt, um den Anforderungen einer schnellen und zuverlässigen Qualitätssicherung in der Strahlentherapie gerecht werden zu können. Die Herausforderungen an die QA durch neue Therapiemethoden erfordern jedoch eine ständige Weiterentwicklung dieser Geräte. Ziel dieser Arbeit ist, die Eignung einer neuen Technologie für die Qualitätssicherung komplexer Strahlentherapie-Techniken zu prüfen.

Die untersuchte Technologie basiert auf Ionisatioskammern, welche in einem Raster angeordnet eine zweidimensionale Oberfläche bedecken. Ionisationskammern wurden aufgrund ihrer intrinsischen Eigenschaften wie Energieunabhängigkeit, Beständigkeit gegen Strahlung und der Möglichkeit der Messung von Wasser-Äquivalentdosis gewählt. Die

hauptsächlich benötigten Eigenschaften der Technologie, neben denen der typischen Standard-Dosimeter, sind eine hohe zeitliche Auflösung und eine geringe Abhängigkeit der Empfindlichkeit von der Pulsdosis. Diese Eigenschaften sind entscheidend, um Dosisverteilungen, welche mit einer hohen Dynamik, hoher Pulsdosis und steilen Gradienten appliziert wurden, detailgetreu und korrekt darzustellen.

Der Charakterisierungsprozess ist in drei Hauptphasen unterteilt. In jeder Phase wird ein Prototyp gebaut und mit verschiedenen Strahlenarten getestet. Der erste Prototyp wird hauptsächlich mit ^{60}Co-Strahlung getestet, um sein Verhalten und Design in einem schrittweisen Prozeß zu optimieren. In den Aufbau des zweiten Prototyps fließen die mit dem ersten Testmuster gewonnenen Erkenntnisse ein und er erhält neue Elektronik sowie ein Design, welches unabhängige und verlässliche Tests ermöglicht. Der Detektor wird intensiv mit klinischen hochenergetischen Photonenstrahlen unterschiedlichster Qualität und mit verschiedenen Dosisleistungen getestet, außerdem mit klinischen Protonenstrahlen, ebenfalls unterschiedlicher Energie und Ströme. Anhand der Ergebnisse lässt sich der Detektor auch mit anderen Detektoren vergleichen. Darüber hinaus wurde die Eignung des Detektors hinsichtlich seines Einsatzes in der Maschinen-Qualitätssicherung (Messung von Output-Faktoren, Strahlprofilen, Tiefendosis-Kurven) und der Verifikation von Bestrahlungsplänen im klinischen Umfeld bewertet. Aufgrund vielversprechender Ergebnisse in dieser Entwicklungsphase wurde ein dritter Prototyp entworfen und gebaut und dieser Detektor an klinischen Bestrahlungsanlagen erprobt.

Die mittels ausführlicher Tests untersuchte Technologie erwies sich für ihre Anwendung in der Strahlendosimetrie als überaus geeignet. Die Hauptergebnisse sind: Eine höhere räumliche Auflösung als gängige Detektoren der gleichen Sensortechnologie, und eine geringe Dosispuls-Abhängigkeit. Es konnte gezeigt werden, dass Eignung zur Messung von Dosisverteilungen mit steilen Dosisgradienten sowie hohen Dosisleistungen besteht. Obwohl ausgezeichnete Ergebnisse erzielt wurden, konnten einige Verbesserungsvorschläge erarbeitet werden. Im Ergebnis dieser Arbeit sind weitere Forschungsarbeiten angezeigt.

Contents

Chapter 1 INTRODUCTION 25
1.1 RADIATION THERAPY 27
1.1.1 Rationale and concept 27
1.1.2 Radiotherapy with photons and protons 30
1.2 QUALITY ASSURANCE 37
1.2.1 The need of QA procedures 37
1.2.2 QA requirements in radiotherapy 38
1.3 THESIS STRUCTURE 44
Chapter 2 DOSIMETRY IN EXTERNAL RADIATION FIELDS 47
2.1 FUNDAMENTALS OF DOSE MEASUREMENTS 49
2.1.1 The Bragg-Gray cavity theory 52
2.1.2 Properties of dosimeters 54
2.1.3 Additional requirements for 2D measurements 60
2.2 TECHNOLOGICAL SOLUTIONS 61
2.2.1 Ionization chambers 61
2.2.2 Diodes 70
2.2.3 Radiochromic films 71
2.2.4 Gel dosimeters 72
2.3 IMPLEMENTATION IN QUALITY ASSURANCE PROCEDURES 73
Chapter 3 DEVELOPMENT OF A NEW IONIZATION CHAMBER TECHNOLOGY 77
3.1 DETECTOR ARRAY V1 78
3.1.1 General description 78
3.1.2 Dosimetric characterization 79
3.1.3 Discussion 86
3.2 DETECTOR ARRAY V2 89
3.2.1 General description 89
3.2.2 Dosimetric characterization 90
3.2.3 Discussion 98

Chapter 4 DETECTOR ARRAY V2 CLINICAL CHARACTERIZATION WITH MV X-RAYS 101
4.1 MACHINE QUALITY ASSURANCE 102
4.1.1 Tissue to phantom ratio 102
4.1.2 Output factors 105
4.1.3 Beam profiling 108
4.1.4 Discussion 113
4.2 PATIENT QUALITY ASSURANCE 115
4.2.1 Patient plan verification through comparison of linear dose distributions 115
4.2.2 Discussion 122
Chapter 5 DETECTOR ARRAY V2 CLINICAL CHARACTERIZATION WITH PROTONS 125
5.1 DOSIMETRIC CHARACTERIZATION WITH PBS PROTON BEAMS 127
5.1.1 Charge collection efficiency 127
5.1.2 Linearity with MU 129
5.2 MACHINE QUALITY ASSURANCE 132
5.2.1 Measurement of uniform dose distributions 133
5.2.2 Measurement of pristine Bragg peak 135
5.3 PATIENT QUALITY ASSURANCE 140
5.3.1 Patient verification through comparison of linear dose distributions 141
5.4 DISCUSSION 147
Chapter 6 DESIGN AND IMPLEMENTATION OF A 2D DETECTOR 149
6.1 GENERAL DESCRIPTION 150
6.2 PRELIMINARY CHARACTERIZATION WITH MV X-RAYS 153
6.3 PRELIMINARY CHARACTERIZATION WITH PROTON BEAMS 155
6.3.1 Linearity with MU 156
6.3.2 Measurements of uniform dose distribution 158
6.3.3 Patient verification through comparison of linear dose distributions 159
6.4 DISCUSSION 164
Chapter 7 CONCLUSIONS AND OUTLOOK 169
Bibliography 179
List of Publications 191
Acknowledgements 193

List of Figures

Figure 1.1. Dose-effect curves and tumor control probability. 29
Figure 1.2. Depth-dose curves for MV photons and protons. 31
Figure 1.3. Sketch of a clinical LINAC. 33
Figure 1.4. Illusration of a clinical proton therapy facility. 33
Figure 1.5. Graphical illustration of the principle of IMRT. 35
Figure 1.6. The concept of gamma index for dose distribution evaluation. 41
Figure 2.1. Kerma and absorbed dose as a function of depth. 51
Figure 2.2. Typical readout electronics for ionization chamber dosimeters. 63
Figure 2.3. Drawings of cylindrical and parallel plate ionization chambers. 64
Figure 2.4. Relation between collected charge and applied potential for an ionization chamber. 66
Figure 2.5. The electric field in plane-parallel and cylindrical geometry of an ionization chamber 67
Figure 2.6. Pulse structure of a beam from a linear accelerator. 67
Figure 2.7. The charge collection process in a plane-parallel ionization chamber. 70
Figure 3.1. D*etector array v1* layout. 79
Figure 3.2. *Detector array v1* setup for irradiation with ^{60}Co beam. 81
Figure 3.3. Dynamic behavior of integrated ionization current in *detector array v1*. 83
Figure 3.4. Detail of a single pixel's dynamic response in *detector array v1*. 83
Figure 3.5. Detail of a single pixel's dynamic response compared to FC65-G. 84
Figure 3.6. Dependence of single chamber response on the applied potential in *detector array v1*. 85
Figure 3.7. Preliminary comparison of 1D dose distributions: *detector array v1* becnhmarked to a:Si flat panel. 85
Figure 3.8. Improvements in the dynamic response to radiation of *detector array v1*. 87
Figure 3.9. Saturation curve of *detector array v1* under continuous gamma radiation. 87
Figure 3.10. *Detector array v2* setup in its dedicated phantom. 90
Figure 3.11. *Detector array v2* setup for angular dependence evaluation. 92
Figure 3.12. Dynamic response of a single chamber in *detector array v2*. 93

Figure 3.13. Sensitivity dependence with time of *detector array v2*. 94
Figure 3.14. Repeatability of *detector array v2* under continuous gamma radiation. 94
Figure 3.15. Profile of ^{60}Co beam acquired with *detector array v2*. 95
Figure 3.16. Integrated charge in *detector array v2* as a function of integral dose. 95
Figure 3.17. Theoretical collection efficiency for *detector array v2*. 96
Figure 3.18. Measured saturation curve for *detector array v2* under MV X-rays. 97
Figure 3.19. Sensitivity dependence of the *detector array v2* on MV X-rays dose per pulse 98
Figure 3.20. Directional dependence of *detector array v2* response with MV X-rays. 99
Figure 4.1. Geometry for measurement of PDD curves. 104
Figure 4.2. TPR curves measured with *detector array v2* for 6 MV and 15 MV X-rays. 105
Figure 4.3. Geometry for measurement of machine OF. 106
Figure 4.4. Agility LINAC's output factors for 6 MV and 15 MV beam quality, measured with the *detector array v2*. 108
Figure 4.5. Beam profiles for 6 MV 10 MVFFF beam quality, measured with the *detector array v2*. 111
Figure 4.6. 1x1 cm^2 field (Varian TrueBeam, 10 MV beam quality) measured with the *detector array v2*. 112
Figure 4.7. CT images of the *detector array v2* inserted into a small phantom. 116
Figure 4.8. Setup of the *detector array v2* inserted into a small phantom for patient plan verification. 116
Figure 4.9. Setup for patient QA measurement with EBT3 film. 117
Figure 4.10. Dose distributions for IMRT and VMAT plans measured with the *detector array v2*, compared to Eclipse TPS. 119
Figure 4.11. VMAT plan (lung tumor) measurement with the *detector array v2*. 120
Figure 4.12. SRS plan (head tumor) measurement with the *detector array v2*. 121
Figure 5.1. Setup of the *detector array v2* inserted into its dedicated phantom for measurements with clinical proton beams. 128
Figure 5.2. Measured efficiency curve of the *detector array v2* with proton beams. 128
Figure 5.3. *Detector array* v2 linearity with dose for 100 MeV proton beam. 130
Figure 5.4. *Detector array v2* linearity with dose for 165 MeV proton beam. 131
Figure 5.5. *Detector array v2* linearity with dose for 226 MeV proton beam. 131
Figure 5.6. Example of proton PBS spots map. 134
Figure 5.7. Dose distributions of 226 MeV proton maps measured with the *detector array v2*. 134
Figure 5.8. Setup for measurement of pristine Bragg peak curves with *detector array v2*. 136
Figure 5.9. Pristine Bragg peak curves (100 and 145 MeV) measured with the *detector array v2*. 138
Figure 5.10. Analytical model applied to measured Bragg peak curves. 138

Figure 5.11. Graphical illustration of the concept of PBS IMPT. 140
Figure 5.12. Setup of MatriXX PT detector for patien plan verification. 141
Figure 5.13. Setup of the *detector array v2* for IMPT patient plan verification. 142
Figure 5.14. PTV and isodose curves from XiO TPS for IMPT prostate treatment. 143
Figure 5.15. Sketch of MatriXX PT pixels' grid and symmetry axes. 144
Figure 5.16. Dose distributions for IMPT plan (distal range) measured with the *detector array* v2, compared to XiO TPS. 146
Figure 5.17. Dose distributions for IMPT plan (medium and proximal range) measured with *detector array v2*, compared to XiO TPS. 145
Figure 6.1. Layout of a base module in *detector array v3*. 151
Figure 6.2. Readout scheme in *detector array v3*. 151
Figure 6.3. *Detector array v3* inserted into its dedicated phantom. 152
Figure 6.4. Setup of *detector array v3* setup for measurements under 6 MV photon beams. 153
Figure 6.5. 5x5 cm^2 and 10x10 cm^2 field (6 MV) measured with the *detector array v3*. 154
Figure 6.6. 6 MV beam profiles measured with the *detector array v3*, compared to MatriXX. 154
Figure 6.7. Setup of the *detector array v3* for measurements with clinical proton beams. 155
Figure 6.8. *Detector array v3* linearity with dose for 100 MeV proton beam. 156
Figure 6.9. *Detector array v3* linearity with dose for 165 MeV proton beam. 157
Figure 6.10. *Detector array v3* linearity with dose for 226 MeV proton beam. 157
Figure 6.11. Raw measurements of 226 MeV PBS proton maps with the *detector array v3*. 158
Figure 6.12. Dose distributions of 226 MeV PBS proton maps measured with the *detector array v3*, compared to Lynx. 159
Figure 6.13. PTV and isodose curves from XiO TPS for IMPT plan 1. 161
Figure 6.14. PTV and isodose curves from XiO TPS for IMPT plan 2. 161
Figure 6.15. Plan 1 dose distributions measured with *detector array v3,* compared to TPS (2D gamma anlysis). 162
Figure 6.16. Plan 2 dose distributions measured with the *detector array v3*, compared to TPS (2D gamma anlysis). 163
Figure 6.17. Repeatability of the *detector array v3* from subsequent measurements of proton PBS maps. 165
Figure 6.18. Crossline and inline profiles of a proton PBS map measured with the *detector array v3*. 165
Figure 6.19. Noise density spectrum of *detector array v3* signal for different shielding configurations. 166
Figure 6.20. 12x12 cm^2 cobalt beam measured with the *detector array v3* and its repeatability. 167

List of Tables

Table 1.1. Machine QA controls for conventional LINACs from AAPM TG 142 report. 43

Table 4.1. Output factors measured with the *detector array v2,* compared to a compact chamber and a stereotactic diode. 107

Table 4.2. Field width and penumbra for 6 MV and 15 MV beam qualities, measured with the *detector array v2* and compared to MatriXX and a:Si flat panel.....110

Table 4.3. Flatness and symmetry of MV X-rays profiles measured with the *detector array v2*, compared to MatriXX and a:Si flat panel. 112

Table 4.4. Comparison between *detector array v2,* MapCHECK 2 and EBT3 in measurements of VMAT and SRS plans. 122

Table 5.1. Proximal range, distal range and peak width extracted from the interpolation of data measured with the *detector array v2*. 139

Table 5.2. Parameters of the analytical model implemented into a MatLab routine and applied to Bragg peak curves measured with the *detector array v2* 139

Table 6.1. Characteristics of two IMPT plans for preliminary patient QA measurements with the *detector array v3*. 160

List of abbreviations

3DCRT	3 Dimensional Conformal Radiation Therapy
AAPM	American Association of Physicists in Medicine
ARDENT	Advanced Radiation Dosimetry European Network Training initiative
CCD	Charge-Coupled Device
COIN	Clinical Oncology Information Network
CPE	Charge Particle Equilibrium
CT	Computed Tomography
DNA	DeoxyriboNucleic Acid
EMI	Electro-Magnetic Interferences
EPID	Electronic Portal Imaging Device
ESTRO	European Society for Therapeutic Radiation Oncology
FFF	Flattening Filter Free
FWHM	Full Width at Half Maximum
IAEA	International Agency for Atomic Energy
IC	Ionization Chamber
ICRU	International Commission on Radiation Units and Measurements
IEC	International Electrotechnical Commission
IMPT	Intensity Modulated Proton Therapy
IMRT	Intensity Modulated Radiation Therapy
IORT	Intra Operative Radiation Therapy
IPEM	Institute of Physics and Engineering in Medicine
KERMA	Kinetic Energy Released per unit MAss
LET	Linear Energy Transfer
LINAC	LINear ACcelerator
MC	Monte Carlo
MLC	Multi Leaf Collimator
MMND-ITRO	Mini-Micro & Nano-Dosimetry and Innovative Technologies in Radiation Oncology

MU	Monitor Unit
NMR	Nuclear Magnetic Resonance
NTCP	Normal Tissue Complication Probability
OF	Output Factors
PBS	Pencil Beam Scanning
PCB	Printed Circuit Board
PDD	Percentage Depth Dose
PRF	Pulse Repetition Frequency
PTCOG	Particle Therapy Co-Operative Group
QA	Quality Assurance
RBE	Relative Biological Effectiveness
RF	Radio Frequency
SAD	Source to Axis Distance
SBRT	Stereotactic Body Radiation Therapy
SD	Standard Deviation
SDD	Source to Detector Distance
SOBP	Spread-Out of Bragg Peak
SRS	Stereotactic Radio-Surgery
SSD	Source to Surface Distance
SSDL	Secondary Standard Dosimetry Laboratory
TAR	Tissue to Air Ratio
TCP	Tumor Control Probability
TCPE	Transient Charge Particle Equilibrium
TG	Task Group
TPR	Tissue to Phantom Ratio
TPS	Treatment Planning System
TRS	Technical Reports Series
UCSF	University of California San Francisco
VMAT	Volumetric Modulated Arc Therapy
WHO	World Health Organization

Chapter 1 INTRODUCTION

Cancer is currently a leading cause of death worldwide, with an estimated 14.1 million new cancer cases occurring in 2012 and 8.2 million deaths [1]. In the western world, cancer has surpassed cardiovascular disease as the most common cause of death for all but the very elderly (i.e. people younger than 85 years) [2]. By 2030, it is projected that there will be approximately 26 million new cancer cases and about 17 million cancer deaths per year [3].

More than 60% of the world's total cases occur in Africa, Asia, and Central and South America. Furthermore, these regions account for about 70% of the world's cancer deaths, a situation that is made worse by a lack of early detection and access to treatment [4]. Indeed, many cancers can be successfully treated, as proved by the increasing percentage of people who survive the disease. In the US, the 5-year relative survival rate (adjusted for normal life expectation) for all cancers diagnosed between 2001 and 2007 is 67%, up from 49% in 1975–1977 [5]. This improvement in survival reflects both progress in diagnosing certain cancers at an earlier stage and improvements in treatment techniques.

Typically, cancer can be treated by surgery, chemotherapy, radiation therapy or a combination of these. The choice of therapy depends upon the location and grade of tumor cells, as well as the cancer stage and the general state of the patient. Besides curative intent, other practical goals of therapy can be the suppression of the cancer to a subclinical state and the maintenance of that state for years of good quality of life (that is, treating the cancer as a chronic disease), and palliative care without curative intent for advanced-stage metastatic cancers.

Cancer treatments often combine surgery, chemotherapy and radiotherapy to enhance the probability of curing or controlling the tumor (e.g. in breast cancer treatment). Sometimes, radiation therapy is the only treatment a patient needs. For instance, prostate and larynx cancers are often treated with radiotherapy alone. It is estimated that nearly two-thirds of the

cancer patients in the US receive radiation therapy during their illness [6]. Among them, almost 90% receive external beam treatments from a linear accelerator.

This thesis focuses on the development and characterization of a novel technology that can be used to build tools for quality controls in external beam radiotherapy. Radiotherapy treatments have become increasingly effective over the past decade and have simultaneously gained a high level of complexity. As a consequence, new and advanced tools are required in the quality assurance workflow, which is meant to ensure a correct and safe fulfilment of the clinical prescriptions during the treatment. A reliable and accurate quality assurance is ultimately designed to improve patient care and to make better use of clinical resources.

1.1 RADIATION THERAPY

Radiation therapy is a collective term for medical treatments where the patient is exposed to ionizing radiation, the primary application of which is in the treatment of malignant disease. The main delivery techniques are external beam therapy, where the patient is irradiated by external fields, and brachytherapy, where radioactive seeds are placed within or in the immediate vicinity of the tumor. Among other external beam therapy techniques, Intra-Operative Radiation Therapy (IORT) delivers a concentrated dose to a tumor bed with external fields during surgery. The purpose of a radiation therapy treatment is generally to deliver a precise radiation dose to a confined target volume that encompasses the malignancy. The absorbed dose in surrounding tissues should simultaneously be minimized in order to avoid damage to healthy organs.

Cancers where curative treatments are common include tumors in the pelvis, head and neck, lung, and central nervous system. Palliative radiation therapy can be administered for clinical cases such as painful bone metastases and tumors that cause pressure on the spinal cord. Radiation therapy is also commonly used as a complementary treatment for patients that undergo chemotherapy or surgery. This is done both in pre-operative conditions to shrink the tumor (facilitating subsequent surgical resection) and in post-operative conditions to decrease the risk of local or regional tumor recurrence.

Advantages of radiation therapy include the facts that the treatment is non-invasive and potentially organ preserving, as well as that systemic side effects are generally avoided. Short-term adverse effects include skin burn, fatigue, and sometimes nausea. Possible later side effects depend on the irradiated body site and can include memory loss, infertility, loss of saliva production, skin problems, and secondary cancers.

1.1.1 Rationale and concept

Exposure of biological tissues to ionizing radiation immediately leads to ionization and excitation of their constituent atoms. The molecules where these atoms reside tend to fall apart, resulting in the so-called free radicals. As water is the most prevalent molecule within

the cell, most of the free radicals are produced by the radiolysis of water. Free radicals are highly unstable: they react with other nearby molecules, transferring chemical damage to them. All components of the cell will be damaged in this way, including proteins, enzymes, membrane components, and so on. However, the most vulnerable part of a cell is the DNA, which can be damaged by reacting with radicals or by direct ionization events.

Cells have evolved to withstand a certain degree of damage, due to the presence of radiation in the natural environment. Thus, most of the radiation-induced DNA lesions can be reversed by cellular repair mechanisms. For instance, a radiation dose of 1 Gy (i.e. 1 J of energy absorbed in 1 kg of matter) produces roughly $2 \cdot 10^5$ ionizations in every cell nucleus, leading to around 1000 single-strand breaks in DNA and possibly 40 double-strand breaks. However, repair processes are so efficient that, in spite of all this damage, most cells survive.

Despite this, the repair mechanisms fail with a small probability, which leads to permanent lesions that make the cell unable to undergo cell division. The repair mechanisms of cells in quickly proliferating tissues such as tumors generally have an increased likelihood of failure. Therefore, it is advantageous to partition the radiation treatment into multiple fractions. These treatment fractions are typically delivered at daily intervals, which is a time-scale that permits the cells in normal tissue to recover from the effects of the irradiation. Fractionated delivery also increases the probability that, at some point during the treatment, each tumor cell is exposed to radiation when it is in a radiosensitive state. The fraction dose and the number of fractions are determined by the estimated number of tumor cells and their radiosensitivity. A typical fractionation schedule for 10^9 tumor cells (i.e. the number of cells commonly assumed to be contained in a tumor reaching the size of 1 cm^3) with an expected cell kill of 50% per 2 Gy fraction is 2 Gy x 30 fractions, which ensures that the expected number of surviving tumor cells is less than one after the last fraction. It is important to note that extinction of all tumor cells at the end of the treatment is often not necessary for long-term survival without recurrence of the cancer; it may instead be sufficient to eradicate the metastatic spread or bring the tumor into partial remission [7].

The tumor control probability (TCP) varies with dose according to a sigmoid relationship (Figure 1.1). This depends on several factors, including the previously mentioned cell repair

processes, the reoxygenation of tumor cells, and their radiosensitivity. For any particular type of cancer, the characteristics of this curve are crucial to the success of therapy. Prescription of dose to be delivered to the tumor volume is calculated according to this relationship, while also considering the normal tissue complication probability (NTCP), which is related to the amount of dose delivered to healthy tissue during the treatment.

An extensive overview of radiobiology is contained in [8] and [9].

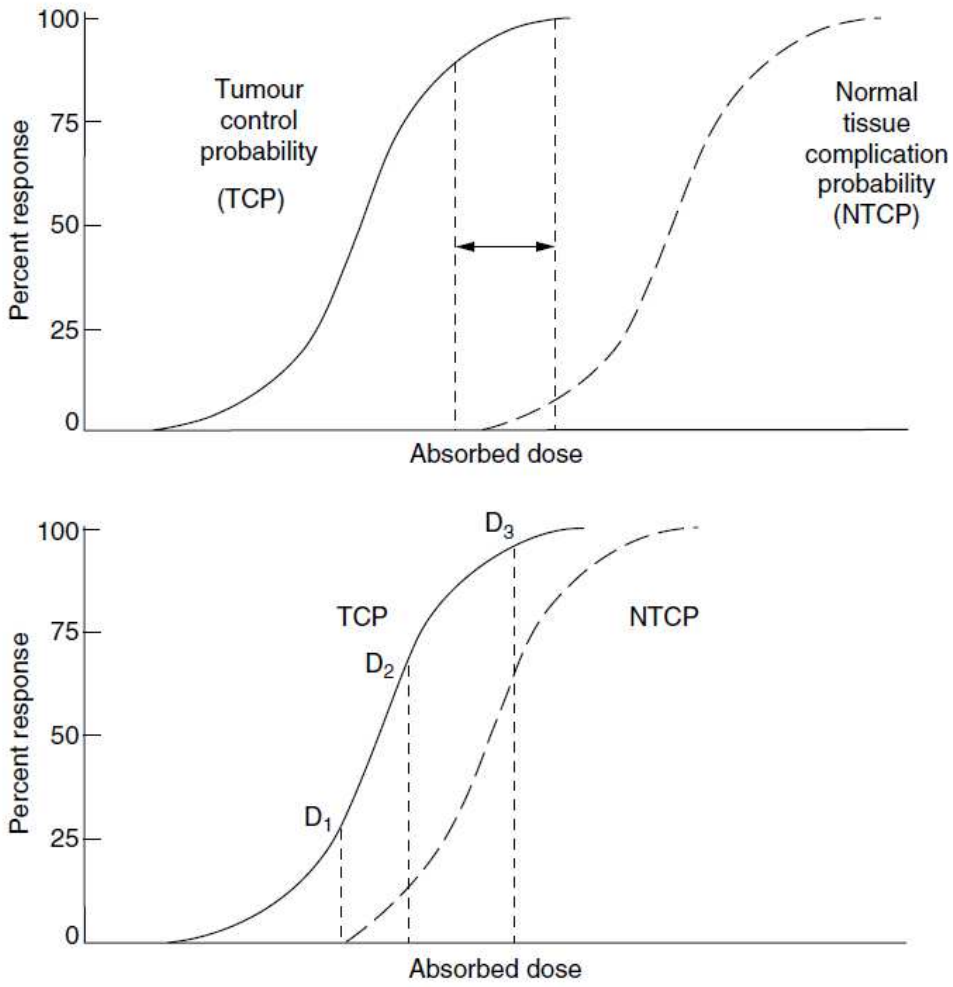

Figure 1.1. Illustration of dose-effect curves for tumor control and normal tissue complications, taken from [9]. The curves are sigmoid and are assumed here to have the same shape and steepness, for simplicity. The upper figure shows a favorable situation for radiotherapy where a dose selected within the range shown by a double arrow is satisfactory. The lower figure shows a less favorable one where none of the 3 dose levels indicated by D1, D2, or D3 can achieve both a high TCP and low NTCP.

1.1.2 Radiotherapy with photons and protons

In a radiotherapy treatment, the prescribed dose can be delivered to the tumor mass by using different types of radiation. For instance, radiotherapy is performed with electrons, kilovoltage (kV) and Megavoltage (MV) X-rays beams, protons, and heavy ion beams. Nevertheless, it is a matter of fact that MV photon beams and proton beams are currently the most widely used radiations in radiotherapy. This is because of their properties and because of a large usage experience gained during the past decades.

1.1.2.1 Physical properties

MV X-rays are typically preferred to electrons or kV X-rays because of their greater penetration. Additionally, a major advantage is the effect of skin sparing brought about by dose build-up, which is greater the higher the energy of the beam. Consequently, the photon depth-dose curve shows a slow exponential decay that follows the maximum reached at the end of the build-up region. These characteristics make external beam photon therapy best suited for treatment of internal tumors. In order to sufficiently differentiate between the absorbed dose in the target volume and the absorbed dose in the surrounding healthy tissue, several overlapping fields can be irradiated from several directions.

Due to their nature as charged particles, protons undergo totally different interactions than photons while travelling through matter. Therefore, the energy deposition is different as well. The depth-dose curve for protons shows a relatively long entrance dose that is followed by a distinct maximum, which is called the Bragg peak. The distal position of the Bragg peak is a function of both the proton energy and the density of the traversed medium. After the Bragg peak, the absorbed dose rapidly falls to zero. A uniform proton dose can be delivered to a spatially extended volume through the superimposition of multiple Bragg peaks associated with different energies.

Thanks to their properties, proton beams are typically used in treatments where the tumor volume is surrounded by radiosensitive organs. The low entrance dose and the lack of exit dose imply that a small number of fields is often sufficient for a proton treatment.

Figure 1.2 shows a qualitative comparison of depth-dose curves for both MV photon beams and proton beams at different energies.

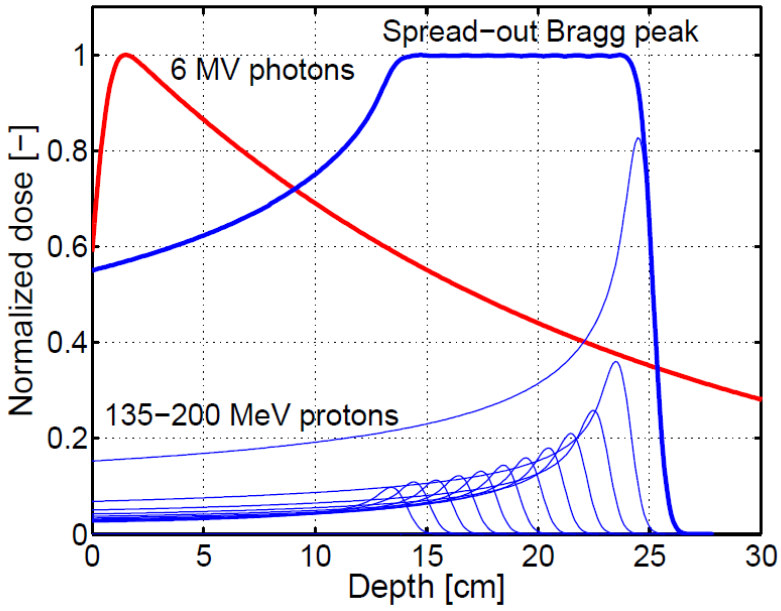

Figure 1.2. Depth-dose curves along the beam axis for 6MV photons and protons in the range 135–200 MeV (in water). The superposition of modulated Bragg peaks produces a spread-out Bragg peak (SOBP) with uniform dose coverage in a large region.

1.1.2.2 Treatment facilities

The most common medical device for MV X-rays external beam radiotherapy is a linear accelerator (LINAC) that accelerates electrons to kinetic energies from 4 to 25 MeV using microwave radio frequency (RF) fields. Secondary photons are emitted as the electrons impinge on a target, before typically being transmitted through a flattening filter, which produces a therapeutic field with uniform intensity. In modern accelerators, the flattening filter can be removed to achieve higher rates of dose delivered per time unit. The beam features a pulsed time structure (5 μs pulse duration) due to the nature of the acceleration system (pulse repetition frequency can be in the range of 100–400 Hz, depending on the beam energy and the manufacturer). Furthermore, each radiation pulse is composed of many "micro pulses", with a typical duration of 30 ps and a typical period of 330 ps.

The field shape is determined by a multi-leaf collimator (MLC). This device is mounted perpendicular to the radiation field and is composed of pairwise opposing leaves that can independently move in and out of the treatment field in order to block a fraction of the irradiation.

The accelerator gantry can be rotated around the patient in order to adjust the field incidence angle. The angle of the treatment couch can also be adjusted to allow for non-coplanar fields. The accelerator contains a set of ionization chambers (typically two – a primary chamber and an emergency backup) that quantifies the radiation output in monitor units (MUs), which are calibrated to a standardized radiation dose in water. More information on LINAC for external beam radiotherapy can be found in [10].

The sketch of a typical isocentric LINAC is represented in Figure 1.3.

In proton therapy, a narrow beam of accelerated protons is generated in a particle accelerator such as a cyclotron or a synchrocyclotron. In the former case, the beam at the exit of the accelerator can be considered continuous in practical applications and QA measurements. The synchrocyclotron beam features a pulsed time structure (usually, the pulse frequency is ~1000 Hz). Other systems used to accelerate protons are based on synchrotrons, which are typically employed to generate clinical beams of heavy ions such helium or carbon.

The proton beam is extracted from the accelerator and guided to the treatment room through a beam line with several focusing and bending magnets. Modern proton therapy systems feature a rotational gantry, which allows for irradiation from any direction (360°) around the patient. The therapeutic field is obtained by either passive scattering, where the field is broadened through a scattering component, or active scanning, where steering magnets are used to scan the particle beam over the target volume.

The energy of the incident protons can be adjusted by transmission through a range shifter of variable thickness. In order to be able to treat all common tumors in the human body, typical beam energies used in proton therapy are in the range 70–230 MeV. An exhaustive review of the state of the art of proton therapy can be found in [11].

Figure 1.4 shows a sketch of a typical proton therapy system.

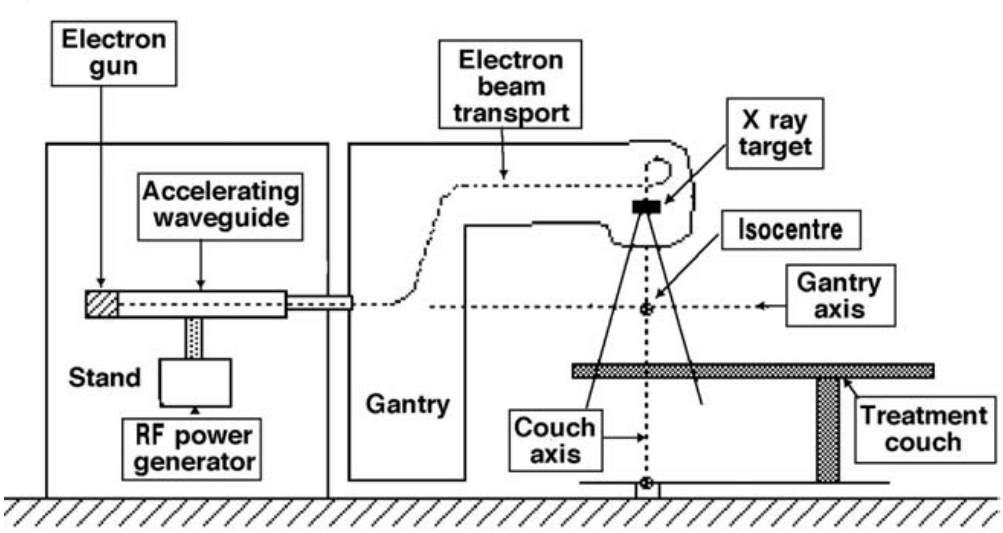

Figure 1.3. Representation of a typical isocentric LINAC design, taken from [10]. The accelerating waveguide and RF power generator are located in the gantry stand; electrons are brought to the movable target through a beam transport system. The machine can produce megavoltage X-rays as well as electrons.

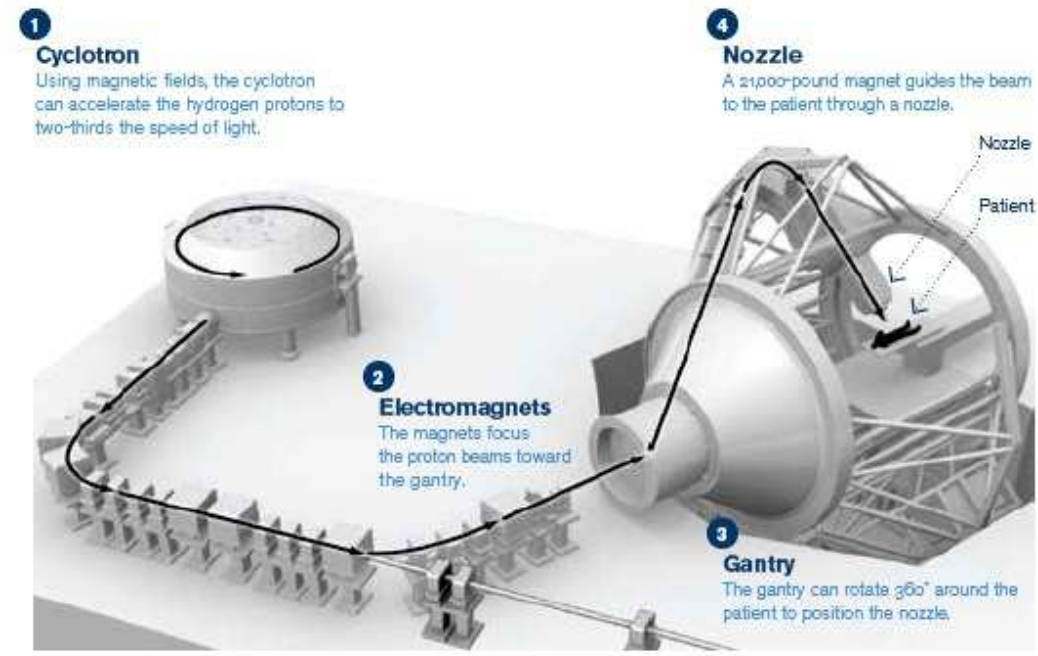

Figure 1.4. Representation of a proton therapy delivery system with 360° gantry (3). A proton beam is generated in the cyclotron (1) and then transported to the treatment room through the beam line (2). The beam is guided to the patient through a nozzle (4), a structure which holds instruments for beam monitoring and beam delivery.

1.1.2.3 Advanced treatment techniques

Considering both MV X-rays and protons, external beam treatments constitute more than 90% of all radiation therapy treatments. The treatments with intensity-modulated fields are the most sophisticated of the external beam treatments, and their use is becoming increasingly common. For instance, the fraction of external beam treatments for prostate cancer that in the US were delivered with intensity-modulated fields increased from 0.15% to 95.9% between 2000 and 2008 [12].

Modulating the intensity of the incoming beams of radiation introduces a degree of freedom which can be applied to achieve a higher conformity of the dose distribution to the tumor target volume [13]. In static intensity-modulated radiation therapy (IMRT), modulated beam profiles are generated at given gantry angles by movements of the multi leaf collimator. The accelerator gantry only rotates when the beam is switched off in order to reach the next delivery angle. An illustration of the IMRT principle is shown in Figure 1.5.

There are two main static IMRT delivery modes. In step-and-shoot or segmented MLC (SMLC), each beam is composed of segments that are delivered consecutively. Each segment is defined by a static MLC configuration and a fraction of the total MU, which is called the segment weight. The beam is switched off as the MLC leaves are repositioned before delivery of the next segment. Step-and-shoot IMRT is an extension of three-dimensional conformal radiation therapy (3DCRT): an older delivery technique that uses similar hardware but only a single static aperture per beam.

The second IMRT method, called sliding window or dynamic MLC (DMLC), uses the continuous movement of leaves during irradiation. During radiation delivery, the leaves move back and forth over the beam planes in unidirectional sweeps. The leaves can either move in a synchronized fashion to minimize interleaf transmission or in a non-synchronized fashion to minimize beam-on time. An extensive review of intensity-modulated radiation therapy can be found in [14].

Volumetric modulated arc therapy (VMAT) [15] is an IMRT mode where the gantry rotates continuously during irradiation. Another distinctive feature of VMAT is that the dose rate

(the number of MUs delivered per unit of time) and the gantry speed can vary during irradiation in order to allow for modulation in MU as a function of gantry angle.

A VMAT treatment can often be delivered within a single gantry rotation by using strategies such as:

- slowing down the gantry rotation and increasing the dose rate over gantry angle intervals, where a high degree of intensity modulation is needed;
- increasing the gantry speed and decreasing the dose rate over angle intervals, where sensitive structures block the field's line of sight.

VMAT does not necessarily provide a better plan than other techniques. However, it is usually delivered in a much shorter time, meaning that the patient generally moves less during the treatment.

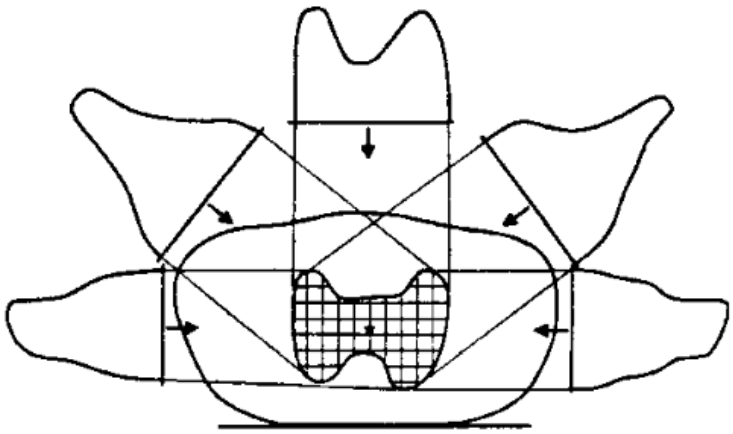

Figure 1.5. Illustration of the IMRT principle, taken from [14]. A number of intensity-modulated beams (5 in this case) with their intensity profiles are shown. The schematic shows an axial cut through the patient's body where the hatched area symbolizes the target volume. The intensities are typically reduced in those regions where the radiation passes through critical structures and increased where the radiation 'sees' primarily the target volume.

In addition, IMRT and VMAT can be used to treat patients in a fashion similar to that of stereotactic radiosurgery (SRS) [16]. Stereotactic radiosurgery is a highly accurate form of radiation therapy that was initially developed to treat small brain tumors and functional abnormalities of the brain. In SRS, the delivered dose distribution is accurate to within one to two millimeters. Despite its name, SRS is a non-surgical procedure that delivers precisely-

targeted radiation at much higher doses than traditional radiation therapy in only a single or a few treatments. In its most typical form, SRS can be delivered with three different items of equipment and sources of radiation:

- ^{60}Co-focused beams in the Gamma Knife, which is ideal for treating small to medium size intracranial lesions;
- MV X-rays from LINAC machines, suitable for treating larger tumors in a single session or during multiple sessions;
- Proton beams for proton radiosurgery.

Despite the high treatment precision, SRS with focused gamma radiation involves long treatment times (e.g. up to 60 min). Treatment time in SRS with high-energy X-rays can be reduced by, for instance, removing the flattening filter from the beam path in the LINAC head, thereby increasing the dose rate during the radiation delivery. SRS can also be applied to the treatment of body tumors through a procedure known as stereotactic body radiotherapy (SBRT).

Intensity-modulated proton therapy (IMPT) refers to actively scanned proton therapy where a plan is composed of several non-uniform fields that together produce an overall uniform target dose [17]. This delivery technique differs from single field uniform dose, where each beam delivers a uniform dose to the target.

An actively scanned proton beam is represented by a number of spots. Each spot is defined by a point in the beam coordinate system and a given particle energy. The fraction of the beam's MU that is associated with a given spot is called the spot weight. A therapeutic field with modulated intensity is then achieved by varying the spot weights in pencil beam scanning (PBS) modality. With PBS proton beams, the tumor volume is covered by delivering spot after spot and layer after layer at different depths. The beam is directed by means of steering magnets positioned in the treatment nozzle.

1.2 QUALITY ASSURANCE

Quality assurance (QA) is an essential part of the radiotherapy process. Calibration errors can lead, for instance, to injury in patients as consequence of wrong treatment. In recent years, it has become accepted that QA is not limited to the calibration of treatment machines, and that it includes every part of the clinical process. The ISO9000 standard has been used as the basis for such a QA system in a number of countries. In this section, an overview is given of general principles underlying the quality assurance in external beam radiation therapy.

According to [10], *quality assurance in radiotherapy is all procedures that ensure consistency of the medical prescription, and safe fulfillment of that prescription, as regards the dose to the target volume, together with minimal dose to normal tissue, minimal exposure of personnel and adequate patient monitoring aimed at determining the end result of the treatment*.

There is a set of accepted criteria, or quality standards, against which the quality of the activity in question can be assessed. Various national and international organizations have issued recommendations for standard in radiotherapy, including the World Health Organization (WHO) in 1988, the American Association of Physicists in Medicine (AAPM) in 1994, the European Society for Therapeutic Radiation Oncology (ESTRO) in 1995, and the Clinical Oncology Information Network (COIN) in 1999. Other organizations, such as the International Electrotechnical Commission (IEC) in 1989 and the Institute of Physics and Engineering in Medicine (IPEM) in 1999, have issued recommendations for certain parts of the radiotherapy process. Where recommended standards are not available (as in the case of machine QA in proton therapy with pencil beam scanning delivery mode), local standards need to be developed, based on a local assessment of requirements.

1.2.1 The need of QA procedures

Quality assurance procedures in radiotherapy are designed for different purposes and can be characterized as follows:

- Quality assurance reduces uncertainties and errors in dosimetry, treatment planning, equipment performance, treatment delivery, and so on, thereby improving dosimetric and geometric accuracy and the precision of dose delivery. This improves radiotherapy results (treatment outcomes), thus improving tumor control rates and reducing rates of complication and recurrence.
- Quality assurance does not only reduce the likelihood of accidents and errors, but also increases the probability that they will be recognized and rectified sooner if they occur, thereby reducing their consequences for patient treatment. This is the case not only for larger incidents but also for the most likely minor incidents.
- Quality assurance allows for a reliable intercomparison of results among different radiotherapy centers, ensuring more uniform and accurate dosimetry and treatment delivery. This is necessary for both clinical trials and for sharing clinical radiotherapy experience and transferring it between centers.

Improved technology and more complex treatments in modern radiotherapy can only be fully exploited if a high level of accuracy and consistency is achieved.

1.2.2 QA requirements in radiotherapy

With the increased complexity of radiation treatments, more frequent and detailed quality checks are required. Although the main concern is the maintenance of accurate output, it is clear that, if the overall accuracy of treatment needs to be within the tolerances expected by radiation oncologists, other parameters require regular checking. Typical tolerances are (as recommended by the International Commission on Radiation Units and Measurements, ICRU, [18]):

- Accuracy of delivered dose to the specification point ±3% (1 standard deviation (SD));
- Accuracy of delivered dose at all other points in the target volume ±5% (1 SD);
- Accuracy of positioning beam edges and shielding blocks in relation to the planning target volume ±4 mm (1 SD).

Taking into consideration the many steps involved in delivering a dose to a target volume in a patient, each step must be performed with an accuracy that is better than those specified to achieve these recommendations.

The QA program for machines which deliver the radiation exists to assure that their characteristics do not deviate significantly from their baseline values acquired at the time of acceptance and commissioning. Many of these baseline values are entered into treatment planning systems (TPS) to characterize and/or model the treatment machine. They can, therefore, directly affect treatment plans calculated for every patient treated on that machine. Deviation from the baseline values could thus result in suboptimal treatment of patients. Machine parameters can deviate from their baseline values as a result of many reasons. There can be unexpected changes in machine performance due to machine malfunction, mechanical breakdown, physical accidents, or component failure.

A number of quality assurance protocols have been written (see introductory part of this section), and these often differ in the test frequencies that they recommend. General guidelines have to be adapted to specific needs anyway. For example, if a machine is being regularly used for stereotactic single fraction high dose treatments, the quality checks relating to the mechanical alignment and stability with arc rotation will need to be carried out frequently, perhaps even before each treatment. On the other hand, for treatments being given over a six-week period, a dose inaccuracy of 3% for two or three fractions can be easily compensated for in subsequent fractions. Thus, less frequent checks may be appropriate.

Table 1.1 shows examples of recommended QA procedures taken from AAPM Task Group (TG) 142 [19], a comprehensive guideline for quality assurance of medical accelerators in MV X-rays external beam radiotherapy. AAPM Task Group 224 is expected to publish the equivalent report for proton machines in 2017 (a preliminary overview can be found in [20]). Since the publication of the ICRU report 78 [21], there has been no dedicated report dealing with proton therapy quality assurance. Nowadays, the majority of these procedures in clinical activity are either adopted from or modified versions of procedures outlined in the AAPM TG 40 report [22, 23].

The last important step before allowing the patient to be treated is to check the whole chain and perform a quality assurance control of the plan being delivered. Especially for intensity-modulated and stereotactic radiation therapy, individual patient QA is of great importance in detecting possible errors that can result in erroneous treatments. For instance, when calculating an IMRT or SBRT/SRS dose distribution, a number of factors, such as small field dosimetry and MLC leaf modelling, become much more important than they are in standard therapy. Many parameters involved in the treatment are difficult to measure, resulting in potential sources of errors which cannot be controlled with simple machine QA. Therefore, pre-treatment patient QA is needed alongside machine QA to ensure correct treatment delivery.

It is standard practice to check individual plans with a pre-treatment comparison between the measurements and the treatment planning system computation. The most accurate and widespread solution is to measure the dose with a detector inserted in a phantom with a simple geometry. Patient-specific QA based on this practice is generally considered to be the most reliable, and it is mandatory in many countries (e.g. US), although it requires extensive resources. In many countries, a tendency exists to only perform patient-specific QA for the most complex treatment plans and to verify the ‘standard’ ones with independent calculations (e.g. by using specific class solutions for each tumor site). The Netherlands Commission on Radiation Dosimetry provides a good example of this in the Code of Practice for QA and Control for Intensity-Modulated Radiotherapy [24].

Similar procedures have been adopted for plan verification of IMPT irradiations. The accuracy required in the delivery of scanned pencil beams makes the verification of each individual plan essential. The measurements to be compared with planning system computation are typically performed with a detector being placed in a water tank and the beam being shot with a fixed angle of incidence. This configuration allows comparison of planar dose distribution at different depths.

There are two aspects which are equally important in the verification of a patient plan: the absolute dose and the dose distribution. To perform a reliable analysis of plan dose distributions, the concept of gamma index has been proposed by Low et al. [25]. Here, the

tolerance is expressed as a combination of the maximum distance to a point of agreement (Δd_M) and the maximum percentage dose difference (ΔD_M). The measure of acceptability is the multidimensional distance between the measurement and calculation points in both the dose and the physical distance, scaled as a fraction of the acceptance criteria (ΔD_M, Δd_M). In a space composed of dose and spatial coordinates (Figure 1.6), the acceptance criteria form an ellipsoid surface, the major axis scales of which are determined by individual acceptance criteria and the center of which is located at the measurement point in question. When the calculated dose distribution surface passes through the ellipsoid, the calculation passes the acceptance test for the measurement point.

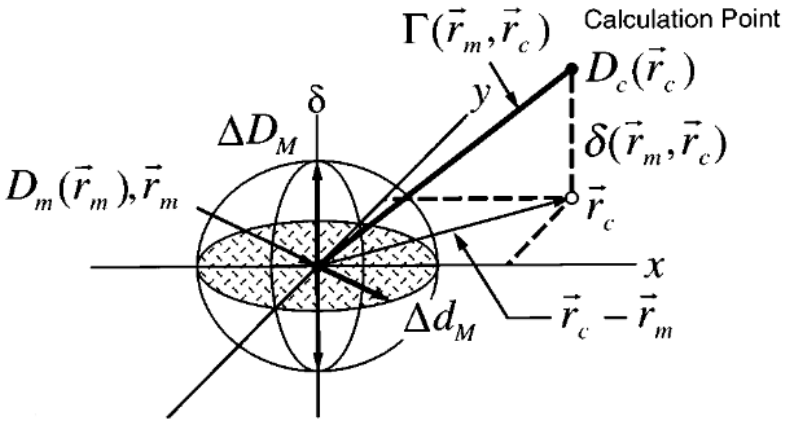

Figure 1.6. Geometrical representation of the dose distribution evaluation based on the gamma index. The ellipsoid surface that represents the acceptance criteria is defined by the equation: $\mathbf{1} = \sqrt{\frac{r^2(r_m,r)}{\Delta d_M^2} + \frac{\delta^2(r_m,r)}{\Delta D_M^2}}$, where $\boldsymbol{r(r_m, r)} = |\boldsymbol{r - r_m}|$ and $\boldsymbol{\delta(r_m, r)} = \boldsymbol{D(r) - D_m(r_m)}$.

The minimum radial distance in the dose-distance space between the measurement point and the calculation points is defined as quality gamma (γ) index:

$$\gamma(r_m) = min\{\Gamma(r_m, r_c)\}\ \forall\{r_c\} \tag{1.1}$$

where

$$\Gamma(r_m, r_c) = \sqrt{\frac{\boldsymbol{r^2(r_m, r_c)}}{\boldsymbol{\Delta d_M^2}} + \frac{\boldsymbol{\delta^2(r_m, r_c)}}{\boldsymbol{\Delta D_M^2}}} \tag{1.2}$$

$$\boldsymbol{r}(\boldsymbol{r_m}, \boldsymbol{r_c}) = |\boldsymbol{r_c} - \boldsymbol{r_m}| \tag{1.3}$$

and

$$\boldsymbol{\delta}(\boldsymbol{r_m}, \boldsymbol{r_c}) = \boldsymbol{D_c}(\boldsymbol{r_c}) - \boldsymbol{D_m}(\boldsymbol{r_m}) \tag{1.4}$$

is the difference between dose values on the calculated and measured distributions, respectively. Regions where $\gamma > 1$ correspond to locations where the calculation does not meet the acceptance criteria. The gamma index, as described by Low et al. [25], quantifies the point-by-point difference between measured and calculated bi-dimensional dose distributions. Recently, a 3D gamma metric [26] has been introduced in the field of radiation physics as an extension of the 2D gamma index into another dimension, allowing for consideration and evaluation of the entire volumetric patient dose distribution. A comparison of the results of 2D and 3D gamma analysis for clinical treatment plans can be found in literature [27].

Applications with which to compare the dose grid calculated by the planning system with measurements from detectors are available. A number of technologies have been developed to accomplish this task; an overview of them can be found in Chapter 2 of this thesis. The goal of this work is to characterize a new technology aimed to perform quality assurance tests in modern external beam radiotherapy.

Table 1.1. Examples of machine QA procedures for conventional LINACs from AAPM TG 142 report.

		Machine-type tolerance		
Procedure	Frequency	Non-IMRT	IMRT	SRS/SBRT
Dosimetry				
X-Ray and electron output constancy	daily		3%	
X-Ray and electron output constancy	monthly		2%	
Dose rate output constancy	monthly	n.a.	2%	2%
Photon beam profile constancy	monthly		1%	
Electron beam profile constancy	monthly		1%	
Electron beam energy constancy	monthly		2%/2mm	
X-Ray flatness	annual		1% change from baseline	
Electron flatness	annual		1% change from baseline	
X-Ray symmetry	annual		±1 % change from baseline	
Electron symmetry	annual		±1 % change from baseline	
X-Ray/electron output calibration	annual		±1 % (absolute)	
Output factors for X-Ray	annual		2% for field size < 4 x 4 cm^2, 1% ≥ 4 x 4 cm^2	
X-Ray beam quality (PDD_{10} or TMR_{10}^{20})	annual		±1 % change from baseline	
Mechanical				
Light/radiation field coincidence	monthly		2 mm or 1% on a side	
Gantry rotation isocenter	annual		±1 mm from baseline	
Coincidence of radiation and mechanical isocenter	annual	±2 mm from baseline	±1 mm from baseline	±1 mm from baseline

1.3 THESIS STRUCTURE

From the discussion developed throughout Section 1.1 and Section 1.2, it should be clear to the reader that quality assurance plays a major role in radiation oncology, since it ensures the clinical fulfillment of a treatment prescribed to a patient with cancer. Due to its importance, quality assurance is generally regulated by means of protocols and practices defined by national and international organizations.

As new and advanced treatment techniques, such as stereotactic radiosurgery with megavoltage photons or intensity-modulated therapy with protons, are added to the possibilities of external beam treatments, devices dedicated to QA controls must also be adapted. Therefore, the succeeding parts outline the characterization and development process of an innovative detector technology that meets the quality assurance requirements described in the introduction.

Chapter 2 (“Dosimetry in External Radiation Fields”) summarizes the principles of dosimetry in external radiation beams, starting with the definition of absorbed dose in a medium and the explanation of the Bragg-Gray cavity theory which establishes the theoretical basis of experimental dose determination and, therefore, of dosimeters’ construction. An overview of properties required for dosimeters is provided. The discussion of possible technological means to build dosimeters focuses on ionization chambers, diodes, gels, and films. The way in which these technologies can be deployed to build area detectors needed in radiation oncology QA procedures is discussed at the end of the chapter, together with some examples of commercially available solutions.

Chapter 3 (“Development of a New Ionization Chamber Technology”) presents the principles and the characteristics of the new detector technology with respect to the requirements and the needs expressed in this introduction and in Chapter 2. The development process of a first prototype (*detector array v1*) based on this technology is described as well, beginning with an investigation of single pixel dynamic response to radiation, and the first attempt of measurement of linear dose distributions. A subsequent section presents the second prototype concept (*detector array v2*), which is based on the outcomes of the *detector array v1*

characterization. The goal of *detector array v2*, which is still a linear detector, is to fix the construction rules learned from the *detector array v1* experience and to provide a reliable and reproducible device. A comprehensive characterization with gamma radiation and megavoltage photons has been performed to prove the suitability of the detector to performing measurements in a clinical environment.

A summary of these measurements is presented in Chapter 4 ("*Detector array v2* clinical characterization with MV X-rays"), which deals with the experimental characterization of the prototype at the Klinikum rechts der Isar (Munich, DE) and at the University of California San Francisco (UCSF) hospital (San Francisco, US, CA). The capability of the detector to address both machine QA and pre-treatment patient QA was investigated and results benchmarked to references commonly used in clinical practice.

Chapter 5 ("*Detector array v2* clinical characterization with protons") has the same structure as Chapter 4, but deals with characterization of the prototype in clinical pencil beam scanning proton beams. The experimental campaign has been performed at the Proton Therapy Center Czech s.r.o. (Prague, Czech Republic). Again, the performances of the detector for both machine QA and pre-treatment patient QA are compared to standard references.

Chapter 6 ("Design and Implementation of a 2D Detector") presents the proof of concept of a *detector array v3* which features an innovative concept with regards to assembly and readout electronics, as well as a 2D-sensitive region. Preliminary results from measurements of IMPT plans are described.

Finally, the last part (Chapter 7 – "Conclusions and Outlook") summarizes and concludes this thesis, providing an overview of the achievements and of the open questions.

Chapter 2 DOSIMETRY IN EXTERNAL RADIATION FIELDS

Radiation dosimetry deals with methods for a quantitative determination of the energy deposited by ionizing radiation in a given medium (i.e. the absorbed dose). This quantitative determination is typically carried out with devices, called dosimeters, which provide a direct measurement of the amount of dose absorbed in a defined sensitive volume. One refers to absolute dosimetry as a technique that yields information directly about absorbed dose in Gy at one reference point in a phantom, with well-defined conditions and geometry, following established protocols. Relative dosimetry relates the dose under non-reference conditions to the dose under reference conditions. Thus, no conversion factors or conversion coefficients are generally required. Field size factors, percentage depth dose curve, and beam profiles are typical examples of relative dosimetry measurements.

Together with the concept of absorbed dose, other quantities which are radiologically relevant (such as kerma and fluence) and that can be directly measured or calculated are introduced in Section 2.1. Subsequently, an overview on the Bragg-Gray cavity theory is provided. This theoretical analysis establishes the relationship between the dose absorbed in a probe to the dose absorbed in a given medium. Therefore, it represents the basis for experimental dose measurement. Properties of dosimeters are outlined at the end of the section.

Section 2.2 deals with technological solutions used nowadays to implement dosimeters for quality assurance in radiotherapy. The discussion focuses mainly on ionization chambers (representing the chosen technology for the device being investigated in this work), diodes, radiochromic films, and gels.

Section 2.3 is a summary of the implementation of the above-mentioned technologies in current radiotherapy quality assurance procedures.

2.1 FUNDAMENTALS OF DOSE MEASUREMENTS

The absorbed dose is by definition a non-stochastic quantity which can be related to both indirectly and directly ionizing radiation, as well as to any ionizing radiation source distributed in the absorbing medium. For indirectly ionizing radiation such as photons or neutrons, the energy is imparted to the medium in two separate processes. In the first step, the energy is transferred as kinetic energy to secondary charged particles, these mainly being electrons. In the second step, these charged particles give some of their kinetic energy to the medium through processes of ionization and atomic excitation that result in the absorbed dose. Together with the ionization and excitation of atoms in the medium, secondary charged particles may also lose some of their initial energy in the form of radiative losses (i.e. bremsstrahlung or annihilation).

In [28], the absorbed dose is defined in terms of the stochastic energy ε imparted to matter of mass m in a finite volume V

$$\varepsilon = (R_{in})_u - (R_{out})_u + (R_{in})_c - (R_{out})_c + \sum Q \tag{2.1}$$

where $\sum Q$ is the net energy due to variation of the rest mass in V and R is the radiant energy of all the uncharged (u) and charged (c) particles entering (in) or leaving (out) the volume V. At any point P in V, the absorbed dose is thus defined as

$$D = \frac{d\bar{\varepsilon}}{dm} \tag{2.2}$$

where $d\bar{\varepsilon}$ is the expectation value of the energy imparted to an infinitesimal volume dV at point P, and dm is the mass in dv. In a very basic way, one can even define the absorbed dose rate at a point P and time t as

$$\dot{D} = \frac{dD}{dt} = \frac{d}{dt}\left(\frac{d\bar{\varepsilon}}{dm}\right) \tag{2.3}$$

Considering that D is a quantity that can be experimentally measured at high accuracy using different methods, the absorbed dose has become the most important quantity in radiological physics. Although the induced effects are not always purely proportional to D and their dependence on the absorbed dose can be complex due to the interplay of many processes at

different levels, it is true that radiotherapy treatments delivered today by physicians and medical physicists are based on the concept of absorbed dose in the human tissue. When radiotherapy is carried out with a beam of charged particles (e.g. protons), the "efficiency" of the radiation is typically compared to the "efficiency" of an X-rays beam. Therefore, the absorbed dose is expressed in terms of relative biological effectiveness (RBE) weighted dose, to take into account the different nature of the radiation itself.

It should be kept in mind that in the case of photons the absorption of energy in the medium does not take place at the same location as the transfer of energy. This is because of the non-zero range of the secondary electrons raised from photon interactions. The transfer of energy from the photon beam to the charged particles is described by kerma (acronym of kinetic energy released per unit mass), without concern as to what happens after this transfer.

The kerma is usually divided into two components: the collision kerma k_{col} and the radiative kerma k_{rad}. The collision kerma k_{col} is the part of kerma that leads to the production of electrons that dissipate their energy as ionization in or near the electron tracks in the medium, and it is therefore the expectation value of the net energy transferred to charged particles per unit mass at the point of interest excluding the radiative energy loss. The radiative kerma k_{rad} is the part of the kerma that leads to the production of radiative photons as the secondary charged particles slow down and interact in the medium. Since radiative photons mostly escape from the volume of interest, one usually relates the absorbed dose to collision kerma. In general, the ratio of dose and collision kerma is defined as

$$\beta = D/k_{col} \tag{2.4}$$

If radiative photons escape the volume of interest, an assumption is made that $\beta \approx 1$.

The relation between kerma and absorbed dose under the condition of charge particle equilibrium (CPE) and under the condition of transient charge particle equilibrium (TCPE) is illustrated in Figure 2.1. As the high-energy photon beam penetrates the medium, collision kerma is maximal at the surface of the irradiated material because photon fluence is greatest at surface. The charge particle fluence, and thus the dose, increases as a function of depth until the depth of dose maximum z_{max}. When the condition of CPE is satisfied, the dose absorbed by the medium is related to the electron fluence φ_{med} in the medium. If the electron spectrum was monoenergetic,

$$D_{med} = \varphi_{med} \cdot \left(\frac{S_{col}}{\rho}\right)_{med} \tag{2.5}$$

where $(S_{col}/\rho)_{med}$ is the mass collision stopping power of the medium at the energy of the electrons (i.e. the rate of energy loss per unit path length divided by the density of the medium, as stated in the Bethe theory).

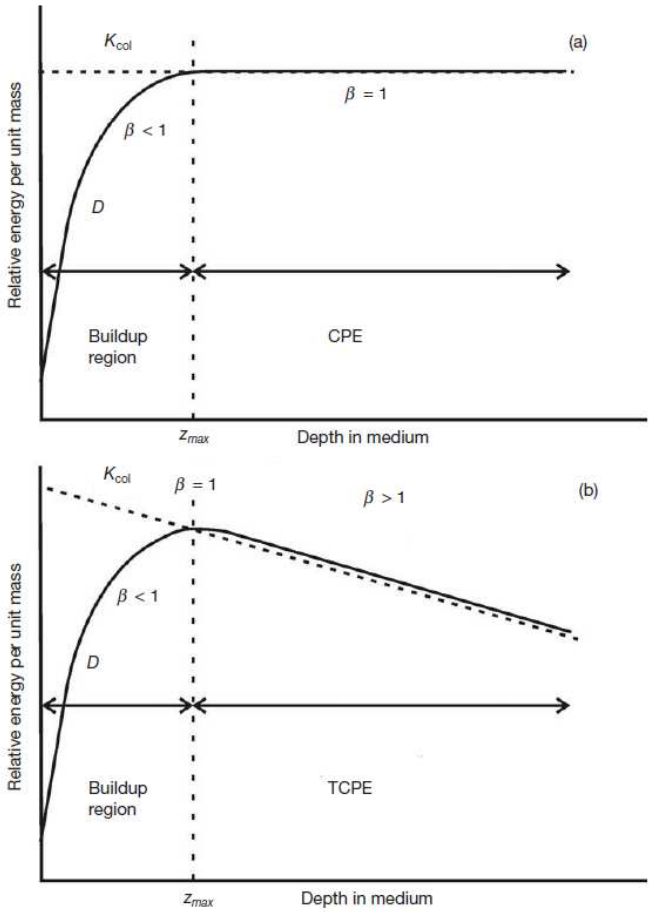

Figure 2.1. Kerma and absorbed dose as a function of depth in a medium irradiated by a high-energy photon beam for (a) hypothetical case of no photon attenuation or scattering and (b) the realistic case. β is defined as the ratio between D and K_{col} (image taken from [10]).

In a more realistic case, electron fluence is better described by a continuous spectrum. Therefore Eq. (2.5) can be further expressed as

$$D_{med} = \int_0^{E_{max}} \varphi_{med,E}(E) \cdot \left(\frac{S}{\rho}\right)_{med} (E)dE = \varphi_{med} \cdot \left(\frac{\bar{S}}{\rho}\right)_{med} \tag{2.6}$$

where $(\bar{S}/\rho)_{med}$ is the mass collision stopping power of the medium averaged on the fluence energy spectrum. Eq. (2.6) is the basis for the cavity theory, which provides the fundamental principles for dose measurement in a given medium.

In case of heavy-charged particle beams (e.g. proton beams), Eq. (2.6) is still valid and applies directly to the fluence of the primary radiation beam [29].

2.1.1 The Bragg-Gray cavity theory

Measuring the absorbed dose in a certain medium is possible by introducing a radiation sensitive device (a probe or dosimeter) into the medium. The Bragg-Gray cavity theory [30, 31, 32] relates the dose absorbed in the probe inserted in a medium to that in the medium itself, which usually differs from the sensitive material of the probe.

If a fluence of identical charged particles passes through an interface between two different media, g and w, then one can write Eq. (2.6) for each side of the boundary

$$D_w = \varphi_w \cdot \left(\frac{\bar{S}}{\rho}\right)_w \tag{2.7}$$

$$D_g = \varphi_g \cdot \left(\frac{\bar{S}}{\rho}\right)_g \tag{2.8}$$

Moreover, assuming that the fluence is continuous and not perturbed across the interface, the absorbed dose in the two adjacent media can be expressed as

$$\frac{D_g}{D_w} = \frac{(\bar{S}/\rho)_g}{(\bar{S}/\rho)_w} \tag{2.9}$$

Eq. (2.9) is still valid in presence of a thin layer of medium g sandwiched between regions containing medium w, under the condition of continuous fluence across the layer g and both the interfaces. In this case, the dose ratio D_g/D_w is again equal to the corresponding ratio of mass collision stopping powers. If one considers the layer (or cavity) filled with the medium g to be the sensitive volume of the dosimeter, it is then possible to estimate the dose measured in the medium w.

There are two conditions that are necessary for the application of the Bragg-Gray cavity theory. Firstly, the thickness of the cavity must be small enough in comparison with the range of the charged particles incident on it that its presence does not perturb the charged particle fluence. The accomplishment of this condition depends on the scattering properties of g and w: the mean path length of the particles in traversing the cavity has to be identical to its value if g were replaced by a layer or cavity filled with w and having the same mass thickness. The result is that the electron fluences in Eq. (2.7) and Eq. (2.8) are the same and equal to the equilibrium fluence established in the surrounding medium under the condition of CPE or TCPE.

For heavy charged particles, this condition related to small fluence perturbation is not particularly challenging, because of the little scattering. However, for electrons, even a very small cavity can generate a non-negligible perturbation unless the two media are close enough in atomic number.

A second condition of the Bragg-Gray relation is that the absorbed dose in the cavity is assumed to be deposited only by the charged particles crossing it. This condition implies that interactions of primary particles (photons) in the cavity are assumed to be negligible, that all the charged particles (electrons) must be produced outside the cavity, and that charged particles (electrons) entering the cavity are assumed not to stop in it.

Under these two conditions, Eq. (2.9) is valid; the dose to the medium w can be made explicit:

$$D_w = D_g \cdot \left(\frac{\bar{S}}{\rho}\right)_{w,g} \tag{2.10}$$

where $(\bar{S}/\rho)_{w,g}$ is the ratio of the average mass collision stopping powers of the medium and the cavity. If the medium g that fills the cavity is a gas in which a charge Q is produced by the radiation, D_g can be expressed in terms of charge as

$$D_g = \frac{Q}{m} \cdot \left(\frac{\bar{W}}{e}\right)_g \tag{2.11}$$

where m is the mass of the gas and $(\bar{W}/e)_g$ is the mean energy spent per unit charge produced in the gas. By substituting Eq. (2.11) into Eq. (2.10), we obtain the Bragg-Gray relation, expressed in terms of cavity ionization:

$$D_w = \frac{Q}{m} \cdot \left(\frac{\bar{W}}{e}\right)_g \cdot \left(\frac{\bar{S}}{\rho}\right)_{w,g} \tag{2.12}$$

Eq. (2.12) allows to calculate the absorbed dose in the medium surrounding the cavity on the basis of the value of charge produced in the cavity gas, once the correct values of m, $(\bar{W}/e)_g$ and $(\bar{S}/\rho)_{w,g}$ are provided.

For the purpose of this work, which is concerned with air-vented ionization chambers, it is useful to note that Q is generally greater than the value of the charge Q' collected from the cavity volume and that m may be smaller than the total mass of the gas contained in the cavity. The reason is that in dosimeters such as ionization chambers, as discussed further in Section 2.2 of this chapter, processes of ionic recombination take place in the dosimeter volume, and a fraction of this volume may be inactive in providing a measurable charge (e.g. in the presence of a guard ring with the same potential of the collection electrode, or due to regions with negligible electric field).

The Bragg-Gray theory, in the form of Eq. (2.12), may also be applied to solid- or liquid-filled cavities. For example, the medium g might be an organic liquid or a thin plastic film that gradually darkens as a known function of the absorbed dose. However, since in clinical applications one is mainly concerned with dose to water, in the case of a sensitive medium with density significantly higher than water, it is more difficult to satisfy the Bragg-Gray conditions because of the high density of the medium itself. Section 2.3 illustrates different technologies which can be used to build a dosimeter.

2.1.2 Properties of dosimeters

In order to be practically usable, radiation dosimeters must exhibit several desirable characteristics, which are explored in this section.

2.1.2.1 Reproducibility and accuracy

The reproducibility of a dosimetric measurement can be estimated from the data obtained in repeated measurements under similar conditions, and it is influenced by random errors due to fluctuations in instrumental characteristics, ambient conditions, stochastic nature of radiation fields and so on. High reproducibility is associated with a small standard deviation of the distribution of the measurement results. Typically, when a measurement of a dosimetric quantity x is repeated N times, the best estimate value for x is $\bar{x}$, i.e. the arithmetic mean value of all measurements x_i:

$$\bar{x} = \frac{1}{N}\sum_{i=1}^{N} x_i \tag{2.13}$$

and the associated standard deviation can be expressed as

$$\sigma_x = \sqrt{\frac{1}{N-1}\cdot\sum_{i=1}^{N}(x_i - \bar{x})^2} \tag{2.14}$$

This formalism has been used in this work when results from experimental measurements are presented.

The accuracy of dosimetry measurements is defined by the proximity of their expectation value to the true value of the measured quantity. While the estimation of this uncertainty from collected data is not possible, high accuracy of dosimetric measurements can be guaranteed through high-quality calibrations of the detector and by ensuring that the detector itself has a significant stability with dose and time. It is worth mentioning that, in experiments that are limited to relative measurements, reproducibility is more important than accuracy.

2.1.2.2 Linearity and dose range

A dosimeter must have an adequate dose sensitivity over the dose range to be measured. The dose range, as defined in the standard IEC 60731 [33], is the range within which the sensitivity is high enough to ensure a good reproducibility and dose linearity. The lowest range limit is typically determined by background fluctuations, noise, instrumental

sensitivity, and, in some cases, the stochastic nature of radiation. The upper limit may be affected by loss of linearity or saturation effects (e.g. the saturation of readout electronics, if a reset system is not implemented).

Ideally, the dose sensitivity throughout the range should be constant, in a way that keeps dosimeter reading M linearly proportional to the dose D. In practice, a dosimeter exhibits some degree of non-linearity, which can be quantified in terms of percentage deviations from a linear fit applied to readings M over the entire dose range. For instance, IEC 60731 recommends evaluating the non-linearity of a dosimeter as follows: the half full reading $M_{0.5}$ is taken as a reference; the input signal $D_{0.5}$ required to produce this reference scale reading is measured. At another reading M, produced by an input signal D, the percentage deviation from linearity is given by

$$100 \cdot ((M \cdot D_{0.5}/M_{0.5} \cdot D) - 1) \tag{2.15}$$

Another way to quantify non-linearity of a dosimeter is to evaluate the deviations of readings from a single end-point linear fit. In this case, drift from linearity at the lower or upper limit of the dose range can be easily identified.

Non-linear systems may be acceptable as well, though they require a calibration curve built on multiple measurements of M.

A dosimetric system is typically composed of a sensor (e.g. an ionization chamber) and a reader (e.g. an electrometer), and in some cases the linearity of the two components should be measured separately. This is important to ensure that the combined effect of two hypothetical non-linear behaviors of both the reader and the sensor does not produce a linear response of the system over the dose range or, in a worst-case scenario, that a non-linearity introduced by the reader affects the linear behavior of the sensor.

2.1.2.3 Dose rate dependence

In a dosimeter dedicated to measurement of a time-integrated dose, it is necessary that its reading does not depend on the rate at which the dose is delivered. In conventional LINACs, the dose rate is the product of the dose delivered within each radiation pulse and the pulse repetition frequency (PRF), and it may change during measurements due to the way radiation

treatment is implemented. For instance, during pre-treatment plan verification, the dose rate of delivered radiation is changed by either changing the PRF, the MLC configuration, or the gantry position with respect to the phantom where the dosimeter is located.

In most cases, lowest dose rate is limited by background fluctuations. An example of low dose rate limitation that is not related to background can be found in radiochromic film dosimeters, where self-repair processes of grains for radiation with low linear energy transfer (LET) at low enough dose rates may lead to underestimation of irradiated dose.

The upper limit of dose rate independence occurs when charged-particle tracks are created closely enough together in space and time to allow the ions, electron-hole pairs, or active chemical products to interact between tracks. An example of this is the general recombination phenomena, which may take place in the sensitive volume of ionization chambers that are either air-vented or filled with liquid materials. As long as the radiation pulse period is much larger than the chamber collection time, the chamber response does not show significant variations. However, if the dose rate is increased, such as by increasing the dose delivered within each single pulse, the charge collection efficiency of the chamber can be limited (an overview of recombination theory in gas-filled ionization chambers is given in Paragraph 2.2.1.1). In this case, correction factors are necessary and must be applied to dosimeter readings.

2.1.2.4 Energy dependence

The sensitivity of a dosimeter is generally dependent on radiation beam quality. Typically, dosimetry systems are calibrated in reference conditions at specified radiation beam quality (or qualities) and used over a much wider energy range. In fact, the energy spectrum changes practically as soon as the measurement conditions are different from those used during calibration, for instance due to a different measurement position or depth or as a consequence of the MLC motion. The energy independence of a dosimeter ensures that the measurements are reliable even out of reference conditions.

Ideally, the energy response should be flat (i.e. the system calibration should be independent of energy over a certain range of radiation qualities). In reality, the energy correction has to be included in the determination of the dose in many measurement situations. In

radiotherapy, as no dosimeter is water or tissue equivalent for all radiation beam qualities, the energy dependence is an important characteristic of a dosimetry system. Typical examples of energy dependence in regularly used dosimeters are as follows: the overresponse of diodes to low-energy radiation due to the onset of photoelectric effect; the overresponse of thermoluminescent dosimeters to high-energy radiation, resulting from the effect of pair production; and the overresponse of ionization chambers due to photoelectric contribution generated in parts made out of copper or steel and adjacent to the sensitive volume.

^{60}Co gamma rays are frequently used as the reference energy in the evaluation of the energy dependence of a detector in photon beams, which can be estimated through the equation

$$\frac{(M/D_{water})_{\bar{E}}}{(M/D_{water})_{Co-60}} = \frac{\left[(\mu_{en}/\rho)_g/(\mu_{en}/\rho)_{water}\right]_{\bar{E}}}{\left[(\mu_{en}/\rho)_g/(\mu_{en}/\rho)_{water}\right]_{Co-60}} \tag{2.16}$$

which takes water as a reference material and where (μ_{en}/ρ) is the mass-energy absorption coefficient. In Eq. (2.16), $\bar{E}$ is the mean energy of the electrons bremsstrahlung spectrum [34]. Because of the large secondary-electrons ranges with Megavoltage beam qualities, this equation is only satisfied to the extent that TCPE is present. In radiotherapy dosimetry, this is typically achieved by performing measurements with the dosimeter inserted into a phantom, thus providing enough material buildup around the sensitive volume.

2.1.2.5 Time stability and stability with dose

The characteristics of a dosimeter should be stable with time before and after being irradiated. Effects of temperature, atmospheric oxygen or humidity, light, delivered radiation, and so on can cause a gradual change in dose sensitivity or in the instrumental background.

Dosimeters are categorized into different classes on the basis of their long-term stability properties. For instance, reference class dosimeters must feature a ±0.5% accuracy in dose measurement over a one year period [33].

The radiation hardness (or stability with dose) defines the impact of the exposure to radiation on the properties of a dosimetric system. Changes of sensitivity versus the dose are typically due to radiation-induced degradation of the material which fills the active volume. Dosimeters' radiation hardness depends on beam quality and becomes crucial when the

system is irradiated with high-energy neutron and ion beams. Not only beam quality but also cumulative exposure time and dose rate have an influence on the radiation-hardness properties of a dosimeter. Silicon-based detectors are a typical example of solid state detectors in which the material filling the active volume undergoes degradation with accumulated dose. In this particular case, the annealing time (i.e. the time spent at room temperature after irradiation) plays a crucial role in the stabilization of the detector sensitivity.

A typical example of a radiation-hard detector technology is represented by air-vented ionization chambers. The air which flows through the chamber constitutes the sensitive medium (cf. Paragraph 2.2.1) and does not undergo any degradation or change in qualities, even after being irradiated for a long time.

The radiation hardness of the readout system is not relevant as long as it is placed outside of the treatment room. Otherwise, the effect of radiation on the reader has to also be assessed.

2.1.2.6 Spatial resolution and physical size

Since the dose is a point-measured quantity, the dosimeters should ideally have a very small active volume. The finite size of a detector leads to volume-average effects which, if measurements are carried out in a non-uniform dose distribution, introduce an additional error in the measurement. As an example, thermoluminescent dosimeters come in very small dimensions and their use, to a great extent, approximates a point measurement. Ionization chamber-type dosimeters are of finite size in order to reach the required sensitivity, although pinpoint micro chambers partially overcome this problem (the smallest pinpoint ionization chambers commercially available show a sensitive volume down to 0.01 cm^3).

The spatial resolution of a dosimeter is a fundamental parameter when measurement of 2D or even 3D dose distribution is required. It is determined by two different parameters: the size of the effective volume (as discussed above) and, in the case of a pixelated detector, the inter-pixel distance. Film dosimeters and gels ensure excellent 2D and 3D spatial resolution, respectively. This topic is addressed in a more detailed discussion in Section 2.1.3.

2.1.2.7 Usability

Dosimetry systems should be as easy to handle as possible, especially those dedicated to radiotherapy applications. Functionality, compactness, robustness, and reusability are all features which add a great value to a detector in terms of possible applications. Furthermore, dosimeters that provide a direct and instantaneous reading are generally regarded as being more convenient than passive dosimeters, as prompt reading allows for the optimization of the clinical workflow and the clinical resources, resulting in maximum benefit for the patient.

2.1.3 Additional requirements for 2D measurements

To fulfill the requirements of quality assurance in radiotherapy, a dosimeter must feature all of the above-listed properties and simultaneously be able to measure multi-dimensional dose distributions. The reason for this has already been discussed in Section 1.2, and it is mainly related to the use of dosimeters for patient plan verification.

There are dosimetric technologies which show an intrinsic capability of measuring 2D or 3D dose distributions (film, gel, and scintillators), as well as others that require the assembly of many point detectors (i.e. ion chambers or diodes) and are arranged in arrays in order to accomplish bi-dimensional measurements. The pattern in which these point detectors are arranged over the sensitive area, as well as their number, might change depending on the final application. In the ideal case, the spatial density of point detectors should be as high as possible in one or two dimensions (depending on the application). This requirement increases the technological complexity of a 2D device: high spatial density means many (typically more than one thousand) output channels which have to be read in parallel, avoiding signal spread between them. For some types of detectors (e.g. silicon flat panels), the signal can be acquired through a multiplexing readout, thus reducing the complexity of the readout electronics from $1/L^2$ to $1/L$ (where L is the sensor pitch). However, the use of multiplexing requires, in addition to the complication of channel selection, the possibility to store the accumulated charge (signal) on a capacitor, thus limiting the use of this technique to monolithic silicon-based sensors.

2.2 TECHNOLOGICAL SOLUTIONS

There are several technologies which are currently employed in detectors for dosimetric measurements in radiation therapy. This section outlines those that are the most commonly used for QA purposes: ionization chambers, diodes, GAFCHROMIC® films, and gel dosimeters. In Section 2.3, the basic features of each technology will be compared on the basis of possible applications.

Other technologies are mentioned here, for instance, plastic scintillators, thermoluminescent systems, and diamond based detectors. To the knowledge of the author, all detectors based on these technologies come in the form of point dosimeters or with limited two-dimensional geometries. The exception is a commercial 2D scintillator-based detector: the Lynx (IBA Dosimetry GmbH, Schwarzenbruck, Germany). This is typically used for commissioning measurements and machine QA with proton and carbon-ions beams [35]. The Lynx detector is made of a Gadolinium-based scintillator screen of 30x30 cm^2, coupled with a CCD camera that allows for the acquisition of images with 0.5 mm spatial resolution in real-time acquisition mode. In Chapter 5, the Lynx has been used to benchmark a few measurements of machine QA performed with the new ionization chamber technology in proton beams.

2.2.1 Ionization chambers

The ionization chamber (IC) is the most widely used type of dosimeter for accurate measurements of dose to water. Such chambers are used both for dose determination in reference conditions (i.e. for beam calibration) and for relative dose measurements.

Ionization chambers come in various shapes and sizes, depending upon the specific final use, but generally they all have some shared features.

An ionization chamber is essentially a gas- or liquid-filled cavity that is surrounded by a conductive outer wall and that has a central collecting electrode. The wall and the collecting electrode are separated with a high-quality insulator to reduce the leakage current when a polarizing voltage is applied to the chamber.

A guard electrode is usually provided in the chamber to further reduce chamber leakage. The guard electrode must have the same potential as the collecting electrode; the guard intercepts the spurious current from insulators and allows it to flow to the ground, bypassing the collecting electrode. It also ensures the field uniformity in the sensitive volume of the chamber, with resulting advantages in charge collection.

Air is typically used as the sensitive gas in an ionization chamber. The initial event of the interaction of indirectly ionizing radiation with the chamber is characterized by a release of high-energy electrons in the chamber wall or phantom through the photoelectric effect, Compton effect, or pair production. Some of these electrons enter the chamber's sensitive volume and ionize air molecules, producing positive ions and low-energy electrons in this volume. The low-energy electrons attach themselves to electronegative oxygen molecules in the air, forming negative ions. Thus, in an air-based ionization chamber, the charged particles collected are the positive and negative ions (ion pairs) rather than positive ions and electrons.

Measurements with air-vented ionization chambers require temperature and pressure correction to account for the change in the mass of air in the chamber volume, which changes with the ambient temperature and pressure. These corrections are easy to be made (e.g. in commercial detectors, environmental parameters are typically detected by the detector itself and corrections are automatically applied to the reading), while the construction of sealed chambers is much more complicated. Thus, air-vented ionization chambers are the preferred choice in clinical dosimetry. Typical examples of sealed ionization chambers are the monitor chambers placed in the LINAC head.

Ionization chambers can be filled with materials other than air, such as polymeric liquids (e.g. isooctane, tetra methyl pentane, cyclo hexane), without changing the operating principles discussed above. The reason behind this choice lies in the fact that, by increasing the density of the sensitive medium, the sensitivity of the detector rises as well. Therefore, it is possible to build a dosimeter which features the same sensitivity of one filled with air but which has a smaller collecting volume. A typical drawback in liquid-filled ionization chambers is the lower ion mobility in the sensitive medium, which can lead to a higher probability of charge recombination with high dose rates.

In a typical dosimetric system, the ionization chamber is coupled with an electrometer, which is a device for measuring the small ionization current generated in the detector in real time. This current is typically in the range 10^{-12}–10^{-9} A, depending on the sensitivity of the chamber and on the dose rate. Electrometers are essentially a high-gain operational amplifier in negative feedback configuration, as shown in Figure 2.2.

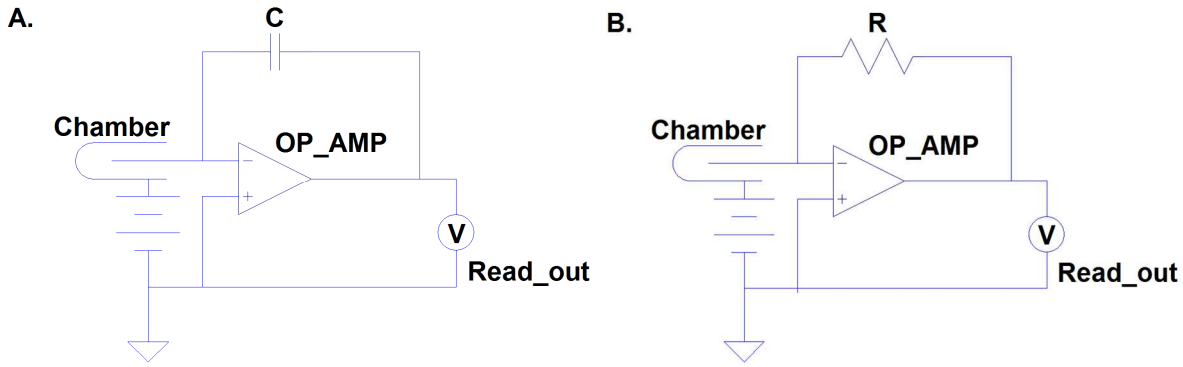

Figure 2.2. Operational amplifiers in negative feedback configuration (picture adapted from [36]). In integrate mode (A) the charge collected by the chamber is integrated in the capacitor C, generating a voltage V across C. In rate mode (B) the ionization current generated in the chamber flows through the resistor R, generating a voltage V across R. The feedback elements determine the sensitivity of the electrometer.

In radiotherapy applications, two chamber geometries are primarily used: cylindrical geometry and parallel plate geometry (Figure 2.3 shows single detectors based on these geometries). Cylindrical chambers are produced by various manufacturers, with active volumes between 0.01 and 1 cm^3. The wall, made out of material with low atomic number Z, has a thimble shape and defines the sensitive volume together with the stem insulator. The central electrode typically has a dimeter of 1 mm or less, and it is made of steel, aluminum, or carbon-based materials.

Parallel-plate ionization chambers consist of two plane walls, one serving as an entry window and polarizing electrode and the other as the back wall and collecting electrode, as well as a guard ring system. The back wall is typically made of conductive plastic or a non-conductive material coated with a conductive layer of graphite. The height of sensitive volume can be reduce to 0.6 mm in commercial detectors.

Further technical details, recommendations, and codes of practice for dosimetry with different ionization chambers, as well as correction factors needed for absolute dose measurements, can be found in several technical reports. Examples are the Technical Reports Series (TRS) from the International Agency for Atomic Energy (IAEA) [37, 38, 39] and the Task Group report from AAPM [40].

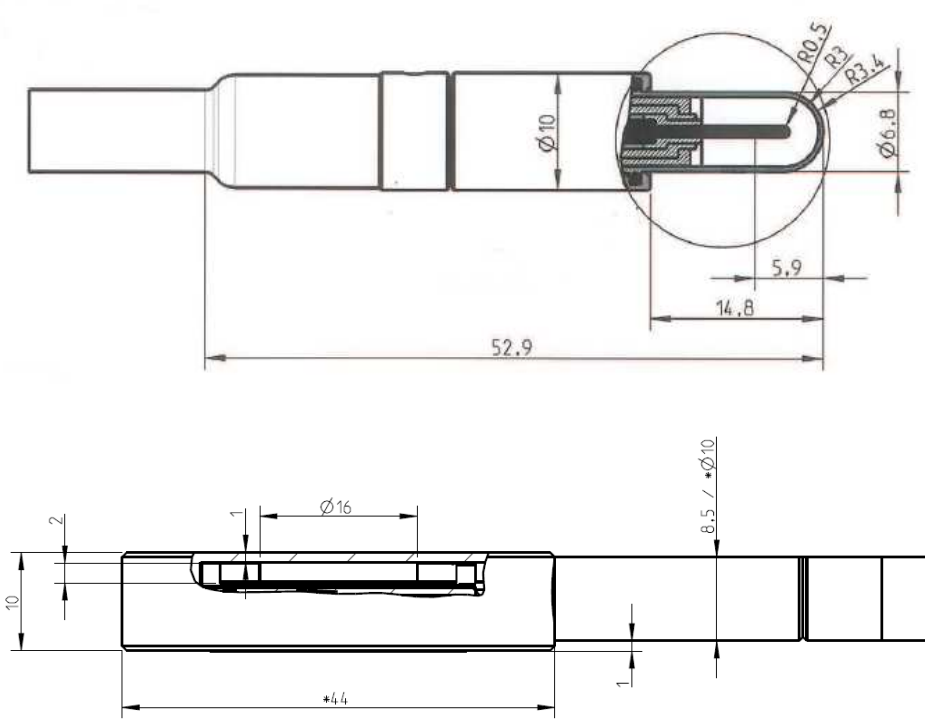

Figure 2.3. Cylindrical ionization chambers (top) are mostly recommended for calibration of MV X-rays beams, whereas parallel plate ionization chambers (bottom) are recommended for calibration of electron beams, proton beams or surface dose measurements.

2.2.1.1 Theory of ionic recombination in ionization chambers

IC-based detectors or, more generally, gas detectors, may suffer from ionic recombination when exposed to elevated dose rates. The amount of ionic recombination inside the sensitive volume is directly related to detector dose rate dependence, as mentioned in Paragraph 2.1.2.3. The theory of recombination in gas detectors addresses the problem of estimating the drop in the efficiency associated with ionic recombination, as shown by Boag [41] and ICRU report 34 [42] and reported on hereafter.

In a gas detector, the charge Q produced in the gas by ionizing phenomena is proportional to the energy deposited in the gas itself (when no amplification of the charge is involved). In any practical case, the charge that is collected by the biased electrode in the chamber and measured by the electrometer is less than Q, because of recombination of some positive and negative ions within the gas. Two types of recombination processes usually take place in the cavity of a gas detector, which are as follows.

- Initial (or columnar) recombination is the recombination of negative and positive ions formed in the same charged particle track. The initial recombination is independent from dose or dose rate, since the number of tracks occurring per unit volume does not influence the recombination within a given track, unless the space-charge density becomes so great that the electric field strength is weakened or the tracks begin to overlap. It is most likely to occur in densely ionized tracks (high LET particles) or in high-pressure gases, but it is negligible for electrons at 1 atm with collecting fields greater than 100 V/cm.
- General (or volume) recombination occurs when ions from different tracks encounter each other on their way to the collecting electrodes. The general recombination depends on how many ions are created per unit volume and per unit time. Therefore, general recombination is dose-rate dependent, since a greater density of ions of both signs moving in opposite directions increases the probability that they will recombine.

A chamber is said to be saturated when such ionic recombination is absent. Increasing the ion-collecting potential applied to the chamber reduces recombination and asymptotically approaches saturation. For instance, in Figure 2.4, the typical variation of the collected charge Q' as a function of the applied potential is shown.

The field strength in the collecting volume depends on the geometry of the chamber. Referring to the geometries represented in Figure 2.3, plane-parallel chambers have uniform field strength $E = P/d$ [V/cm] throughout the whole volume, whereas cylindrical chambers feature field strengths $E(r) = P/(r \cdot ln(a/b))$ [V/cm] depending on the radius (Figure 2.5). The weakening of the electric field in a large part of the volume in cylindrical chambers compared to plane chambers of the same electrode separation requires a higher potential V to produce the same collection efficiency. However, it is not possible to indefinitely increase the

applied potential to eliminate recombination because of the onset of electrical breakdown in insulators or the onset of multiplication phenomena in the gas.

The type of gas also plays a role in the collection efficiency of a chamber. In general, it is much easier to saturate an ion chamber containing a non-electronegative gas because of the lower drift velocity of negative ions compared to free electrons.

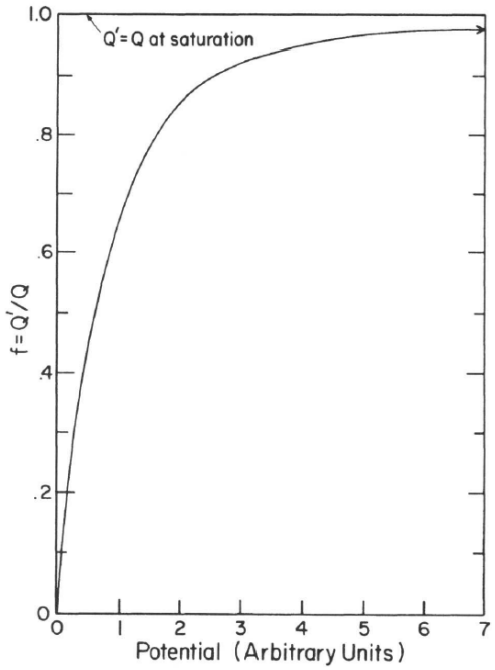

Figure 2.4. Variation of ionization charge Q' collected from an ion chamber on the applied potential (picture taken from [34]). Q is the charge produced by external radiation in the chamber volume.

General recombination may play a significant role when the radiation is delivered in pulsed beams with short pulses and high repetition frequency. For instance, Figure 2.6 shows the typical time structure of a beam delivered by a linear clinical accelerator. In these conditions, the ion concentrations created by the pulse are much higher than those obtained in a chamber exposed to continuous radiation at the same mean dose rate. Consequently, general recombination is greatly enhanced while initial recombination remains unchanged, being an effect localized within each track.

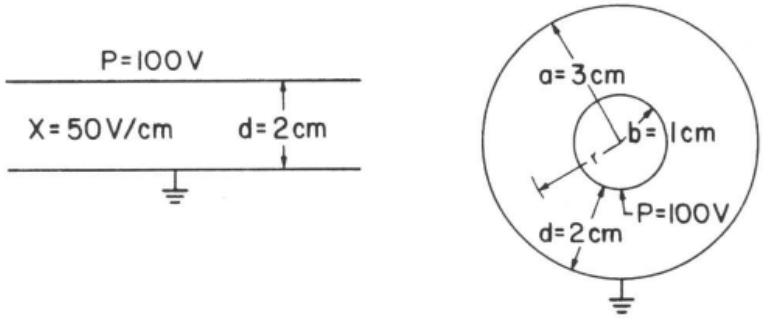

Figure 2.5. From [34], electric field strength in plane-parallel geometry (left) and cylindrical geometry (right). For the cylindrical chamber, a and b are the radii of the outer and inner electrodes, respectively. P is the applied electric potential.

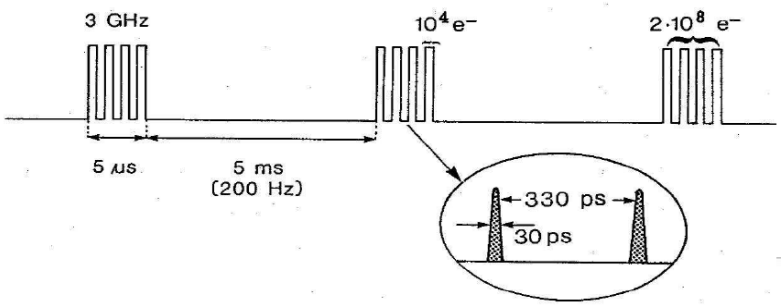

Figure 2.6. Typical pulse structure of a linear accelerator beam. In this example, three "macro pulses" of about 5 μs duration and 5 ms period are shown. Each "macro pulse" is composed of many "micro pulses" with 30 ps duration and 330 ps period. With these values, about 14000 micro pulses fall within a macro pulse. However, to make the drawing clear, only four are sketched.

The requirements which must be satisfied to ensure the validity of the Bragg-Gray classical equation for ionization dosimetry (Eq. (2.12)) are not affected by pulsing radiation. The one factor that becomes more difficult to measure with pulsed radiation is the charge liberated per unit mass of gas in the cavity, $J_g = Q/m$. As a matter of fact, ionic recombination in pulsed radiation may lead to non-linear behavior of the detector. In relative dosimetry, non-linearity in dose rate may lead to distortions of dose profiles and depth dose curves, whereas in absolute dosimetry, this effect may lead to inaccuracies in absorbed dose determination.

In parallel plate ionization chambers exposed to instantaneous and non-overlapping pulses, the effect of general recombination can be calculated under certain assumptions. These are as follows.

- The electrons liberated in the gas immediately attached themselves to molecules to form negative ions. This assumption is a reasonable approximation for many of the ionization chambers commonly used for dosimetry.
- The charge carriers are positive and negative ions with well-defined mobility k_1 and k_2.
- Recombination occurs at the rate $\alpha n_1 n_2$, where n_1 and n_2 are the concentrations of positive and negative ions, respectively, and where α is a constant called *recombination coefficient*.
- Space charge due to the ions does not significantly affect the externally applied collecting field.
- The thermal diffusion of the ions can be neglected in comparison with their drift in the electric field. This assumption can be considered valid at the field strengths normally used in dosimetric ion chambers.

A simple model depicting a parallel plate chamber which has received an instantaneous radiation pulse is shown in Figure 2.7. The space between electrodes consists of three regions:

1. a region of width ε_1, close to the negative plate from which all the negative ions have been driven out;
2. a region of width ε_2, close to the positive electrode and containing only negative ions;
3. a central region containing both negative and positive ions which, being formed in equal concentrations and disappearing only by mutual charge exchange, maintain equal though declining concentrations as long as the overlap persists.

Assuming the initial ion density n_0 to be uniform in the volume of the gas cavity (a condition generally satisfied in small ionization chambers designed for measurements of absorbed dose at a point), the ion density within the overlap region decreases with time t by ionic recombination with the second order equation:

$$n(t) = \frac{n_0}{(1 + \alpha \cdot n_0 \cdot t)} \tag{2.17}$$

Considering the applied electric field, $X = V/d$, with V applied potential and d the distance between the plates, the overlap region is narrowing at the rate $(k_1 + k_2) \cdot X$ and vanishes after a time T_1:

$$T_1(d) = \frac{d}{(k_1 + k_2) \cdot X} \tag{2.18}$$

After this time interval T_1, the positive and negative ion clouds have completely separated. Therefore, no further recombination can occur. It is then possible to calculate the fraction of the ions which recombine during the lifetime of the overlap, T_1, and to deduce the fraction collected (i.e. the collection efficiency), f. The result has been presented by Boag [41]:

$$f(u) = \frac{1}{u} \cdot \ln(1 + u) \tag{2.19}$$

where

$$u(d, V) = \frac{\alpha/e}{(k_1 + k_2)} \cdot \left\{ \frac{(n_0 \cdot e) d^2}{V} \right\} \tag{2.20}$$

or

$$u(d, V) = \mu \cdot \left(\frac{r \cdot d^2}{V} \right) \tag{2.21}$$

with $r = n_0 e$ the initial charge density (of each sign) and μ a constant involving the recombination coefficient and the ions mobility.

The principal design quantity which affects recombination of an ion chamber in pulsed radiation is undoubtedly the time during which the overlap persists. To reduce this to a minimum, one must design a chamber with a short inter-electrode distance d and a relatively uniform field strength.

The recombination model for parallel plate ionization chambers discussed here has been used to calculate the theoretical efficiency under pulsed beams of the first clinical prototype built with the technology under investigation. The outcome of the model compared to experimental data is presented in Section 3.2.2.2.

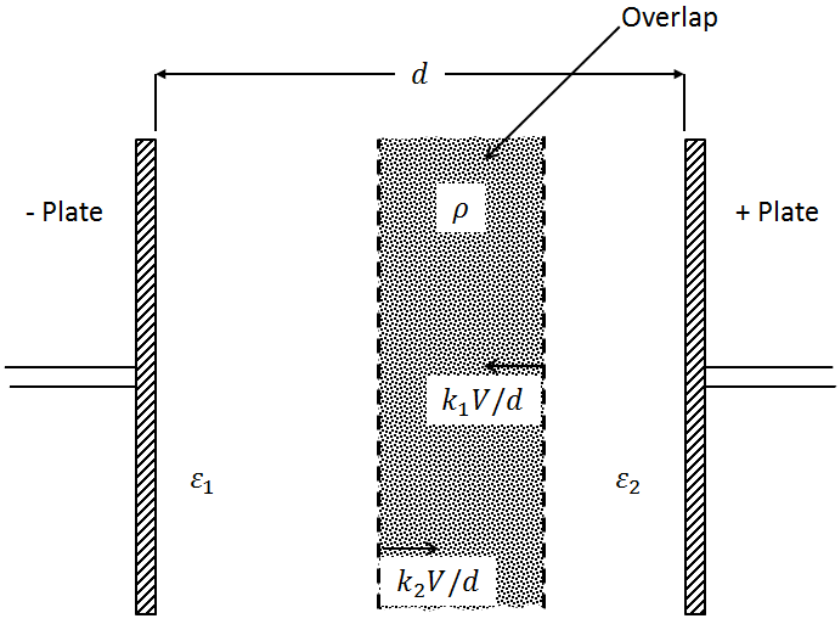

Figure 2.7. Cross-section of a parallel plate ionization chamber during charge collection process.

2.2.2 Diodes

Silicon diode dosimeters are essentially a p-n junction diode, normally referred to as n-Si or p-Si type dosimeters, depending upon the base material. The p-Si type has become largely used for dosimetry in radiotherapy because it is less affected by radiation damage and has a much smaller dark current than the n-Si type.

When radiation is delivered on a p-Si diode dosimeter, electron-hole pairs are produced throughout the body of the detector, including the depletion layer. The charge collection process is very different than in an ionization chamber. While an ionization chamber requires a high voltage supply, the high electric field across the junction makes charge collection possible for the diode without external bias.

The minority carriers (electrons on the p side and holes on the n side) diffuse toward the junction. Those carriers within approximately one diffusion length from the junction edge are able to reach it before they recombine. They are then swept across the junction by the built-in potential and measured by the electrometer. The total current consists of the radiation-

induced photocurrent and the electrical leakage current due to the offset voltage from the electrometer.

The sensitivity per unit volume of diodes is much higher than that of ionization chambers, leading to the possibility to build smaller sensors. Diodes show a variation of dose response with accumulated dose, and hence they are not recommended for the measurement of absolute dose. They are used to measure absolute dose in the case of in-vivo applications, as in this case ionization chambers cannot be applied to the skin of the patient due to high voltage bias. For such application, silicon diodes require frequent recalibrations.

A major drawback of silicon diodes is their energy dependence. This is due to the atomic number being higher than the average atomic number of water, which leads to an excess photoelectric effect. Correction factors to be applied to measured data are summarized in the report from AAPM Task Group 62 [43].

2.2.3 Radiochromic films

Radiochromic film is a self-developing type of film for radiotherapy dosimetry. The most commonly used is GAFCHROMIC® type EBT (Ashland Specialty Ingredients, Bridgewater, NJ, US). It is a colorless film with a nearly tissue-equivalent composition (9.0% hydrogen, 60.6% carbon, 11.2% nitrogen and 19.2% oxygen), and it develops a blue color upon radiation exposure. Radiochromic film contains a special dye that is polymerized upon exposure to radiation. The polymer absorbs light, and the transmission of light through the film can be measured with a general purpose optical scanner.

Radiochromic films ensure a very high resolution that is practically limited by grain size. Therefore, they can be used to obtain highly accurate measurements of two-dimension dose distributions.

Absolute dosimetry with radiochromic films is possible but requires high precision and is time-consuming (typically 12 hours waiting time is needed for the complete development of films). When performing film absolute dosimetry, one has to take care that the conditions during measurements are the same as those during the calibration. Moreover, film properties may change significantly from batch to batch, and a specific calibration for each batch is

therefore recommended. A number of studies of film uniformity and reproducibility are available in literature; some examples can be found in [44, 45].

2.2.4 Gel dosimeters

Gel-dosimetry systems are the only truly 3D dosimeters that are suitable for dose measurements. At the same time, the dosimeter is a phantom that can measure absorbed dose distribution in a full 3D geometry. Gels are nearly tissue equivalent (no energy corrections needed) and can be molded to any desired shape or form.

Gel dosimeters can be divided into two types: Fricke gels and polymer gels. In Fricke gels, Fe2+ ions in ferrous sulphate solutions are dispersed throughout a gelatin matrix. Radiation-induced changes are either due to direct absorption of radiation or due to intermediate water free radicals. Upon radiation exposure, ferrous ions Fe2+ are converted into ferric ions Fe3+ with a corresponding change in paramagnetic properties that may be measured using nuclear magnetic resonance (NMR) relaxation rates or optical techniques. A 3D image of the dose distribution is created. A major limitation of Fricke gel systems is the continual post-irradiation diffusion of ions, resulting in a blurred dose distribution.

In polymer gel, monomers such as acrylamid are dispersed in a gelatin or agarose matrix. Upon radiation exposure, monomers undergo a polymerization reaction, resulting in a 3D polymer gel matrix that is a function of absorbed dose that can be evaluated using NMR, X-rays computed tomography (CT), optical tomography, vibrational spectroscopy, or ultrasound.

In literature, it is possible to find exhaustive summaries of characteristics of gel dosimeters and their possible application [46, 47].

2.3 IMPLEMENTATION IN QUALITY ASSURANCE PROCEDURES

As already pointed out in the previous paragraphs, area detectors are essential for quality assurance purposes in external beam radiotherapy, especially:

- in pre-treatment plan verification, where planar dose distributions need to be measured;
- in machine quality assurance, when dynamic measurements in which dose distribution is changing with time are needed. In this case, scanning systems with point detectors cannot be used;
- in machine quality assurance and LINAC commissioning, when there is the need to accelerate the measurement of static dose distributions beyond the capability of a scanning system.

Moreover, due to the characteristics of the treatment beams described in Section 1.1, the ideal detector should feature a small volume together with minimal energy and dose rate dependence in order to provide accurate dose information.

Methods based on dosimetry with radiochromic films [48, 49] and polymer gel [50, 51] are valuable especially because they can provide 2D and 3D dose reconstruction. Additionally, a great benefit of these types of detectors is their near water equivalence, resulting in a minimal perturbation of the radiation spectrum. On the other hand, measurements with film and gel might require complex procedures, time-consuming processes and accurate calibration workflows to obtain reliable results. Therefore, these solutions are often intended for reference measurements but not used in routinely (daily, weekly, or monthly) quality assurance controls.

Due to their efficiency, versatility, reliability, and extreme manageability, 2D detector arrays have become one of the most used solution for LINAC quality assurance [52, 53, 54]. Furthermore, they have become the standard devices for patient plan verification in intensity-modulated radiotherapy techniques [55, 56, 57]. A very well-consolidated pre-treatment plan verification procedure consists of measuring the dose with a 2D detector inserted into a phantom with simple geometry, as discussed in Section 1.2.2 [58, 59]. Besides that, there is

also an emerging market which addresses the need for online treatment verification with area detectors [60, 61, 62, 63].

It is also worth mentioning that, for both machine QA and patient QA, there are available solutions based on dose reconstruction from electronic portal imaging devices (EPID) integrated into LINACs machines [64, 65].

Features which are typically taken into account when classifying 2D detectors are the sensor type (ion chamber or semiconductor), the volume of a single sensor, the number of sensors and the spatial arrangement of sensors over the active area. In practice, the dosimetric performance of the detector strongly depends on the materials and the design, and there is always a tradeoff between performance and technical feasibility/costs.

Air-vented ionization chambers are till the gold standard for dose determination because of their low sensitivity dependence on radiation energy and their excellent stability in time. However, the air-vented ionization chambers used currently in 2D detectors often have their response influenced by volume averaging effects when the sensitive volume is large compared to the field size. It is important to point out here that in modern radiotherapy there is the reasonable trend to increase the conformity of dose distribution to the tumor (and therefore the sparing of organs at risk) as much as possible by using very steep dose gradients. Steep dose gradients can be achieved with beam modulation and/or the use of stereotactic cones. The effect of volume averaging can lead to a smoothing of such steep dose gradients as those found in typical intensity-modulated techniques [66, 67] and SRS, where high doses per fraction are delivered and the margin for errors is reduced.

Furthermore, a poor spatial resolution is responsible for dose distributions being defined inaccurately. On the other hand, the sensitive volume of each chamber should be kept large enough to ensure a good signal to noise ratio and a resultant sufficient sensitivity. Dose gradient in typical SRS beams can be in the order of 10%/mm (cf. Paragraph 4.2); the spatial resolution of commercial air-vented ion chambers detectors is typically greater than 5 mm and the volume of each sensor not smaller than 0.032 cm^3 [68].

Liquid-filled ionization chambers may represent a valid option to build detectors with smaller sensitive volume and higher sensor spatial density. This is possible due to the higher density of the sensitive medium compared to air. Detectors based on this technology have been

already introduced in the market and they have been proved to be suitable especially for dose measurements in small photon beams [69, 70]. However, the major disadvantage of liquid-filled ionization chambers is their strong dependence of sensitivity on dose rate as a consequence of the reduced ion mobility and speed, which makes them not ideal for dose measurements in stereotactic beams [69, 70, 71]. In some cases, [72] the collection time is about 9 ms, which is larger than the typical 3 ms (1/PRF) LINAC pulse period. Thus, PRF dependence is superimposed upon dose per pulse dependence.

Detectors based on diode technology have sensors with a small sensitive volume and high sensitivity, which can be arranged in a high-resolution grid. However, they may exhibit dose rate dependence and radiation energy dependence [73, 74]. The dose per pulse dependence of this detector type is due to the filling of carrier traps in the lattice, while the energy dependence is caused by the enhancement of the photoelectric effect, being the atomic number Z higher than the average one of water. The Z-effect in silicon-based detectors plays an important role in the dosimetry of small fields [75].

Moreover, silicon sensors may show a non-excellent radiation hardness (as mentioned in Paragraph 2.1.2.5), although modern construction technology has significantly reduced this weakness [76].

Indeed, detector arrays enjoy numerous advantages over point detectors in a water phantom, over films, and over gel dosimeters. They are efficient because of the simultaneous acquisition of many point doses; they are versatile, reliable and easy to set up. Currently, dose information can be projected in a 3D space through a calculation engine from measured 2D fluences. The increase of the sensors' spatial density while maintaining high dosimetric performance in the verification of complex radiotherapy techniques has become one of the most challenging tasks in modern detector technology development. Besides the sensor geometry itself, one of the major problems common to silicon-based and IC-based detectors, is the escalation of readout complexity when reducing the pitch and/or increasing the active area. While films and gels are insensitive to this problem, for silicon-based and IC-based detectors, the best compromise has to be evaluated.

Chapter 3 DEVELOPMENT OF A NEW IONIZATION CHAMBER TECHNOLOGY

To address the requirements of quality assurance in complex radiotherapy techniques, the development of a new air-vented ionization chamber technology has been carried out at IBA Dosimetry. A consolidated experience in manufacturing area detectors that are aimed to radiotherapy applications (e.g. the MatriXX sensor family [53]) represented the starting point of this process. During the development phase, three different detectors based on the new technology were built. In the following, they are referred to as *detector array v1*, *detector array v2* and *detector array v3*, considering the chronological order of manufacturing.

The project began in December, 2011 and the *detector array v1* was manufactured in October, 2012. Preliminary tests were performed in December-January, 2013. The debug phase was completed during the month of July, 2013. Section 3.1 presents the concept behind the realization of *detector array v1* and gathers together the different debug phases of the dosimetric characterization.

Detector array v2 was designed according to the outcomes of *detector array v1* characterization and assembled at the beginning of October, 2013. Section 3.2 describes the experimental evaluation of the detector until its completion in April, 2015.

The assembly of *detector array v3*, which represents the first 2D prototype based on the investigated technology, was completed in November, 2015. The proof of concept of this innovative device is further described in Chapter 6 of this work.

3.1 DETECTOR ARRAY V1

The *detector array v1* was built to prove the suitability of a new ionization chamber technology to building possible devices aimed at radiotherapy applications. Experimental assessment of its novel properties was carried out through the measurement campaign described in the following sections. Upgrades to the detector design were introduced on the basis of experimental outcomes.

3.1.1 General description

The development of a new ionization chamber technology for detector arrays comes with the already discussed necessity of a device which combines efficiency and manageability with high performances in challenging measurements conditions, such as those characterizing radiation treatments with high-intensity and time-varying parameters.

The initial detector design was chosen to primarily fulfill two key points: a small center-to-center chamber distance and a low sensitivity dependence on dose per pulse. Therefore, the pixel pitch was set to 3.5 mm and the inter-electrodes distance to 1 mm, with a nominal sensitive volume of each sensor of about 4 mm^3. If the choice of a small inter-chamber distance to achieve a high sampling resolution is self-explaining, the tiny gap between collecting electrodes allows for a reduction of the ionic recombination at an elevated dose per pulse thanks to the onset of a high electrical field in the collecting region. This aspect has been discussed in Chapter 2, Paragraph 2.2.1.1.

Other goals to be achieved with the new design were simplified detector geometry and an easy and straightforward assembly process, which would result in some practical benefits such as an increase in the production yield. Moreover, the *detector array v1* was meant to test different design solutions that are slightly different in terms of chamber geometry and pixel spatial arrangement. To accomplish this goal, *detector array v1* comes with a multi-array layout, with several one-dimensional arrays to be tested (Figure 3.1).

Technical details (drawings, materials and layout) of *detector array v1* are described in a confidential annex of this thesis. Preliminary investigations into detector properties are reported as well.

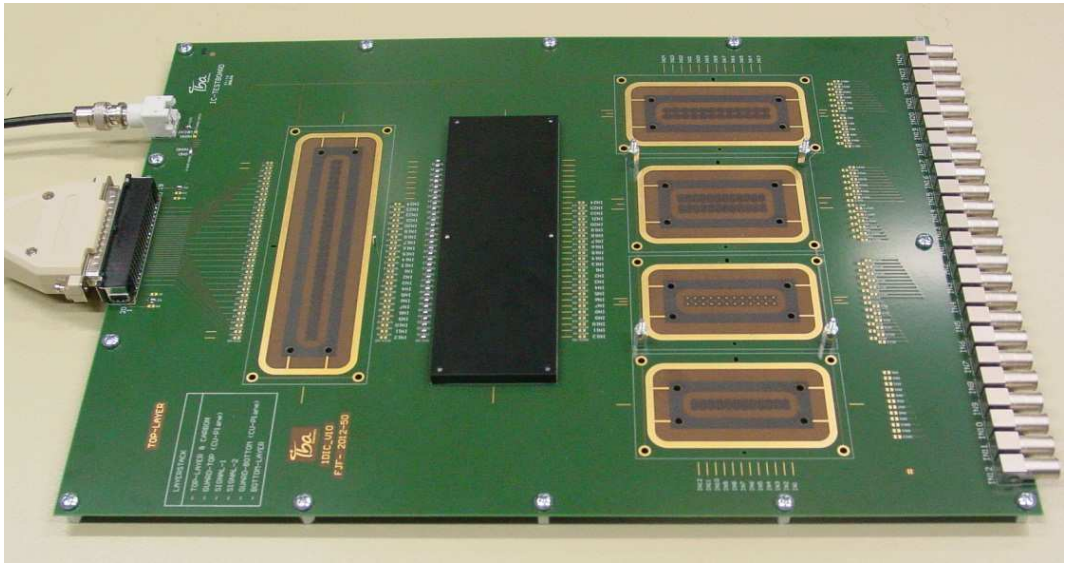

Figure 3.1. *Detector array v1* layout: multiple arrays implemented on a single printed circuit board (PCB). On PCB edges, connectors for chambers readout and bias voltage are installed.

3.1.2 Dosimetric characterization

The experimental characterization of the *detector array v1* was carried out entirely at the Secondary Standard Dosimetry Laboratory (SSDL DosLab) of IBA Dosimetry. The DosLab is equipped with several irradiation facilities. Among these, it is worth describing the three which have been used for detector testing and characterization:

- Gammatron (Siemens Medical Solutions, NC, US): cobalt source mounted on a 360° rotating gantry, with a measured kerma in air of 0.407 Gy/min at isocenter (value measured on 10.04.2014);
- Terabalt 100 (UJP Praha a.s., Prague, Czech Republic): cobalt source mounted on a 360° rotating gantry, with a measured kerma in air of 1.278 Gy/min at isocenter (value measured on 10.04.2014);
- Synergy® LINAC (ELEKTA AB, Stockholm, Sweden): medical linear accelerator equipped with ELEKTA Agility™ head (40x40 cm^2 maximum field size, MLC with 160 leaves with 5 mm width at isocenter) and featuring three flattened (6 MV, 10 MV and 15 MV) and two unflattened photon beam qualities (6 MVFFF, 10 MVFFF). The

LINAC is calibrated to deliver ~1 cGy/MU at isocenter at 10cm depth in water, with 6MV beam quality and field size of 10x10cm^2.

In the following sections, the names Gammatron, Terabalt, and Agility LINAC are used when referring to the facilities described above.

3.1.2.1 First debug phase

The assessment of dosimetric properties began with preliminary testing at Terabalt and Gammatron radiation facilities. The *detector array v1* was first tested in the configuration shown in Figure 3.1, with one linear array (consisting of 32 ion chambers) set up and connected to an Electrometer Board that was internally developed at IBA and allows for readout of very small currents. Such a device is a 2x32 channels electrometer designed for proton therapy applications (e.g. it can be connected to a monitor ionization chamber or Faraday cup in proton beams), with a minimum internal sampling period of 10 µs and a charge quantum resolution of 180 aC. The signal integration time was set to 1s. Bias was provided through an external power supply (Hamamatsu, model C3350). Figure 3.2 shows the connections between *detector array v1* and external devices, as well as the detector setup under the cobalt radiation facility.

Despite the simple setup, measurements with this configuration were found to be not reproducible due to a poor signal to noise ratio. Due to the small active volume of the ion chambers, the sensitivity of the detector is small (about 200 pC/Gy) in comparison to the typical sensitivity of compact ionization chambers (0.5–20 nC/Gy), and the amplitude of parasitic currents is not negligible in comparison to the signal. The dominant source of such parasitic signals was hypothesized to be air ions driven by the electric field generated by the applied voltage and entering any break in the guard. Based on this first outcome, it was decided to carry out additional experiments measuring the signal from a single pixel out of the complete array, using a single channel electrometer connected with a tri-axial cable. In this case, the guarding is strongly improved. In order to move to a second measurement phase, some modifications to the layout of *detector array v1* were introduced. Those improvements are described in the confidential appendix.

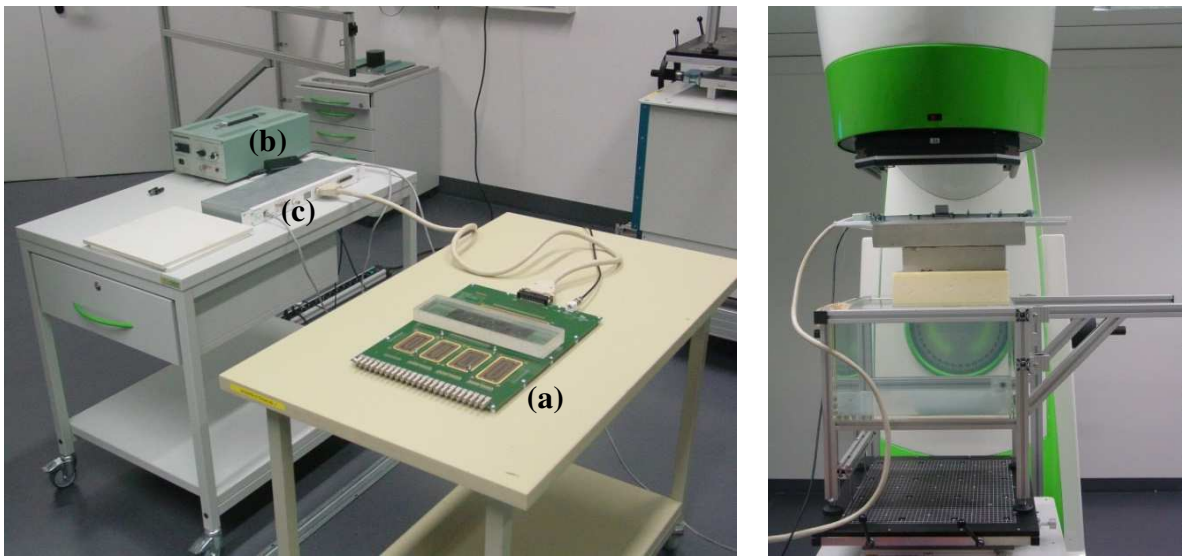

Figure 3.2. *Detector array v1* (a) connected to an external bias supply (b) and to the 32 channels Electrometer Board (c) (left). The electrometer communicates with a control laptop through an Ethernet cable. On the right, the *detector array v1* placed under the gantry head of the Terabalt facility.

3.1.2.2 Second debug phase

The improvements introduced at the end of the first debug phase were intended to achieve reliable measurement conditions and therefore more reproducible results. In particular, together with the already mentioned possibility of single chamber readout, modifications were introduced to minimize the influence of scattered radiation and to provide adequate isolation from any spurious signal. As explained in a previous discussion, the presence of parasitic currents moving through the guard was hypothesized. Such currents may originate from air ionization or ionization of insulator materials on the printed circuit board (PCB). The analyses carried out with the new detector configuration are presented in the following text.

The characterization of a single chamber dynamic response was performed both under continuous gamma radiation (at Terabalt and Gammatron facilities) and under MV X-rays pulsed beams (Agility LINAC). Gamma radiation was delivered in 2-minute-long subsequent irradiations, with approximately 20 s of waiting time in between. The choice of this time pattern ensures enough sampling points in the beam-off and beam-on periods to clearly define the rise and fall–off regions of the ionization current. Pulsed X-rays were delivered,

with subsequent irradiations consisting of 400 MU each, with a dose rate of 220 MU/min, and with approximately 20 s of waiting time again. For Pulsed radiation, a Farmer chamber (FC65-G, IBA Dosimetry GmbH, Schwarzenbruck, Germany) with a sensitive volume of 0.65 cm^3, 3.1 mm cavity radius, biased at +300 V was placed at the edge of the radiation field to monitor the time constancy of the LINAC output. Such a precaution was not adopted during tests under continuous gamma radiation, where the dose rate can be considered constant within the irradiation time and the ramp-up time (defined as the time needed to completely open the mechanical shutter which covers the source) in the order of 10^{-1} seconds.

The detector was always pre-irradiated with at least 2 Gy and the ionization current integrated over a time period of 1 s with a Keithley source-measure unit (model 6517B) that features a resolution of 10 fC. The acquisition system is based on software that was developed in house (LabVIEW System Design Software environment).

To identify the minimum polarizing voltage which determines full charge collection under continuous radiation, the single chamber signal was integrated for different applied bias voltages in the range 10–500 V.

Measurements of linear dose distributions were carried out at Terabalt unit. Signals from the array were acquired simultaneously with the 2x32 channels IBA Electrometer Board. Normalization to a large field was performed to correct for uniformity. Dose profiles were compared with those measured with an amorphous silicon flat panel (0.2 mm pixel pitch) operating in direct conversion mode.

The measured signal dynamics of a single ionization chamber under cobalt radiation is presented in Figure 3.3. A magnified detail is additionally depicted in Figure 3.4. The ionization current does not exhibit a prompt rise, despite the almost instantaneous onset of the radiation field, and two time-drift components can be clearly distinguished: a ‘fast’ component in the rising part of the signal, and a ‘slow’ component which leads to the current decreasing once it has reached its maximum intensity. The combination of these two spurious components results in a ±2% signal fluctuation over a 2-minute-long irradiation. Further tests showed that this effect even grows in magnitude when increasing the bias applied to the detector.

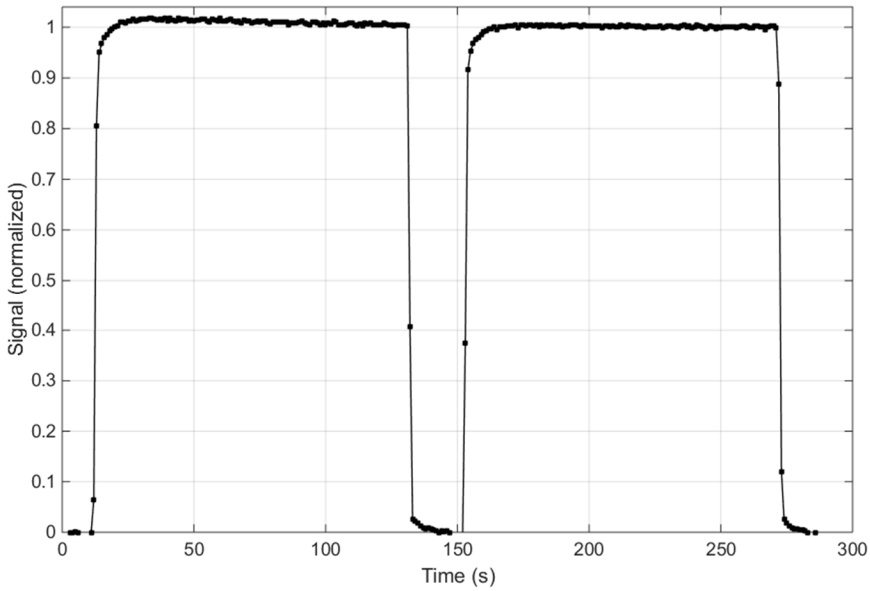

Figure 3.3. Time profile of integrated ionization current for two subsequent irradiations. Detector was biased at 100 V and the external buildup consists of 15 mm of polystyrene (RW3). The signal is normalized to the 'flat region' (i.e. from 240 s to 260 s) at the end of second irradiation. Measured dose rate is 2.2 Gy/min.

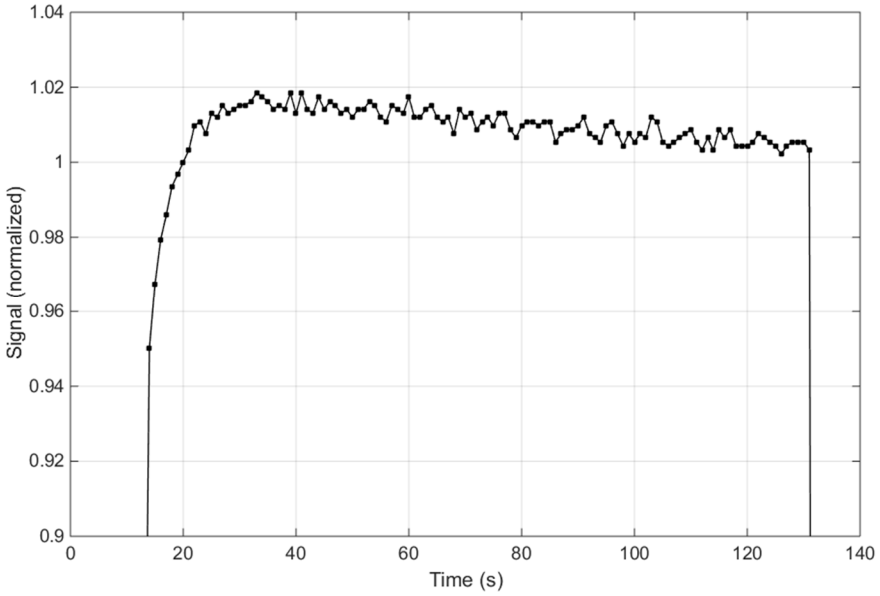

Figure 3.4. Detail of a single pixel dynamic response: the signal above the 90% of the normalization value is shown. 2 Gy of preirradiation was performed after the detector was biased. Time instability of the ionization current can be clearly identified in two components with two different time constants.

Measurements of chamber dynamic response with MV X-rays highlighted the same drifting behavior over time. Figure 3.5 clearly shows a different rising time constant for the single ion

chamber from the array and the Farmer chamber. Again, the magnitude of this effect can be correlated to the intensity of the bias applied: the higher the polarization voltage, the bigger the time instability. On the other hand, no dependence of this effect on the dose rate was observed.

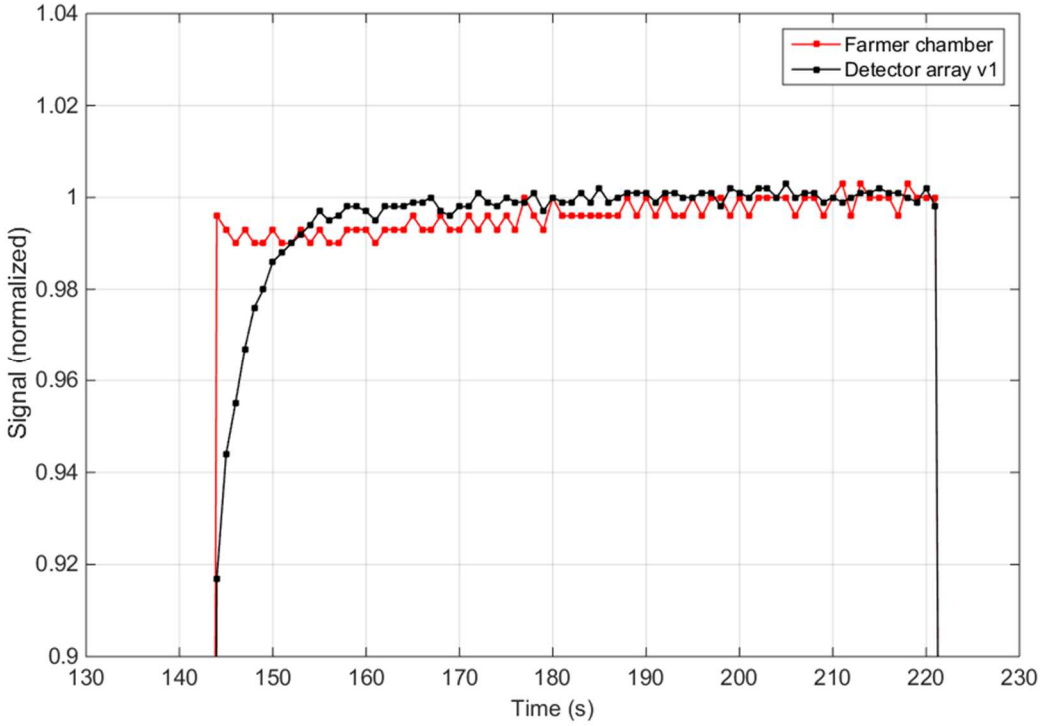

Figure 3.5. Detail of a single pixel dynamics compared to FC65-G: the signal above the 90% of the normalization value is shown. Irradiation details: array biased at 100 V, 15 MV beam energy, 220 MU/min dose rate, external buildup 15mm (polystyrene RW3), SDD 100 cm.

As a consequence of the instability phenomena observed, it was not possible to clearly identify the bias range determining full charge collection (Figure 3.6).

Preliminary measurements of dose profiles illustrate a good agreement with the reference a:Si flat panel in the flat top region, in the tails and in the penumbra regions (Figure 3.7). In particular, penumbras are very well-defined thanks to the small pixel pitch of the array.

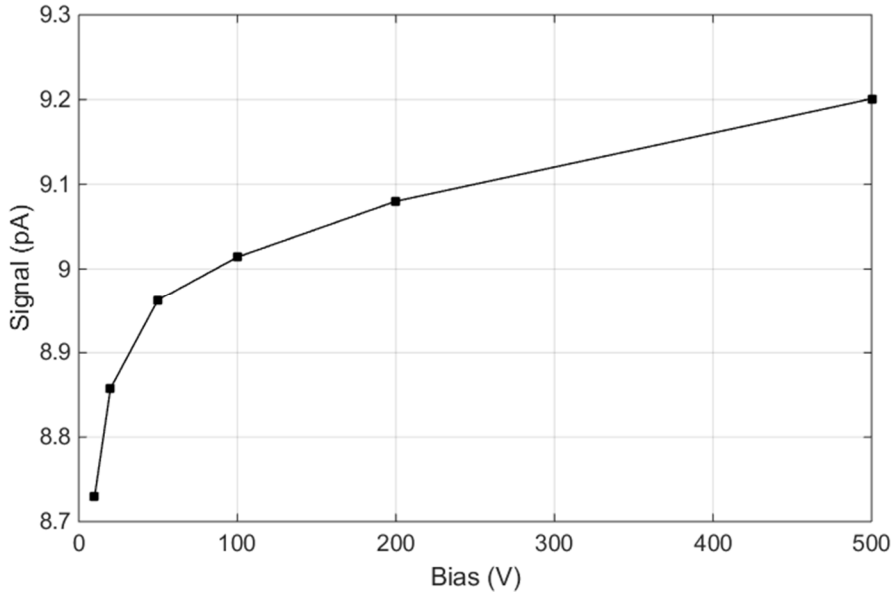

Figure 3.6. Dependence of single chamber response on the applied bias (measurement performed under continuous gamma radiation). The plateau, which corresponds to a region of full charge collection, is not noticeable.

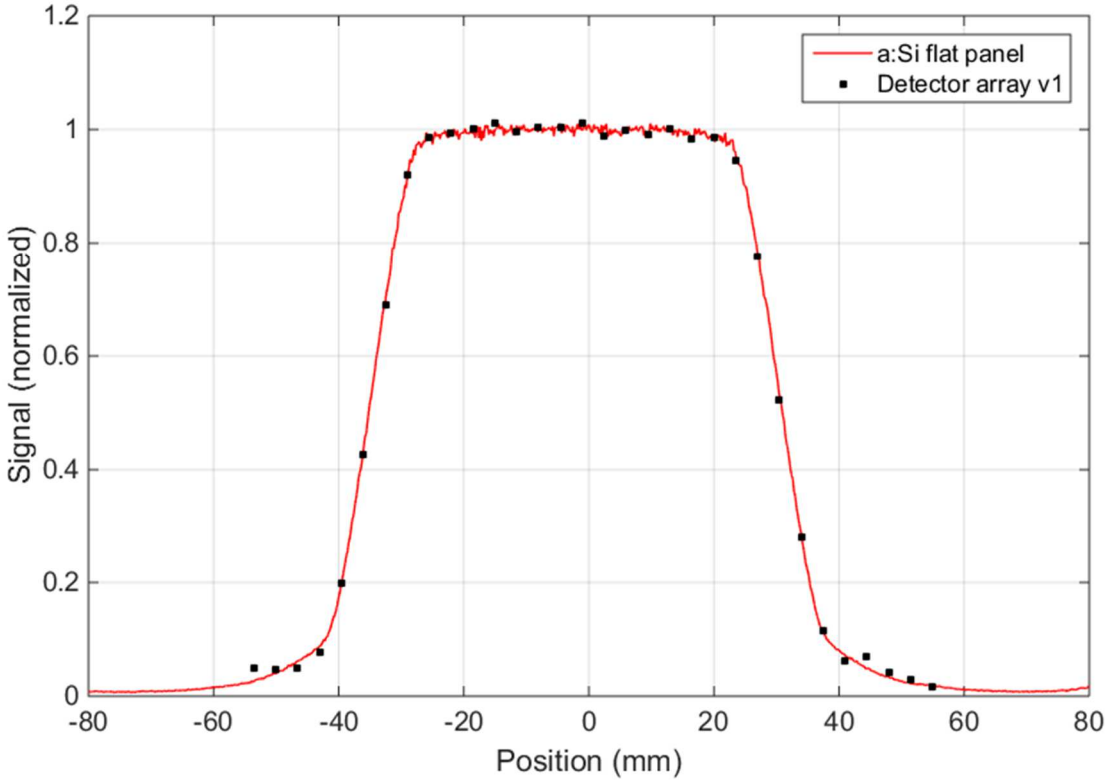

Figure 3.7. Comparison of 1D dose distributions. The nominal field width is 6.2 cm, and the external buildup consists of 15 mm of polystyrene RW3. Profiles are normalized to their maximum.

3.1.2.3 Final debug phase

The goal of the subsequent debug phase was to minimize the amplitude of the parasitic currents other than the air ionization in the chamber volume.

Therefore, the *detector array v1* configuration was modified once more in order to finally achieve stable and reproducible measurement conditions. A manufactured new sensor was used to accomplish this purpose. Changes were introduced to remove any floating conductor within guard planes in the PCB. These changes are described in the confidential appendix.

The dynamic characterization of the array single chamber was then performed in the same experimental conditions reported in Section 3.1.2.2: gamma radiation delivered in 2-minute-long subsequent irradiations with 20 s of waiting time in between, 2.2 Gy/min measured dose rate, and the detector biased at 100 V with 15 mm external buildup of RW3.

Significant improvements in terms of signal time stability were obtained. The ionization current, continuously integrated over a period of 1 s, exhibits both a prompt rise and prompt fall, and its standard deviation over the complete irradiation time is 0.2%.

A direct comparison with the results previously presented in Figure 3.3 is shown in Figure 3.8: drift effects related to parasitic signals are completely eliminated.

Preliminary measurements of the saturation curve under ^{60}Co radiation showed nearly full collection efficiency already when 50 V bias was applied (Figure 3.9).

3.1.3 Discussion

In the preliminary characterization phase of the investigated ionization chamber technology, a prototype named *detector array v1* was built and tested. A three-step approach was followed during the testing process, which consists of a first assessment of detector performance, a subsequent improvement of its design and configuration based on hypotheses which explain unexpected behaviors, and finally an experimental proof of the applied improvements. The same approach was adopted through the whole characterization process of the technology.

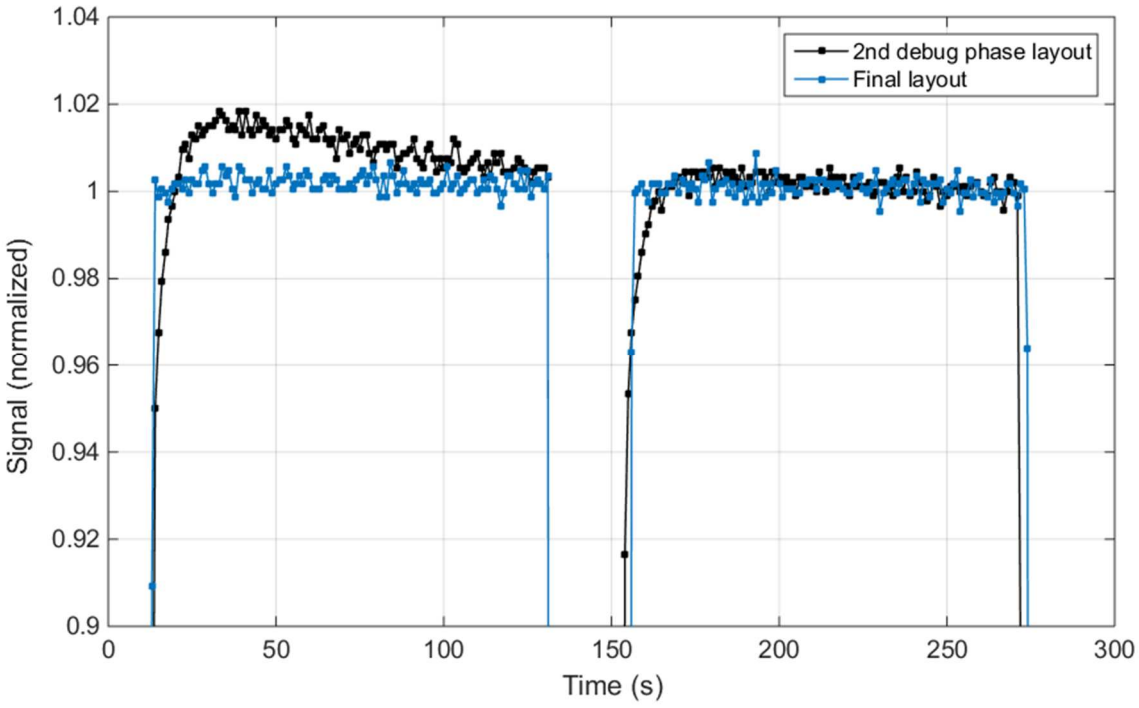

Figure 3.8. Comparison between detector dynamic responses: during the second debug phase (black curve) and after the final layout modifications (blue curve). Only the signal above the 90% of the normalization value is shown. The same normalization procedure was followed.

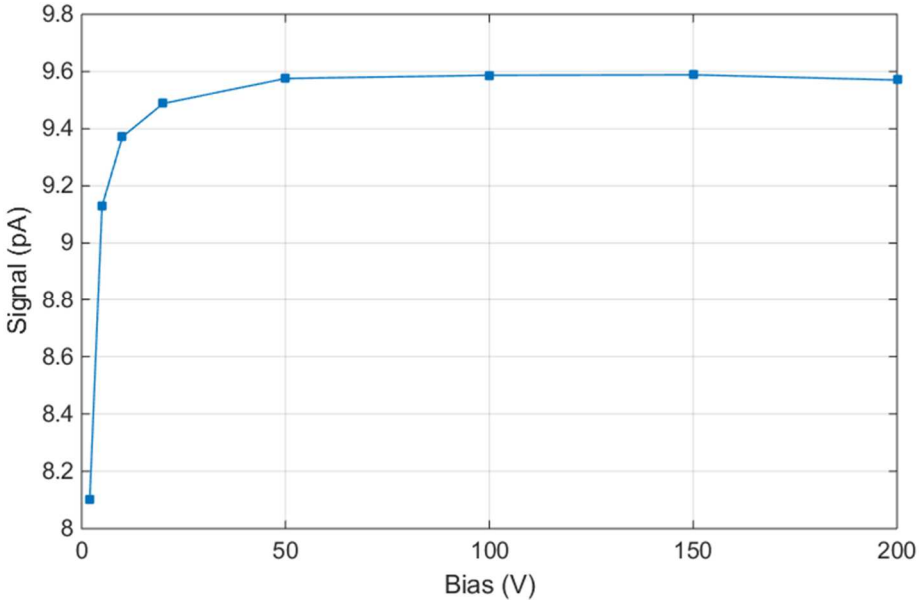

Figure 3.9. Saturation curve of the single pixel ionization current under continuous gamma radiation.

The first step was to evaluate the performances of the built prototype under continuous gamma radiation, to exclude any possible influence of a non-stable radiation source on the

ionization current. The detector layout was changed step by step, by simplifying the initial design to eliminate different sources of instability. In parallel, an investigation into the properties of the electrical field generated in the sensitive volume of the chamber was carried out (cf. confidential appendix).

At the end of this first step, the feasibility of the new technology to perform reliable and reproducible measurements under gamma and MV X-rays radiation was proven. Despite the small active volume of each chamber and the consequent low sensitivity, the ionization current was found to be free from parasitic signal. The sensor dynamic response to radiation was characterized by a prompt rise and fall-off, as well as by a highly stable behavior over the irradiation period.

Through the complete experimental investigation of *detector array v1*, several rules for an improved design of the detector were identified. These general guidelines and the experience acquired were applied in the conceptualization of the subsequent detector, the *detector array v2*, and are summarized in the confidential appendix. For instance, major constraints were found in the design of the printed circuit board through which the signal from the chambers is routed.

3.2 DETECTOR ARRAY V2

On the basis of the experience gained with the characterization of *detector array v1*, a new detector named *detector array v2* was built with the following purposes:

- to consolidate the achievements reached with *detector array v1* and to implement all the design rules that lead to reproducible measurement conditions;
- to introduce a new multi-channel low-noise front end electronics;
- to produce a device suitable (i.e. reproducible, compact and sufficiently manageable) to perform independent tests at clinics.

The dosimetric characterization of this new device is described in the following paragraphs, while the tests to assess its suitability to real clinical applications are reported in Chapter 4 and Chapter 5.

3.2.1 General description

The array *detector array v2* features 80 air-vented ionization chambers with a 3.5 mm center-to-center chamber distance, resulting in a total active length of 276.5 mm. The chamber geometry can be described well using parallel plate geometry, with a 4x1 mm^2 rectangular cross-section and a 1 mm distance between the electrodes, resulting in a nominal sensitive volume of about 4 mm^3 as for *detector array v1*.

The collecting electrode consists of a graphite print on the surface of a printed circuit board (made of glass fiber reinforced with resin, about 1 mm thick). The overall thickness of the copper conductive planes in the inner layers of the printed circuit board is about 120 μm. The other electrode closing the chamber volume is made of carbon-loaded plastic and provides an intrinsic buildup thickness of 5 mm.

The read-out electronic system is based on a commercial electrometer with 128 channels and a resolution practically limited by noise (1.3–1.7 fC rms when coupled with the sensor). With such readout electronics, it is possible to achieve high values of signal to noise ratio even when the ionization current from the chambers is in the order of a few pA. The detector was still biased through an external high voltage supply to avoid possible induced leakages.

As for *detector array v1*, the technical details (drawings, materials and layout) of *detector array v2* are described in detail in the confidential appendix of this thesis.

3.2.2 Dosimetric characterization

The dosimetric characterization of *detector array v1* was performed at IBA Dosimetry DosLab, either by using the plastic phantom MultiCube (IBA Dosimetry GmbH, Schwarzenbruck, Germany) (Figure 3.10–bottom) or by adding RW3 layers upstream of the detector (Figure 3.10–top). In the latter case, a few centimeters of RW3 slabs were placed downstream of the linear array to provide adequate backscatter material. An RW3 water adaptor was fabricated in order to fit the geometry of the detector to the MultiCube, to facilitate the piling of RW3 plates, and to obtain a homogenous extrinsic buildup.

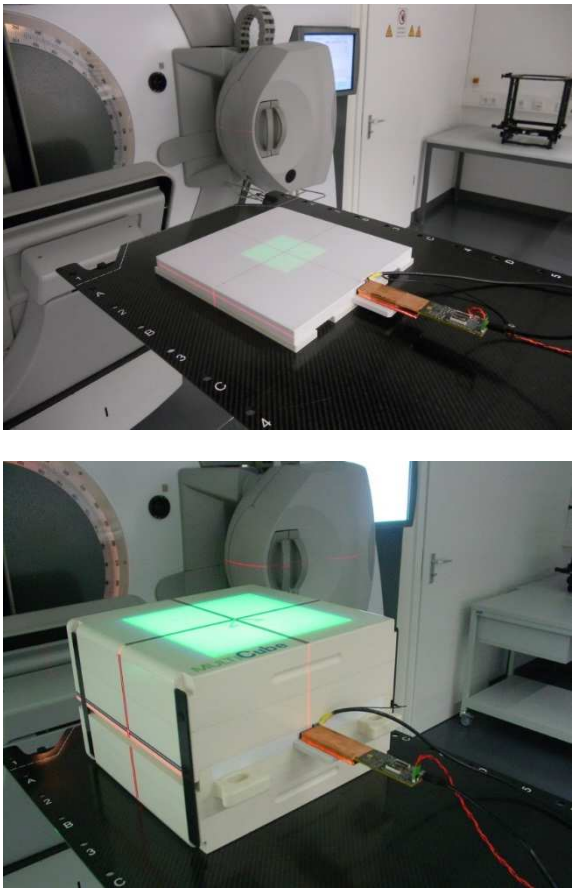

Figure 3.10. Top: the *detector array v2* placed in the RW3 adaptor. Bottom: the *detector array v2* and the adaptor placed inside MultiCube plastic phantom.

3.2.2.1 Experimental methods

The dynamic response of chambers was evaluated with continuous gamma radiation to assess the effectiveness of the improved design in achieving an adequate time stability of the signal.

To measure repeatability, reproducibility and dose linearity, the *detector array v2* was placed under the ^{60}Co beam generated by the Terabalt facility at a water-equivalent depth of 1.1 cm, a source to detector distance SDD=82.2 cm, and a dose rate R=2.29 Gy/min. Repeatability was measured as a function of delivered dose under continuous irradiation to evidence the presence of any possible drift effects. The response of each pixel was binned with a variable time period t, corresponding to the dose $R \cdot t$. Repeatability $\sigma(R \cdot t)$ is evaluated as the standard deviation of the response integrated over the period t. It is worth mentioning here that the effects related to the switching on and off of radiation are not accounted for in the repeatability evaluation, although they are included in the reproducibility measurements.

Reproducibility for all of the 80 chambers was calculated as the standard deviation of 10 identical measurements taken during a day, in which the dose D=2 Gy was delivered. The setup was dismounted and remounted before each measurement. To evaluate long term stability, the same ^{60}Co profile was measured every two weeks over an 8-month-long period.

The linearity was evaluated in terms of residual from linear regression of measurements in the dose range 0.1–10.7 Gy. For all tests with ^{60}Co, the reference detector to measure dose to water was a Farmer-type ionization chamber (FC65-G, IBA Dosimetry GmbH, Schwarzenbruck, Germany) with a sensitive volume of 0.65 cm^3, a 3.1 mm cavity radius, and biased at +300 V.

To determine the optimal bias and to evaluate the sensitivity dependence on dose per pulse, *detector array v2* was irradiated with MV X-rays produced by the Agility LINAC. The charge collection efficiency of the detector versus bias was assessed in the most critical case (that is with 2.67 mGy/pulse – 10 MVFFF, SDD 59 cm, 3 cm depth of measurement) by changing the polarization voltage in the range 10–400 V. The evaluation of the charge collection efficiency was based on Boag's theory, as presented in Section 2.2.1.1, and experimental results were compared with the theoretical model valid for a parallel plate

geometry. After this test, the optimal bias of 250 V was determined and used in all subsequent measurements.

Sensitivity dependence on dose per pulse was evaluated by changing both the SDD (59 cm, 77 cm, 100 cm, and 150 cm) and the beam quality (6 MV and 10 MVFFF), in order to cover a wide range of dose per pulse values (0.09–2.67 mGy/pulse). The nominal field size was adjusted at each SDD to always have a 10x10 cm^2 field at the plane of the detectors. In this way, measurements are not influenced by spectrum variations. The reference detector was a compact chamber (CC04, IBA Dosimetry GmbH, Schwarzenbruck, Germany) with a 0.04 cm^3 active volume, a 2.0 mm cavity radius and +500 V polarization voltage. An independently evaluated correction was used to account for the loss of charge collection efficiency of the compact chamber at high dose per pulse (measured efficiency was 99.34% at 2.67 mGy/pulse).

The directional dependence of the *detector array v2* as a function of the irradiation angle was assessed by placing the detector inside a compact RW3 phantom (Figure 3.11) and by delivering a 10x10 cm^2 open field with 6 MV beam quality. For each selected gantry angle, the response of the central pixel was compared with a CC13S thimble chamber (IBA Dosimetry GmbH, Schwarzenbruck, Germany) that features a sensitive volume of 0.13 cm^3 and a 3.0 mm cavity radius, biased at +300 V.

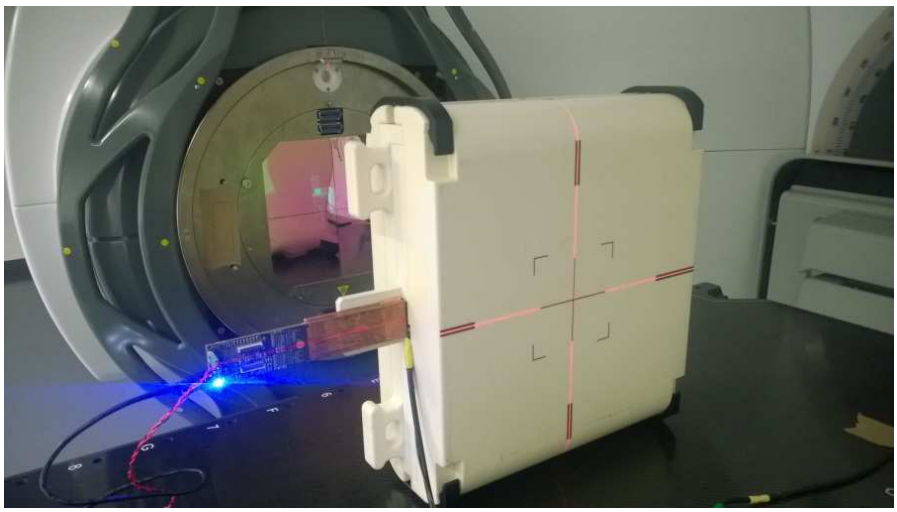

Figure 3.11. *Detector array v2* in a compact RW3 phantom for angular dependence evaluation (gantry at -90°). The phantom rests on its side to avoid irradiating through the couch.

The statistical uncertainty in the experimental data was evaluated as the standard deviation over a set of measurements, including errors in assembling the setup. The statistical uncertainty was found to be below 0.5% in all cases.

3.2.2.2 Experimental results

Signal dynamics exhibit a prompt rise and fall-off and a very stable value during the time the radiation is delivered (Figure 3.12). Fluctuations of the ionization current are in the order of 0.3% (1σ) of the average value. The long-term stability evaluated for each pixel (Figure 3.13) was consistenly within 0.5% (1σ). The repeatability under continuous irradiation was found to be under 0.3% (1σ) for all the 80 pixels of the detector. In Figure 3.14, for the sake of clarity, only 10 ionization chambers are shown. The integrated dose covers a wide range of values, from 0.2 Gy to 20 Gy.

The measured reproducibility with 2 Gy delivery was 0.2%. In Figure 3.15, the acquired ^{60}Co beam profile is shown, with a delivered dose of 2 Gy, normalized to the maximum. The error bars applied at each point represent the standard deviation (reproducibility) over 10 subsequent measurements.

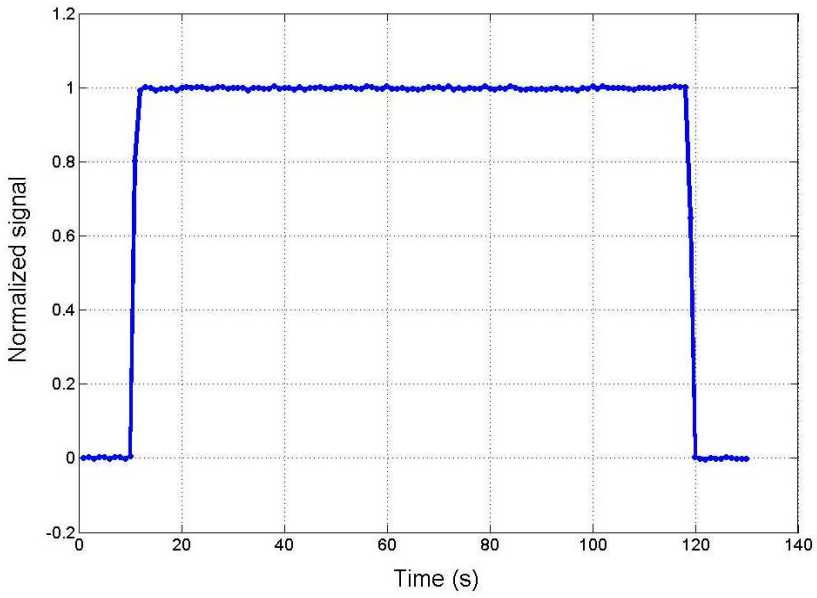

Figure 3.12. Dynamic response of a single chamber from the *detector array v2*. Integration time is about 0.8 s, signal is normalized to the average value of the plateau (absolute current value about 10 pA, dose rate 2.29 Gy/min).

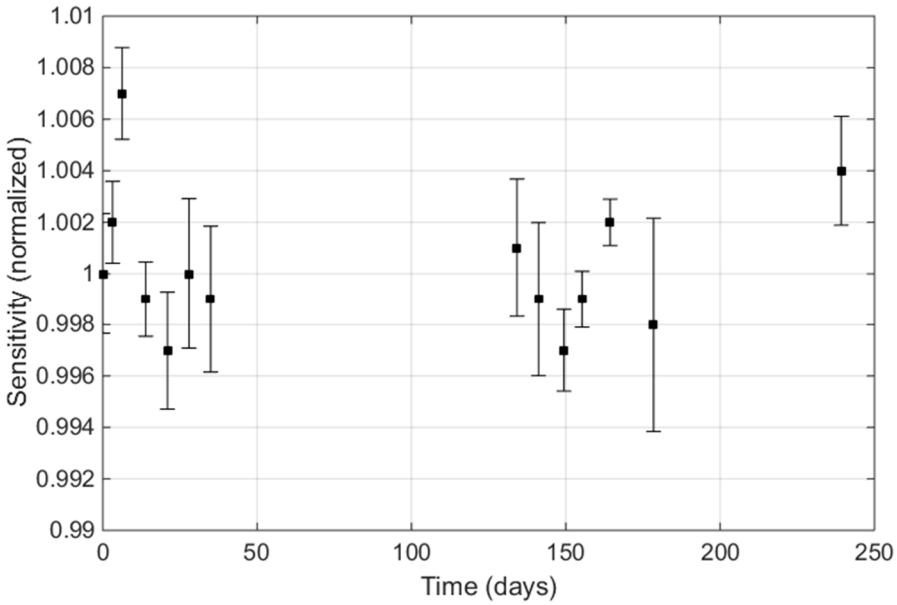

Figure 3.13. Sensitivity dependence with time of the central pixel of *detector array v2*. Measurements were performed over a period of approximately 8 months. For each measured point in the graph, the same measurement conditions were reproduced and measurement performed 10 times, with the system setup assembled and disassembled after each acquisition.

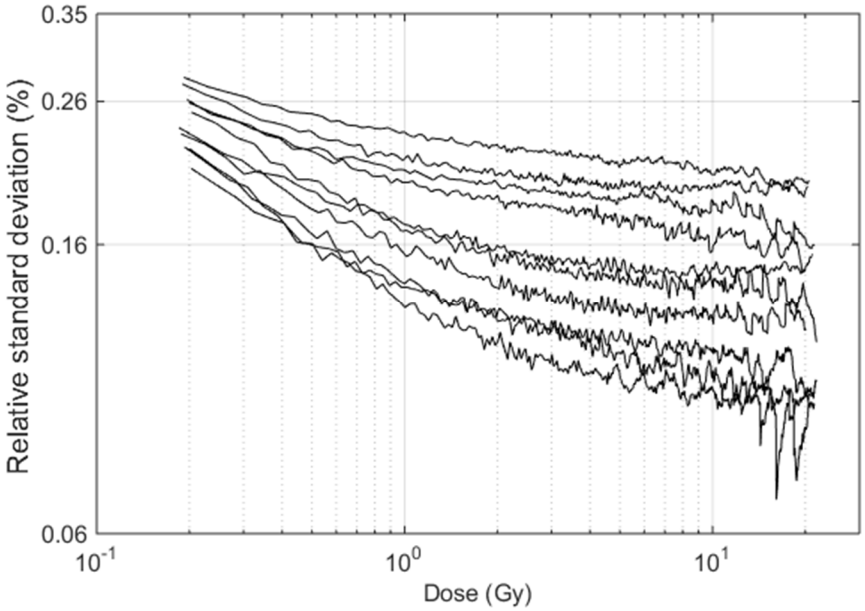

Figure 3.14. Repeatability measured with ^{60}Co. Each curve represents the relative standard deviation of the detector signal for different values of integrated dose. Short term stability is shown only for 10 pixels for clarity, which represent the range of σ for all the other pixels of the detector. Uniformity correction is not applied to these measurements.

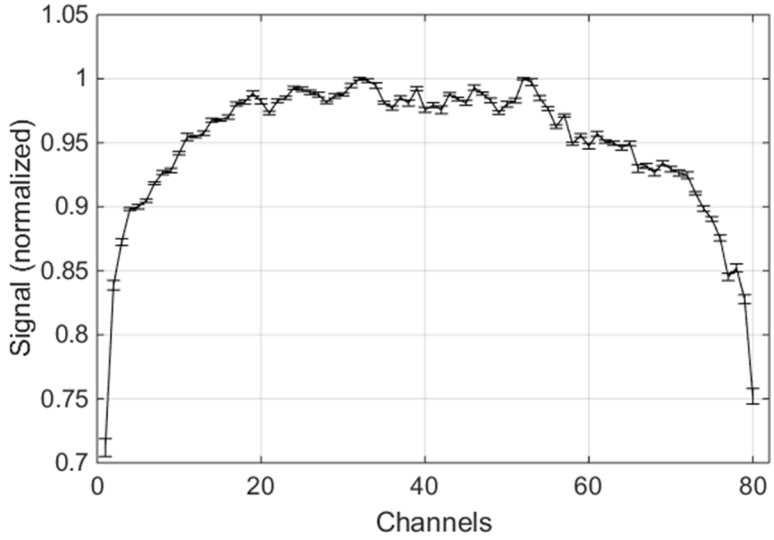

Figure 3.15. ^{60}Co beam profile acquired with the *detector array v2*. The uniformity correction is not applied to the measurement.

The detector response as a function of the dose is linear, within 0.3% for 20 cGy or more (Figure 3.16), with the exception of a deviation of about 0.9% that was observed for an integrated dose of 53 cGy. This can be explained by a limitation of the detector acquisition system. Deviation from linearity increases below 10 cGy (1.5% is measured at 9cGy).

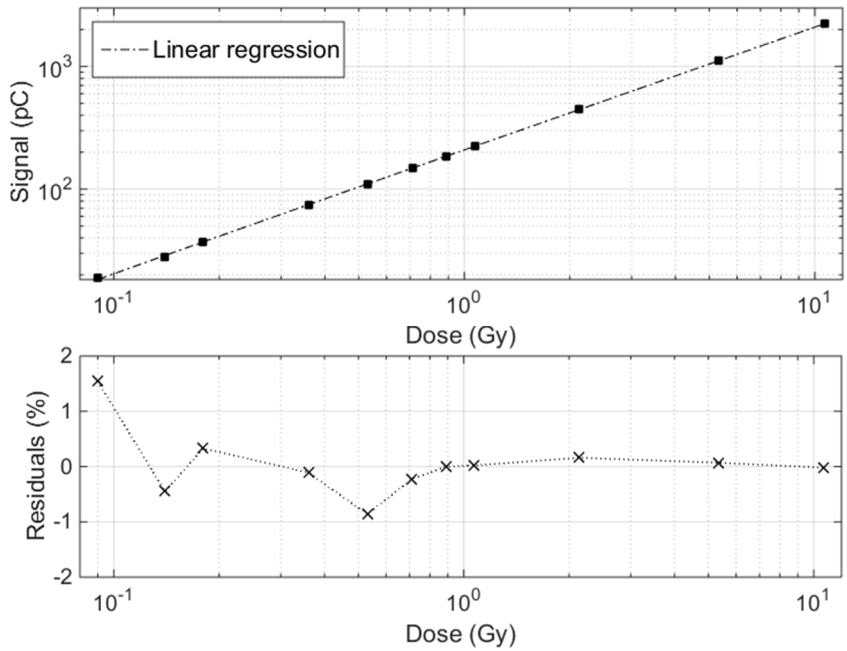

Figure 3.16. Integrated charge as a function of integrated dose (top) and percentage residuals from a linear regression fit (bottom).

The charge collection efficiency was measured with the highest value of dose per pulse achievable with the Agility LINAC without the flattening filter, and therefore with the highest rate of ion recombination in the sensitive volume. Based on the theory of recombination discussed in Section 2.2.1.1, the theoretical efficiency of the detector was calculated as a function of the dimensionless variable u (Figure 3.17). Signal at 100% charge collection was estimated through a linear fit of signal versus 1/bias (inset in Figure 3.18), according to Boag's theory [41]. Measured charge collection efficiency is already higher than 99% at 150 V, reaching 99.5% ±0.3% at 250 V. In Figure 3.18, the comparison between the measured and the theoretical saturation curve as a function of applied bias is also shown. The agreement is always within the experimental uncertainty, with the exception of the point at 10 V. Further investigations revealed that a value of 500 V is the maximum applicable polarization before the onset of electrical discharges in the chamber volume. In light of these results, a 250 V bias has been chosen as the optimal one for all subsequent tests.

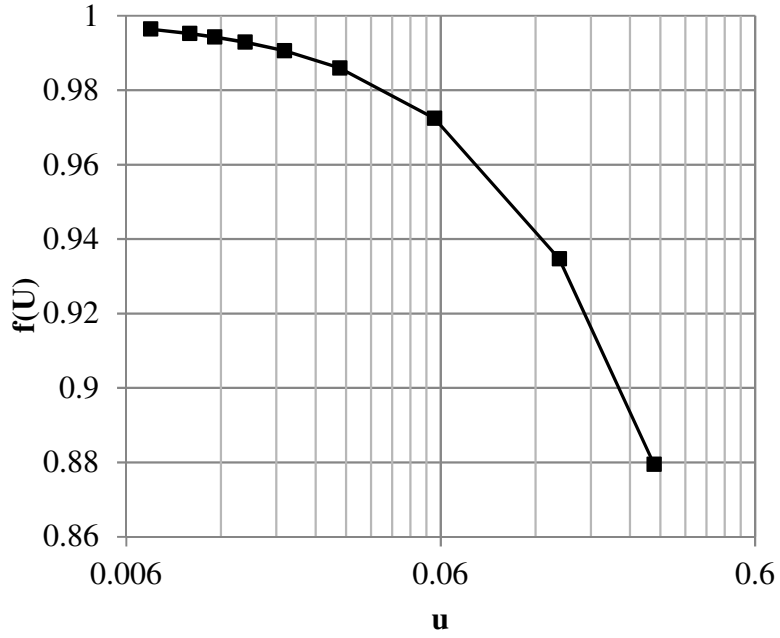

Figure 3.17. Theoretical collection efficiency for *detector array v2* as function of dimensionless variable u (cf. Section 2.2.1.1). Parameters taken into account for the theoretical prediction are: 250 V bias, dose per pulse=2.67 mGy, charge density per pulse=$9.47 \cdot 10^{-5}$ C/m^3, inter-electrode distance=1mm, air density=1.20484 kg/m^3, air ionization potential=33.97 eV/ion. The value of the recombination coefficient μ=$3.02 \cdot 10^{10}$ (Vm)/C, which takes into account the ionic mobility in air, has been chosen following the recommendations of ICRU report 34 [42] and considering the fraction of free electron collection negligible.

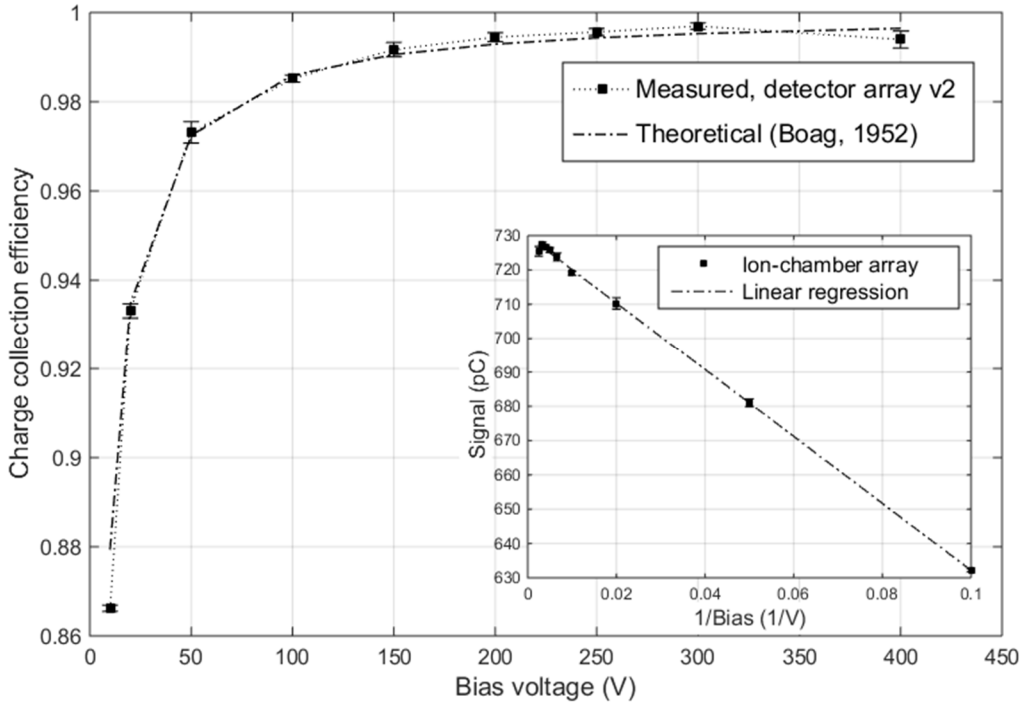

Figure 3.18. Measured and theoretical saturation curves are in good agreement: a deviation from the model is observed only at very low values of polarization. The inset in the graph shows the linear relationship between saturation current and inverse chamber bias.

The dose per pulse dependence was evaluated with two different beam qualities: 6 MV and 10 MVFFF (Figure 3.19). The values displayed for sensitivity are normalized to a common point (0.5 mGy/pulse) in order to cancel out effects related to energy dependence. Sensitivity was calculated by taking the ratio between measurements performed with the *detector array v2* and CC04 measurements. The dose rate dependence is within 0.3% up to about 1 mGy/pulse, which is the range of dose per pulse typically found at isocenter in clinical routines. A maximum deviation of about 0.9% was found if the dose per pulse range is extended to 2.7 mGy/pulse.

The *detector array v2* response as a function of the irradiation direction (Figure 3.20) shows a maximum deviation from the compact chamber of about 16% for angles between -90° and -30°. In addition to the angular dependence of the parallel plate chambers, this deviation includes asymmetry and inhomogeneity of detector construction. In patient plan quality assurance, the latter are taken into account by the CT scan and only the former components affect plan evaluation.

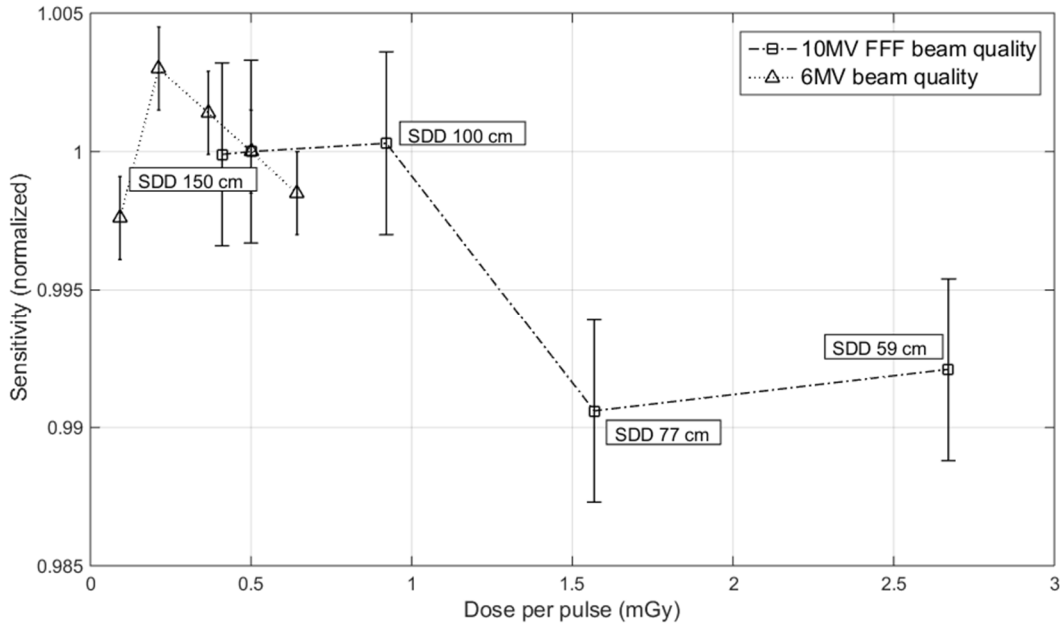

Figure 3.19. Sensitivity dependence on dose per pulse of *detector array v2*. Dose per single pulse was changed by changing both SSD and beam quality.

3.2.3 Discussion

Detector array v2 constituted the first attempt to build a detector based on the technology under investigation that could be used to perform reliable and comprehensive dosimetric measurements. The major properties which were required are: stability with time and dose, reproducibility, and linearity with dose and dose rate.

Moreover, this prototype starts to include some of the characteristics that will be part of a final commercial product, such as a large sensitive region (even though only unidimensional) and a fast, low-noise frontend electronics.

Basic dosimetric properties were assessed through continuous gamma ray irradiation. The ionization current coming from the chambers exhibited high time stability despite the very low sensitivity due to the 4 mm^3 active volume. Long-term stability and reproducibility were found to be 0.5% and below 0.3%, respectively. A good stability was expected, due to the adoption of ionization chamber technology. Deviations from dose linearity are below 1.0% for doses higher than 20 cGy and no larger than 1.5% down to 5 cGy. Dose linearity is presently limited by the performance of the readout electronics, which is suboptimal for

measurements at low doses with small chambers. An optimized version of the acquisition system will be implemented in the subsequent detector prototype (*detector array v3*).

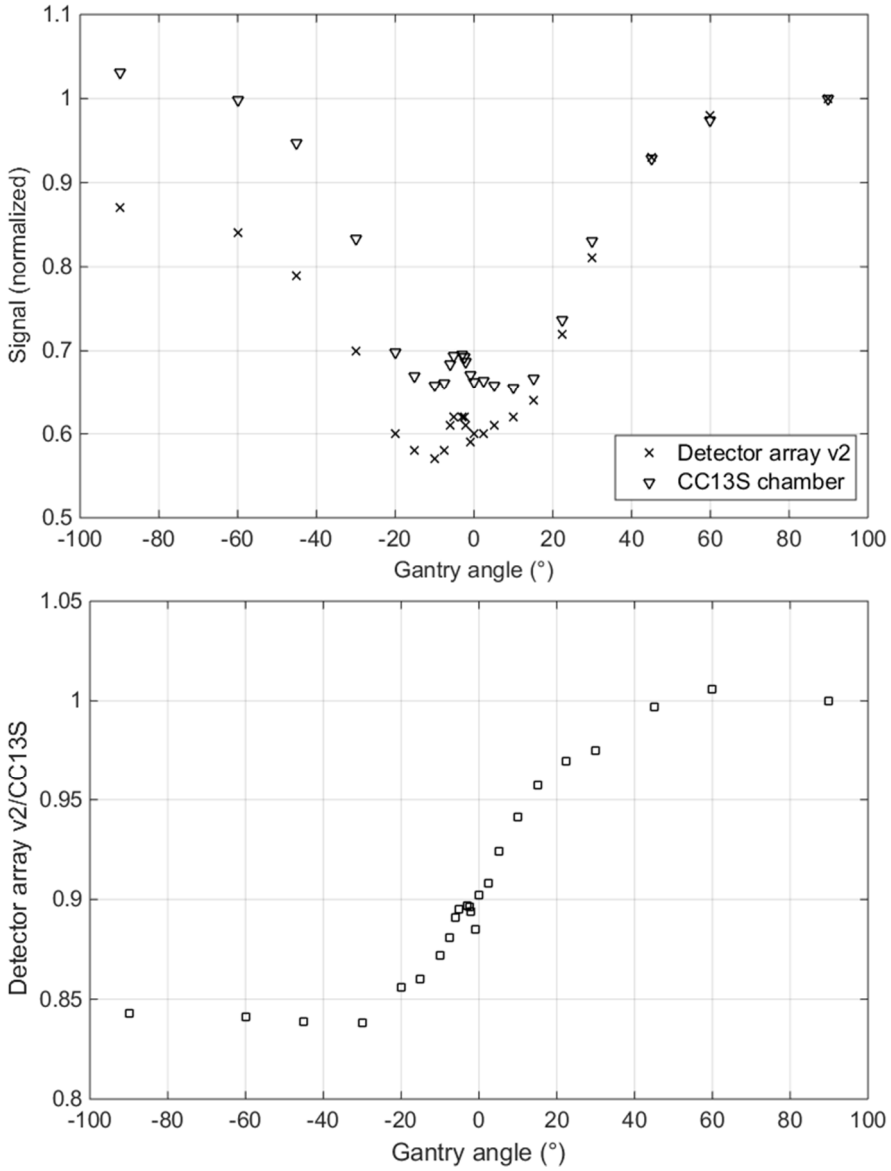

Figure 3.20. Directional dependence measurement for both detectors (top) and expressed as the ratio between *detector array v2* signal and thimble chamber signal (bottom) as a function of the gantry angle (data are normalized to +90°). The angular dependence was investigated in the range -90°–+90°, where +90° means normal incidence on array top surface.

The measured charge collection efficiency of the *detector array v2* at 2.7 mGy/pulse is 99.5% ±0.3%, which is achieved with a bias (250 V) that is 50% of the maximum applicable one (500 V). A significant agreement (always within experimental uncertainty) was found

between the measured efficiency curve and the analytical model derived from Boag (cf. Section 2.2.1.1).

The high-charge collection efficiency determines a moderate dose per pulse dependence of the *detector array v2*, which is better than 0.3% in the range 0.1–1.0 mGy per pulse and never exceeds 0.9% up to 2.7 mGy per pulse at 250 V. In other studies into chamber arrays, 0.4% maximum deviation in the range 0.2–1.0 mGy per pulse has been reported, with 3 mm chamber height biased with 1000 V [54] and 1.5% at 2.0 mGy per pulse with 2 mm chamber height biased at 500 V [77].

The sensitivity of the chambers exhibits a clear angular dependence, which is similar to that reported in previous studies into arrays with parallel plate chamber geometries [77]. In particular, the sensitivity decreases by about 16% if radiation is delivered through the bottom detector surface. This dependence includes the effects of asymmetries and inhomogeneity in the detector design (which are taken into account by the TPS in patient plan quality assurance), as well as the angular dependence of the chambers (which can be compensated by angular correction factors). Since the prototype under investigation is not optimized for plan verification, an attempt to evaluate these correction factors was not performed. Correction factors for the 2D ion chamber array used as a reference for some studies in this thesis (cf. Chapter 4), which is based on parallel plate chamber geometry, are in the range ±7% [78]. One can expect similar values for the *detector array v2*.

Based on the outcomes of this investigation, it is possible to conclude that the *detector array v2* exhibited all the dosimetric properties which are typically associated with air-vented ionization chambers, combined with a small center-to-center chamber distance and a remarkable independence of sensitivity to dose per pulse. These features provided a solid base to consider the investigated technology ready for extensive clinical tests. The detector was then characterized with MV X-rays and proton clinical beams, thanks to the collaboration with different partner institutions. Chapter 4 and Chapter 5 consist of detailed reports on these further investigations.

As highlighted in the List of Publications at the end of this thesis, some of the results shown in this chapter were presented at international medical physics congresses.

Chapter 4 DETECTOR ARRAY V2 CLINICAL CHARACTERIZATION WITH MV X-RAYS

To further characterize the new ion chamber technology and assess its feasibility with regards to quality assurance procedures in radiotherapy, several measurement campaigns were carried out at different institutes.

This chapter deals with the experimental characterization performed with clinical MV X-rays at the IBA Dosimetry DosLab, at the Klinikum rechts der Isar (Munich, DE), and at the University of California San Francisco (UCSF) hospital (San Francisco, US, CA). Klinikum rechts der Isar is equipped with a Trilogy® (Varian Medical Systems, Palo Alto, CA, US) LINAC, while UCSF is equipped with a TrueBeam™ (Varian Medical Systems, Palo Alto, CA, US) LINAC. Both Varian LINACs feature a HD120 MLC.

In Section 4.1, the outcomes of machine QA measurements are described. These measurements include the verification of depth dose curves, LINAC output factors, and beam profiles.

Section 4.2 refers to patient plan QA, and outlines data measured with the *detector array v2* are compared with different commercial detectors and benchmarked to films that are considered the reference for such application. Comparison of linear dose distributions is carried out to assess the suitability of the chamber technology for patient plan QA, even if a 2D analysis would be more appropriate in clinical applications.

4.1 MACHINE QUALITY ASSURANCE

As already discussed in Section 1.2, quality assurance controls are fundamental in ensuring that an accurate treatment is given to the patient. Machine QA also represents an invaluable and mandatory method to ensure the accuracy of dose delivery and to identify machine errors or discontinuity in machine parameters. For instance, the replacement of major components may alter machine performance from original parameters, and gradual changes may appear as a result of the aging of the machine components.

The suitability of *detector array v2* to machine QA was investigated with two different linear accelerators: the Agility LINAC at IBA Dosimetry DosLab and the TrueBeam™ LINAC at UCSF. Three different machine QA quantities were measured:

- Tissue to phantom ratio (TPR);
- Output factors;
- Beam profiles.

4.1.1 Tissue to phantom ratio

Measurements of percentage depth dose (PDD) curves along the central beam axis are part of the commissioning process. However, they must be repeated periodically, especially after accelerator maintenance. Typically, when a PDD has been measured, it is compared with the curve recorded during commissioning.

The dose distribution is typically measured along the central axis and normalized to D_{max}=100% at the depth of dose maximum z_{max}, before being referred to as the PDD distribution. Thus, the PDD is described by the relation

$$PDD\left(z, A_Q, f, hv\right) = 100\,\frac{M_Q(z, A_Q, f, hv)}{M_P(A_Q, f, hv)} \quad [\%] \tag{4.1}$$

where A_Q is the field size at the depth z in the phantom, M_Q is the measured signal proportional to the dose at point Q at depth z, and M_P is the measured signal at point P which corresponds to D_{max}. f and hv are the values for SSD and beam energy, respectively. The geometry for PDD measurement is represented in the diagram in Figure 4.1. PDD curves are

measured in water tanks, keeping the SSD constant and moving the detector in order to incrementally increase the SDD.

To simplify the measurement process, Tissue to Air Ratio (TAR) and Tissue to Phantom Ratio (TPR) were introduced and defined by the following relations:

$$TAR(z, A_Q, f, hv) = \frac{M_Q(z, A_Q, f, hv)}{M_Q{}'(z, A_Q, f, hv)} \tag{4.2}$$

where M_Q is the measured signal proportional to the dose at point Q at depth z in the patient or phantom, and $M_Q{}'$ is the measured signal proportional to the dose at the same point Q in a small mass of water in air;

$$TPR(z, A_Q, f, hv) = \frac{M_Q(z, A_Q, f, hv)}{M_Q^{ref}(z, A_Q, f, hv)} \tag{4.3}$$

where M_Q is the measured signal proportional to the dose in a phantom at arbitrary point Q and M_Q^{ref} is the measured signal at a reference depth in a phantom. For megavoltage X-rays produced by high-energy LINACs, measuring the TAR is challenging due to the difficulties in measuring the 'dose to small mass of water in air' at those energies (the required size of the buildup cap for the ionization chamber becomes excessively large). Thus, TPR curves are typically measured when assessing the absolute absorbed dose in a medium. The beam quality is specified by $TPR_{20,10}$, which is the ratio of the absorbed doses at depths 20 cm and 10 cm, both measured in SDD of 100 cm and a field of 10x10 cm^2 at the plane of the chamber. The conversion of $TPR_{20,10}$ into $PDD_{20,10}$ for MV photons beams is illustrated in different works in literature [79, 80]. For instance, a simple empirical equation obtained from a sample of almost 700 accelerators is reported in the code of practice TRS 398 [39]:

$$TPR_{20,10} = 1.2661 \cdot PDD_{20,10} - 0.0595 \tag{4.4}$$

It is important to mention here that, in the characterization process of a dosimeter, the tissue to phantom ratio curve is an effective indicator of the detector sensitivity to low-energy scattered radiation. Indeed, the contribution of low-energy photons to the total signal increases alongside the depth of the point of measurement inside the phantom.

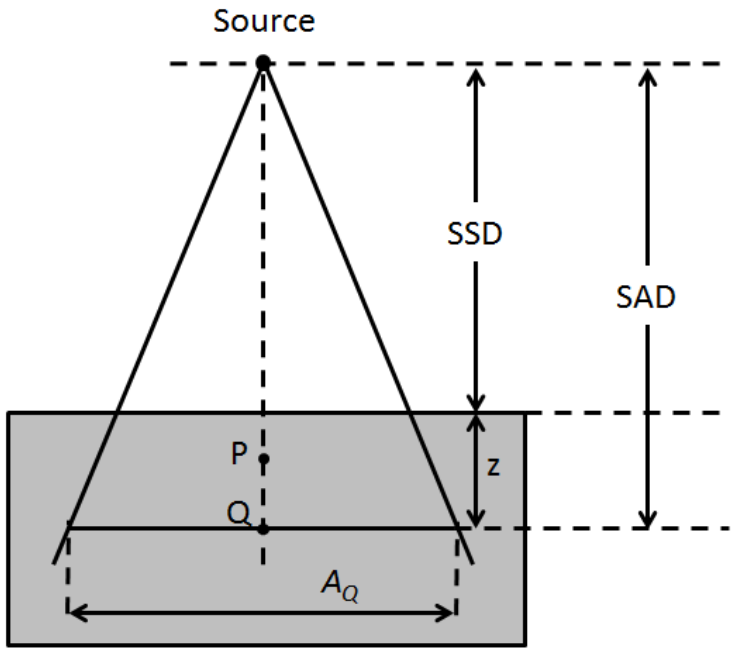

Figure 4.1. Geometry for measurement of PDD (picture taken from [10]) curves. SSD (Source-to-Surface Distance) indicates the distance between the radiation source and the surface of the phantom, SAD (Source-to-Axis Distance) is the distance between the source and the axis of the accelerator. The grey area represents the phantom where the PDD is measured.

Detector array v2 was used to measure TPR curves for 6 MV and 15 MV photon beams. Considering the notation of Figure 4.1, the following parameters were considered:

- Source Detector Distance SDD=SAD=100 cm (detector placed at isocenter). The parallel-plate-like geometry of the detector clearly defines the effective point of measurement, which corresponds to the inner surface of the front electrode;
- A_Q=10x10 cm^2;
- the depth of measurement z was changed by adding RW3 layers on top of the detector.

The data collected with the linear array (central pixel reading) were compared with those obtained using a CC04 ion chamber. Measured curves are show in Figure 4.2.

A noticeable agreement was found between the array and the thimble chamber for both 6 MV and 15 MV beam qualities. As outlined in Figure 4.2–bottom, the maximum deviation from reference after D_{max} is approximately 0.6%, which is comparable with the experimental uncertainty.

Accurate dose measurement in the buildup region is problematic because of the nature of radiation (in this region, the condition of charge particle equilibrium is not fulfilled, cf. Section 2.1). However, the agreement between detectors remains completely satisfactory.

These results can be interpreted as the proof of low detector dependence on low-energy scattered radiation.

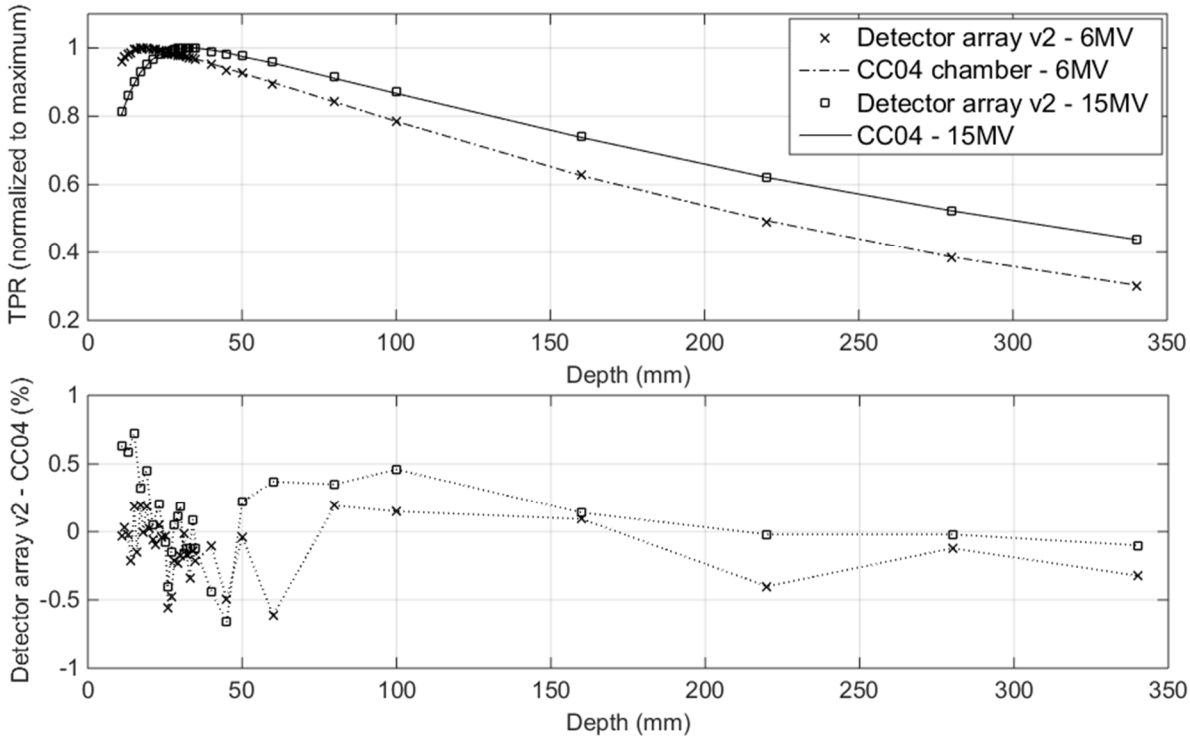

Figure 4.2. TPR curves (top) and percentage difference at different z between *detector array v2* and CC04 ion chamber (bottom). TPR distributions were measured for the Agility LINAC and are normalized to D_{max}.

4.1.2 Output factors

Similar to measurements of PDD curves, the measurement of the output factor (OF) of a LINAC is part of the commissioning workflow. However, it can also be repeated periodically. For a given photon beam at a given SSD, the dose rate at point P in a phantom depends on the field size A; as the field size increases, so does the measured dose at the center of the field, due to the increasing contribution of scattered radiation. The OF are

defined as the ratio of $M_P(z_P, A)$, the signal proportional to dose measured at P in a phantom for field A, to $M_P(z_P, A_{ref})$, the signal at P in a phantom for a field with size A_{ref}:

$$\mathrm{OF}(z_P, A_P, f, hv) = \frac{M_P(z_P, A, f, hv)}{M_P(z_P, A_{ref}, f, hv)} \tag{4.5}$$

A typical value for A_{ref} is 10x10 cm^2, but different reference field sizes can be selected. For instance, smaller fields (e.g. 5x5 cm^2, 3x3 cm^2) are often used for normalization when measured fields are as small as 1x1 cm^2. The geometry for the measurement of machine output factors is shown in Figure 4.3.

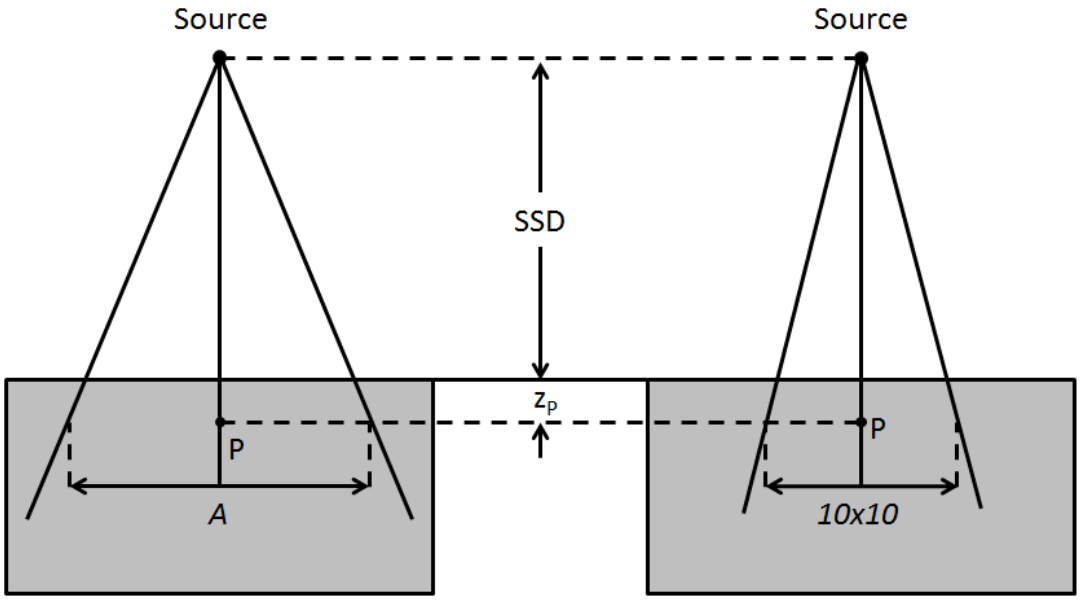

Figure 4.3. Geometry for the measurement of machine OF (picture adapted from [10]). The dose at point P is measured with field A (left) and with a 10x10 cm^2 field (right) which is taken as reference for normalization.

OF measurements were carried out with *detector array v2* for both 6 MV and 15 MV photon beams, with 10 cm RW3 buildup and SSD=90 cm. The signal from the central pixel of the array was considered.

Two different detectors were chosen as reference: a CC04 ion chamber and a p-type Razor diode (IBA Dosimetry GmbH, Schwarzenbruck, Germany) that features an active diameter of 0.6 mm and an active thickness of 0.02 mm. *Detector array v2* was benchmarked with the CC04 for fields equal to or larger than 3x3 cm^2. Below this field size, the dimension of the

chamber is not negligible compared to beam aperture and volume effect thus has a significant impact on measured dose. For the smallest field sizes (down to 1x1 cm^2), the signal from the Razor diode was taken as reference.

In common practice, because of their limited size, pinpoint detectors in a water tank are preferred to arrays for evaluation of machine output factors. However, an array that is suitable to multiple checks in machine QA could represent a very valuable tool. Additionally, a correct OF assessment is a way to evaluate the correct behavior of single chambers in the prototype.

Output factors measured with *detector array v2*, the thimble chamber, and the stereotactic diode are shown in Figure 4.4 and Table 4.1.

For field sizes in the range 2x2 cm^2–15x15 cm^2, the OF obtained with *detector array v2* are in agreement with the thimble chamber within 2%. For larger field sizes (20x20cm^2 and 25x25 cm^2), differences ranging from 2.5% to 4.0% were found. In the case of fields smaller than 5x5 cm^2, the array is closer to the stereotactic diode than the thimble chamber. In particular, for a 1x1 cm^2 field size, the array underestimates the diode measurement by 5.7% (6 MV) and 3.1% (15 MV).

Table 4.1. Output factors measured with the *detector array v2* and differences with respect to those measured with the compact chamber (IC) and the stereotactic diode. The signal is normalized at 5x5 cm^2 field size for all the detectors.

	Output factors (normalized)					
Lateral field size	6 MV			15 MV		
(cm)	*Array v2*	*Array v2-IC*	*Array v2-Diode*	*Array v2*	*Array v2-IC*	*Array v2-Diode*
25	1.153	-0.040		1.107	-0.040	
20	1.152	-0.025		1.110	-0.026	
15	1.131	-0.015		1.103	-0.010	
10	1.087	-0.006	-0.045	1.072	-0.003	-0.027
5	1.000			1.000		
3	0.928	0.003	0.010	0.930	0.010	0.012
2	0.888	0.023	0.019	0.854	0.016	0.005
1	0.672	0.090	-0.057	0.650	0.058	-0.031

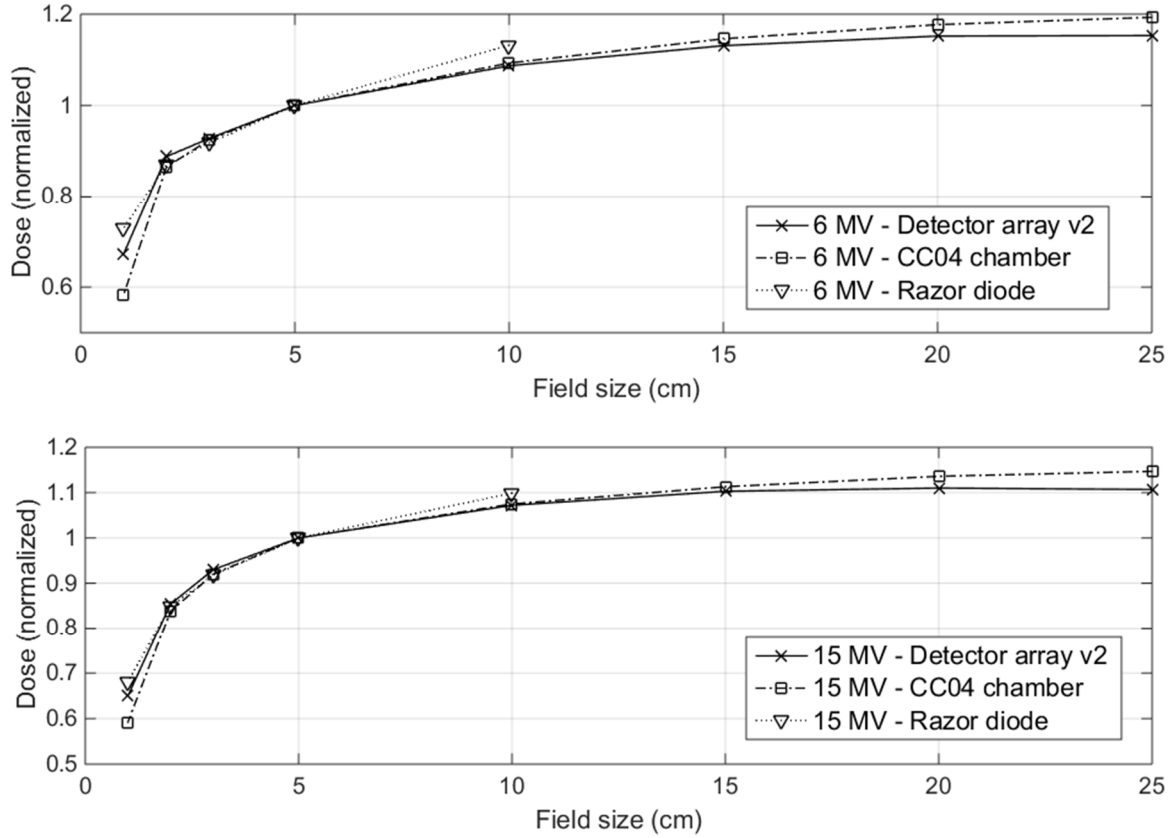

Figure 4.4. Agility LINAC output factors for 6 MV (top) and 15 MV beam quality (bottom). Measurements with the diode (Razor) were taken up to 10x10 cm^2 field size. The signal is normalized at 5x5 cm^2 field size for all the detectors.

4.1.3 Beam profiling

Dose distributions along the beam central axis (PDD) provide only a segment of the information required for machine QA. Dose distributions in 2D and 3D are determined with central axis data in conjunction with off-axis data.

Fundamentally, the off-axis data are obtained by measuring beam profiles perpendicularly to the beam central axis at a given depth in a phantom. The depth of measurement is typically z_{max} or z=10 cm for verification of compliance with machine specifications; other depths can be required by the treatment planning system. Beam profiles are usually defined as the ratio of dose at an off-axis point to the dose on the central beam axis at the same depth in a phantom.

MV X-rays beam profiles consist of three distinct regions: central, penumbra, and tail. The central region represents the central portion of the profile extending from the beam central axis to within 1–1.5 cm from the geometric field edges of the beam. The geometric field size is usually defined as the separation between the 50% dose level points of the beam profile.

In the penumbra region, the dose changes rapidly and depends on the field defining collimators, the finite size of the source and the lateral electronic disequilibrium. The dose fall-off around the beam edge is sigmoid in shape and extends into the penumbra tail region, where there is a small component of dose due to transmission through the collimator and phantom-scattered radiation. The tail is the region outside the radiation field, where the dose should ideally be close to zero in order to minimize the dose delivered to tissues outside the target volume.

Measuring beam profiles along the two major beam axes with a 2D detector may represent a straightforward and time-saving procedure in comparison to the use of a water phantom scanner.

Relative dose profiles of flattened and unflattened beams were measured with *detector array v2* at the depth of maximum dose (z_{max}). Two reference detectors were used: the commercial 2D ion-chamber array MatriXX^{Evolution} (IBA Dosimetry GmbH, Schwarzenbruck, Germany), with 7.6 mm pixel pitch and 4.5 mm chamber diameter, and an amorphous silicon flat panel (0.2 mm pixel pitch) operating in direct conversion mode. Uniformity correction was determined by taking the ratio of a 30x30 cm^2 field, measured with the linear array and with a CC04 chamber in a water tank. For the MatriXX^{Evolution}, the penumbra region was interpolated with a Fermi-Dirac distribution function down to 5x5 cm^2 and with a linear fit for 3x3 cm^2 and 2x2 cm^2 field sizes. For *detector array v2* and the silicon flat panel, an Erf-type function was chosen for data interpolation in the penumbra region, with the exception of the 1x1 cm^2 field, where a linear fit was applied to array data. Flatness is evaluated according to AAPM Task Group 45 code of practice [81].

Dose profiles were measured for different field sizes for both flattened and unflattened beams. In Figure 4.5, a subset of normalized profiles is shown for 6 MV (top) and 10 MVFFF X-rays beams (bottom). Field and penumbra widths measured with the *detector array v2*, as well as the deviation from MatriXX and flat panel data, are reported in Table 4.2 for 6 MV

and 15 MV energies. The field width agreement between array prototype and MatriXX (flat panel) is within 0.9 mm (0.6 mm). Both chamber arrays overestimate the penumbra width measured by the flat panel, probably because of the volume averaging effect. However, *detector array v2* provides a closer agreement with the flat panel, as the maximum deviation between penumbra widths measured by these two detectors is 1.4 mm. Flatness and symmetry (Table 4.3) measured with *detector array v2* and the reference detectors are comparable, and differences are always smaller than 1%.

Table 4.2. Measured values of field width and left penumbra width for 6 MV (top) and 15 MV (bottom) beam qualities. Similar results are obtained for the right penumbra. Deviations with respect to values measured with the MatriXX array and the flat panel are also reported.

	Detector array v2		*a:Si flat panel*		*MatriXX*	
Field size (mm)	Width (mm)	Penumbra (mm)	Width (mm)	Penumbra (mm)	Width (mm)	Penumbra (mm)
10	10.1	3.2	9.5	2.4	-	-
20	19.4	3.6	19.8	2.7	18.5	9.1
30	29.7	4.0	29.8	2.9	30.2	5.7
50	50.4	4.5	50.3	3.1	50.2	5.4
100	100.2	4.1	100.2	3.3	100.6	6.3
150	150.3	3.8	149.9	3.4	150.9	5.6
200	200.7	3.8	-	-	201.1	5.5

	Detector array v2		*a:Si flat panel*		*MatriXX*	
Field size (mm)	Width (mm)	Penumbra (mm)	Width (mm)	Penumbra (mm)	Width (mm)	Penumbra (mm)
10	10.6	3.5	10.2	3.0	-	-
20	19.6	4.4	19.9	3.7	19.2	9.5
30	29.9	4.8	30.1	3.9	30.5	6.3
50	50.3	5.6	50.2	4.6	50.2	7.2
100	100.4	5.4	100.1	4.9	100.9	7.7
150	150.6	5.0	150.5	5.2	151.3	6.8
200	200.8	4.8	-	-	200.8	7.2

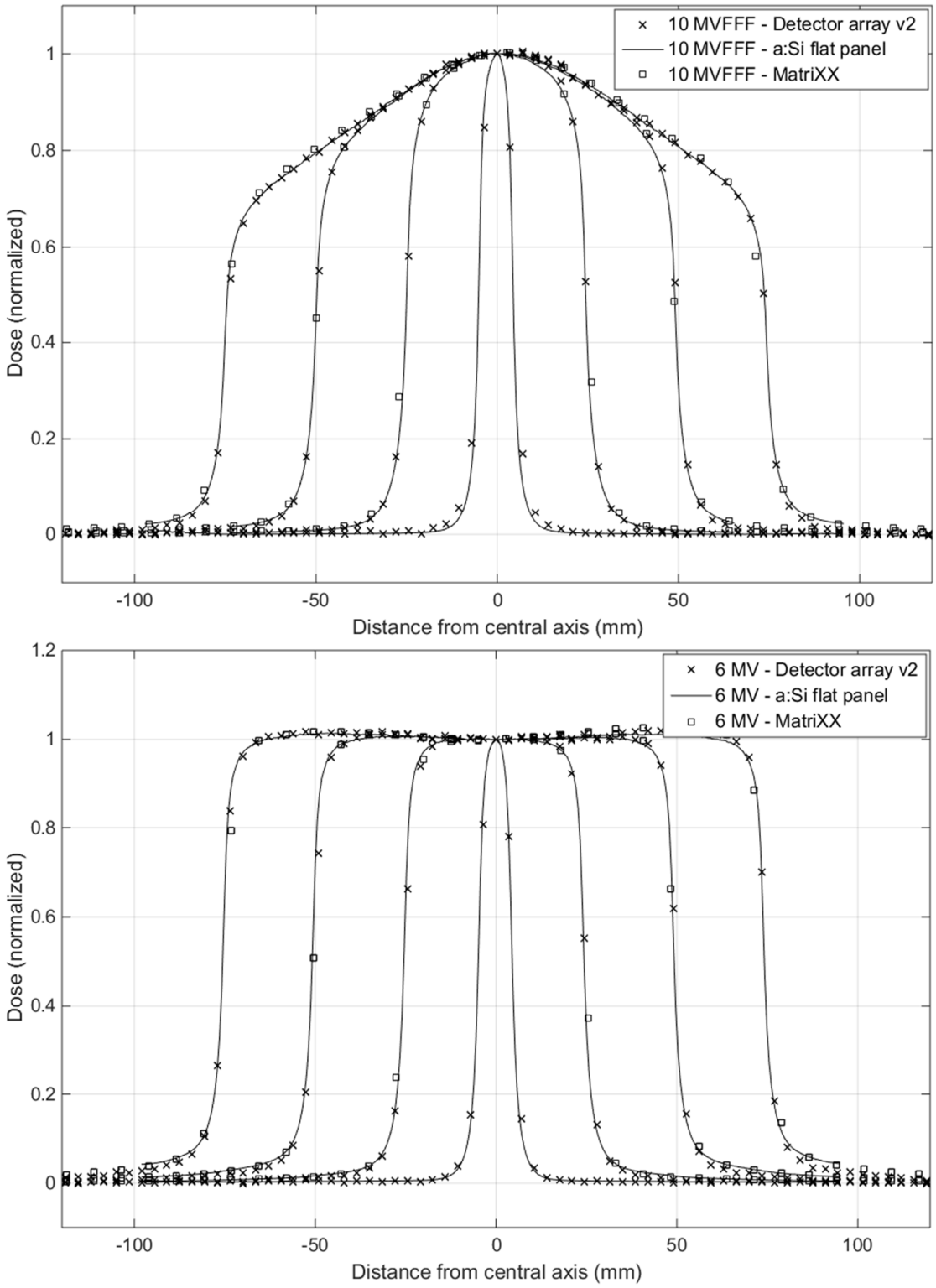

Figure 4.5. Comparison of beam profiles for 6 MV (top) and 10 MVFFF beam quality (bottom), for TrueBeam LINAC. Profiles (1x1 cm^2, 5x5 cm^2, 10x10 cm^2, 15x15 cm^2) are normalized on the beam central axis. Due to the 7.6 mm pitch, MatriXX detector is not suitable to measure the 1x1 cm^2 field.

Table 4.3. Typical values of flatness and symmetry of profiles measured with the *detector array v2*, the MatriXX array used as a reference and the flat panel prototype.

Lateral field size	Flatness (%)			Symmetry (%)		
(cm)	*array v2*	*MatriXX*	*Flat panel*	*array v2*	*MatriXX*	*Flat panel*
15	1.15	1.36	0.73	1.0	1.0	0.5
10	0.67	0.71	0.73	1.2	0.3	0.6
5	0.34	0.34	0.36	0.5	0.6	0.7

Figure 4.6 shows the comparison of *detector array v2* with Gafchromic® EBT3 film for a 1x1 cm^2 field delivered with the TrueBeam™ LINAC at 10 cm water-equivalent depth. The same profile has also been measured with the flat panel. Differences between the array and the film have the same magnitude as those between the flat panel and the film. In particular, the maximum measured difference is 3% in the penumbra region.

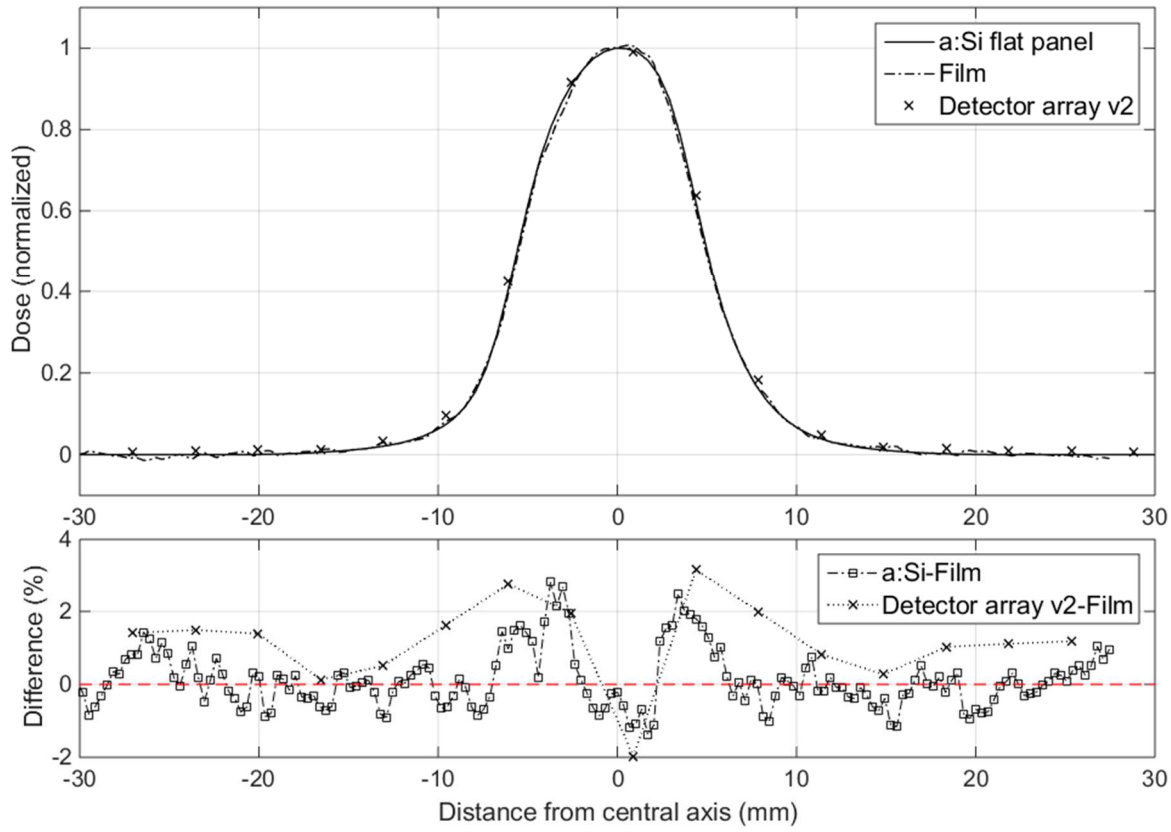

Figure 4.6. 1x1 cm^2 field (Varian TrueBeam, 10 MV beam quality) measured with *detector array v2,* a:Si flat panel and EBT3 film (top). Differences between the array and the film have the same magnitude of those between the flat panel and the film (bottom).

4.1.4 Discussion

The relative dosimetry capability of *detector array v2* makes it a valuable tool for LINAC quality assurance. Measurements of depth dose distributions show a maximum deviation from the reference ion chamber of about 0.6% beyond z_{max} (up to 34 cm depth) for both 6 MV and 15 MV. As already observed, this result quantifies the low dependence of the sensitivity of the detector on photon energy.

For field sizes in the range 2x2 cm^2–15x15 $cm^{2,}$ the OFs obtained with *detector array v2* are in agreement with the thimble chamber within 2%, whilst a 4.0% deviation was found at 25x25 cm^2 field size. An underestimation of output factors at large field sizes has already been reported in literature [69] in the case of liquid-filled ion chamber arrays (2.6% with 6 MV and 1.8% with 15 MV, with a field size of 27x27 cm^2). The authors suggested the energy dependence introduced by the high-Z electrodes of the detector as a possible explanation. This is not the case for the prototype under study, which does not present high-Z materials in the chamber volume (cf. confidential appendix). The behavior of *detector array v2* at large field sizes could instead be due to the fact that the amount of lateral scattering of radiation in a volume with many air cavities at short distance is smaller than in a homogeneous volume without cavities. This is consistent with the fact that the fraction of lost signal increases with increasing field size.

A more detailed investigation with Monte Carlo simulations of the phenomenon has been started. Although it is possible to employ correction factors to compensate field size dependence [82, 83], this effect shall firstly be minimized by optimizing detector design.

The simulation package that has been chosen for the Monte Carlo investigation is EGSnrc, which provides tools to run simulations of coupled electron-photon transport for particle energies ranging from 1 keV to 10 GeV. It also includes a C++ geometry library for defining geometry of complex simulation environments and particle sources.

The ‘chamber’ C++ library has been used to implement a simplified geometry which simulates the *detector array v2* geometry. It basically consists of a row of 80 air cavities with a similar design to those of the array prototype, included into a cube of water of 30x30 cm^2. A 6 MV photons spectrum can be applied to the defined geometry, with different beam

apertures in order to study the effect of the field dimension on the chamber response. Particle transport parameters and enhancement regions can also be tuned in order to increase the efficiency of the simulation.

The simulation code has already been built but it needs to be further improved and refined in order to give reliable results. However, this preliminary implementation can be used as basis for a future complete investigation of the detector dependence to field size through Monte Carlo simulations.

Profiles of beams with different beam qualities and field sizes (in the range from 1x1 cm^2 to 20x20 cm^2) were measured and compared with an amorphous silicon flat panel and a MatriXX array. The measurement of a 1x1 cm^2 field was also benchmarked to film measurement. The largest deviations in the measurement of penumbra and field width between *detector array v2* and the flat panel are 1.4 mm and 0.6 mm, respectively. In the case of the 1x1 cm^2 field, the maximum deviations between the *detector array v2* profile and film are within 3%. In the profiling of small fields, *detector array v2* performs a less pronounced overestimation of penumbra regions compared to the reference MatriXX, which, due to larger chamber pitch (7.6 mm) and active volume (4.5 mm diameter), is not suitable for measuring fields smaller than 2x2 cm^2. The ability to measure dose distributions of small photon fields is essential, as they are increasingly used in modern radiotherapy treatments, such as IMRT and SRS. A broadening of the measured penumbra due to volume averaging may result in over-irradiation of organs that are adjacent to the tumor volume and so at risk [66].

As part of this work, it is possible to conclude that the detector based on the investigated technology addresses the needs of LINAC machine QA, with clear improvements in spatial resolution with respect to commercial ion chamber-based detectors and comparable performances to single ionization chambers for TPR and LINAC OF measurements. The technology is suitable for building manageable detectors that can be used for fast and reliable routine QA checks in clinics. From the results presented, it is also clear that one question that remains open is the dependence on field size, which will be further addressed in a future work.

4.2 PATIENT QUALITY ASSURANCE

High accuracy in dose delivery in cancer treatments is becoming increasingly necessary with the advent of complex treatment delivery options that makes patient management critical. High modulation, very short delivery times, and elevated dose rates are the most common features of VMAT and SBRT/SRS delivery techniques. Therefore, as already stated in previous Section 1.2.2, patient plan verification is a fundamental step in the quality assurance process designed to ensure correct radiation delivery.

Several patient plans were verified through *detector array v2* being irradiated with the Trilogy® LINAC at the Klinikum rechts der Isar. The computed dose from treatment planning system was compared with experimental measurements from the linear array and, for two selected cases, with other reference detectors.

4.2.1 Patient plan verification through comparison of linear dose distributions

As already discussed in Section 1.2, in patient QA, it is common practice to deliver IMRT, VMAT, and stereotactic treatment plans to a phantom and to compare the doses measured in the phantom with those calculated by the planning system for that phantom. The comparison is typically performed on a 2D dose grid through the gamma index analysis.

Preliminary tests of patient plan verification were performed with various IMRT, SRS, and VMAT plans, and agreement with TPS dose distributions was evaluated along the inline major axis. Dose analysis of 2D distributions is not feasible with *detector array v2*, being this a linear detector.

As a first step, a computed tomography (CT) of the detector was acquired and imported into the treatment planning system Eclipse (Varian Medical Systems, Palo Alto, CA, US) in order to calculate the expected dose distribution in the linear array (using an anisotropic analytical dose calculation algorithm), as shown in Figure 4.7. Secondly, *detector array v2* was irradiated (Figure 4.8) with complete plans for different clinical localizations, and the dose was recorded.

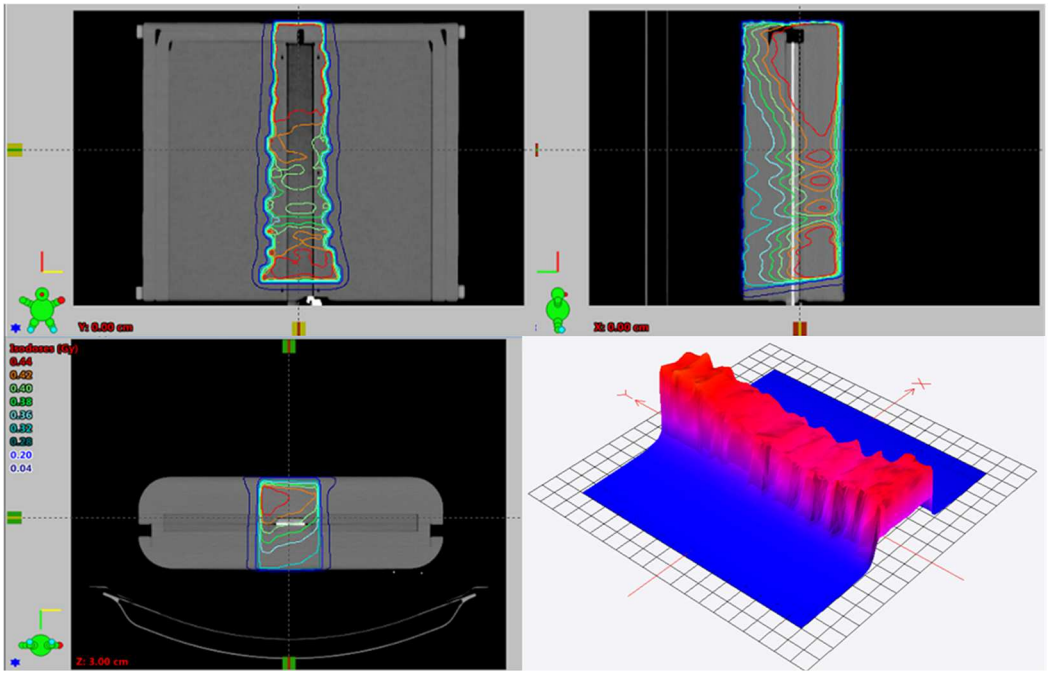

Figure 4.7. CT images of *detector array v2* inserted into the phantom, imported into Eclipse TPS. Fields from a sliding window IMRT plan for treatment of a spinal tumor are applied to the phantom CT images in order to compute dose distributions in the array. Comparison between measured and computed distribution is represented in Figure 4.10–bottom inset.

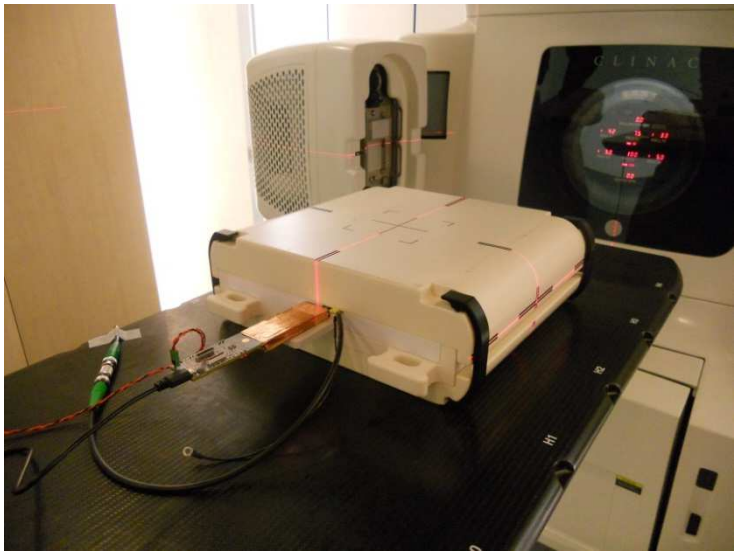

Figure 4.8. *Detector array v2* inserted into the phantom and ready to be irradiated with the Trilogy® LINAC (Klinikum rechts der Isar) for patient plan verification.

For two selected cases (an SRS irradiation of a brain tumor and a VMAT irradiation of a lung tumor), linear array data were also compared with measurements taken with the 2D diode array MapCHECK 2 (Sun Nuclear Corporation, Melbourne, FL, US) featuring a uniform detector spacing of 7.0 mm (enhanced to 5.0 mm with software interpolation), as well as with Gafchromic EBT3 films (Ashland Specialty Ingredients, Bridgewater, NJ, US) (Figure 4.9). EBT3 films were read with a fluorescent lamp scanner (EPSON Perfection V700) by means of dedicated software (EPSON Scan. Vers. 3.9.2.0 US). Data analysis was performed on the red color channel using the software MapCHECK (Vers. 5.02.00.02, Sun Nuclear Corporation, Melbourne, FL, US). The dose calibration curve was calculated for different energies from previously irradiated films at different dose exposures. To fit the calibration curves, the function

$$d_X(D) = a + b/(D - c) \tag{4.6}$$

was used, where $d_X(D)$ is the optical density of the film in scanner channel X at dose D, and where a, b, and c are the parameters to be fitted. Results of patient QA investigation are plotted in Figure 4.10, Figure 4.11, and Figure 4.12.

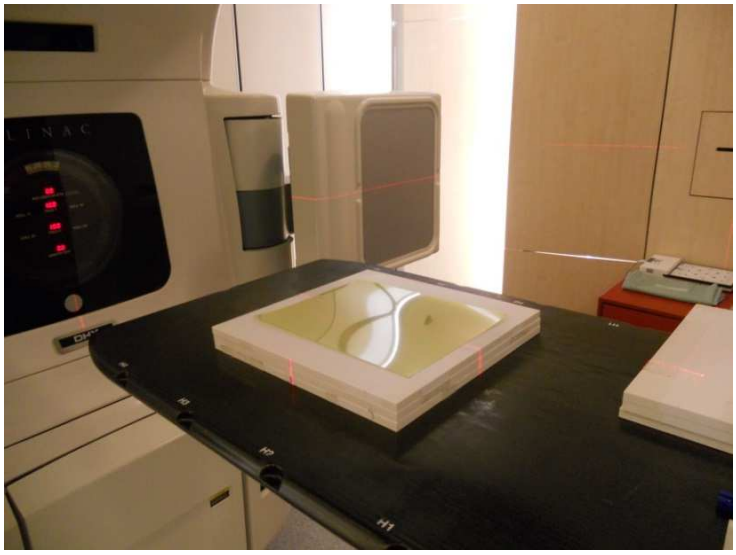

Figure 4.9. Patient QA measurement with EBT3 film. The backscatter and the buildup were adjusted to match the *detector array v2* measurement conditions.

As shown in Figure 4.10, the detector is able to accurately reproduce the expected dose distributions. The average difference between the *detector array v2* and the TPS was found to be below 1.1%, with maximum deviations always being lower than 3.0% in the target region

(i.e. for values of dose greater than 80% of the maximum). The main features of the lung tumor VMAT irradiation with high dose modulation (Figure 4.11), of the SRS irradiation of a brain tumor (Figure 4.12) and comparative results are summarized in Table 4.4. In both cases, the average difference between *detector array v2* and films is below 1.2%. Measurements taken with the linear array and MapCHECK 2 diode array are consistent. A slightly better agreement with film is achieved with the linear array when the fluence is highly modulated: a 0.6%–0.7% average improvement was observed in the VMAT delivered plan, with a maximum deviation from film of 4.2% and 9.2% for *detector array v2* and MapCHECK 2, respectively. Similar profiling performance in stereotactic beams was measured with the *detector array v2* and the diode array.

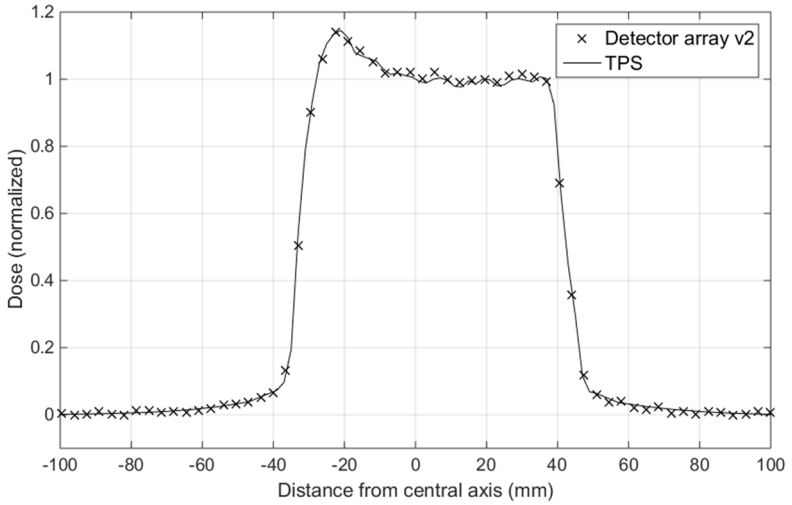

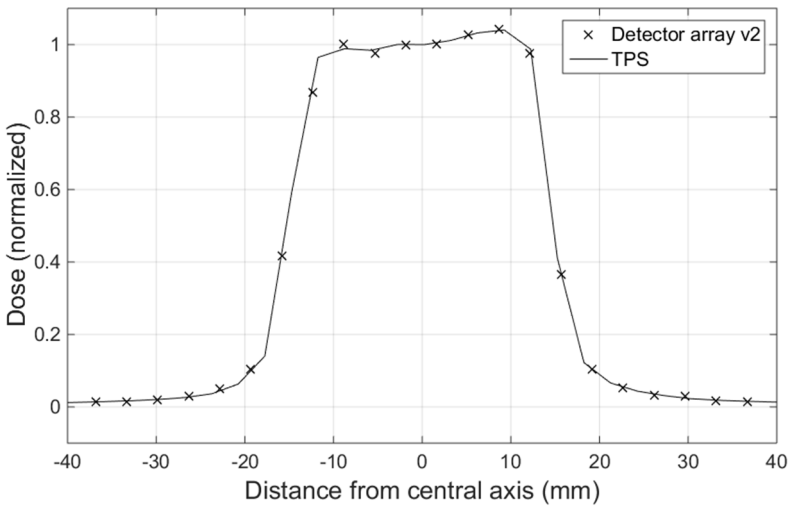

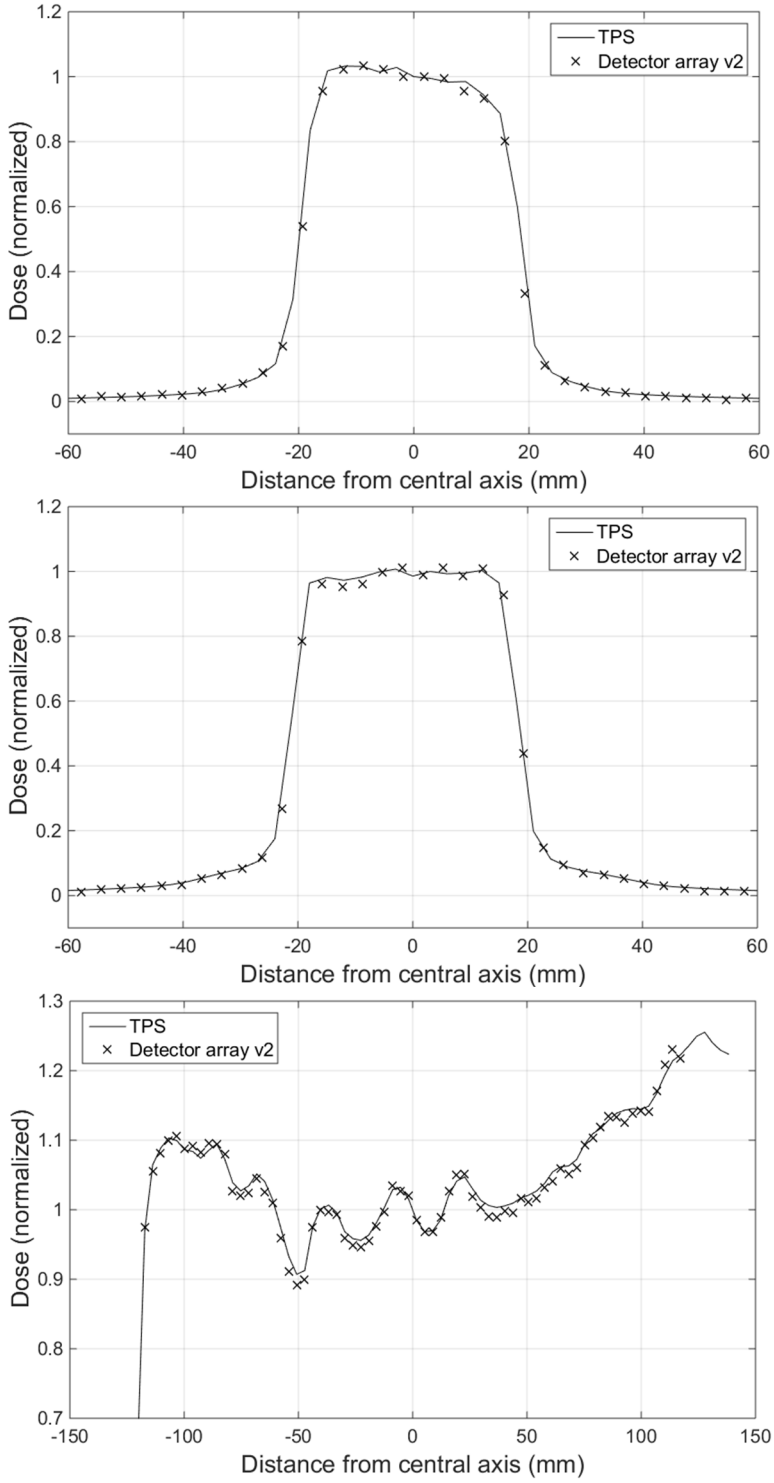

Figure 4.10. Comparison of dose distributions measured with *detector array v2* and calculated with Eclipse TPS for: prostate step and shoot IMRT irradiation (first from the top), skull lesion VMAT irradiation (second from the top), spine VMAT irradiation (third and fourth from the top), spine sliding window IMRT irradiation (first from the bottom). Dose is normalized to the central axis of the detector. All the treatments feature 6 MV beam quality, with the exception of the spine irradiation shown in the middle-right panel (6 MVFFF).

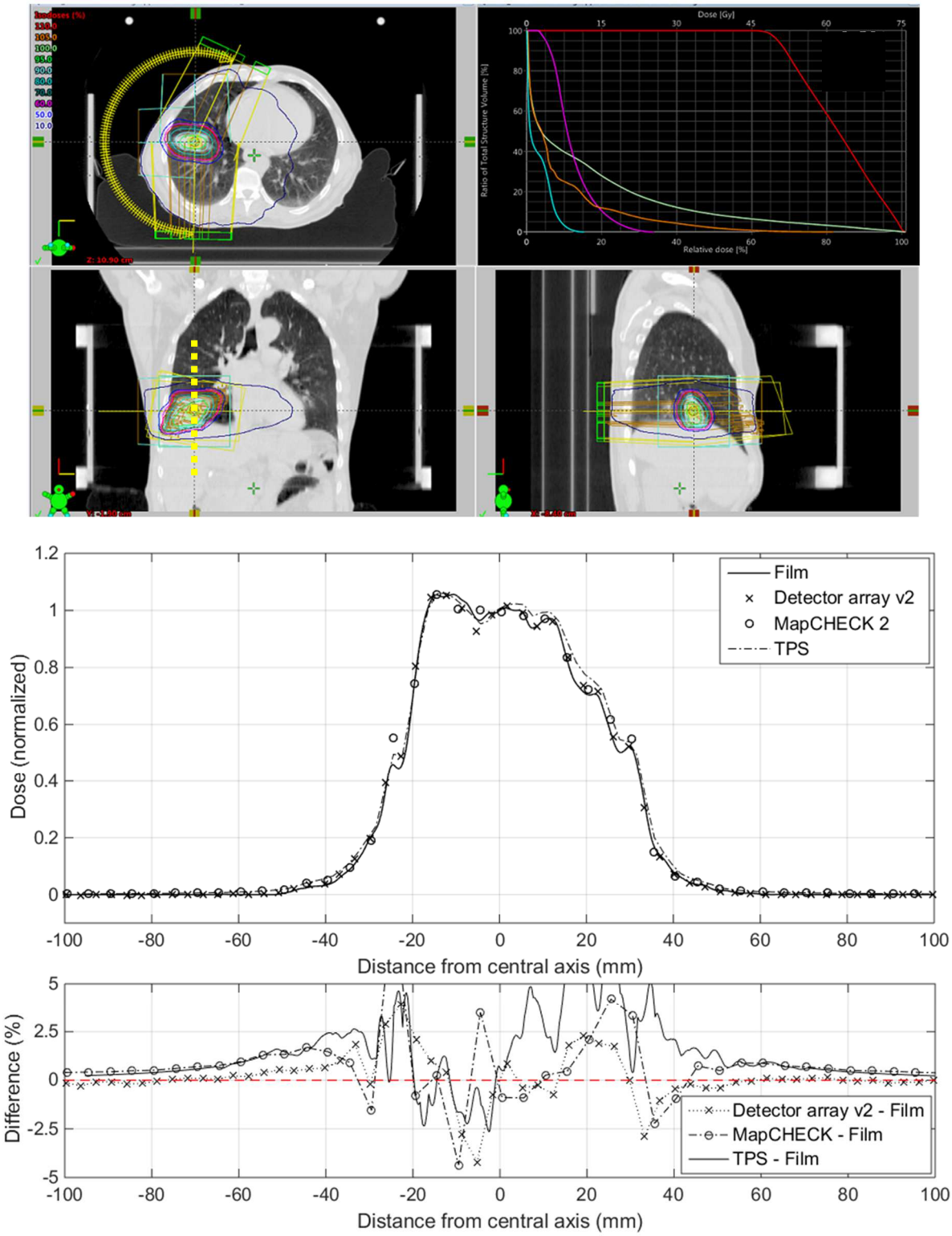

Figure 4.11. VMAT lung plan with 15 MV beam: isodose curves and dose-volume histogram from TPS (top); dose distributions and differences between investigated detectors (bottom). The dose distribution was measured with *detector array v2* along the dashed yellow line.

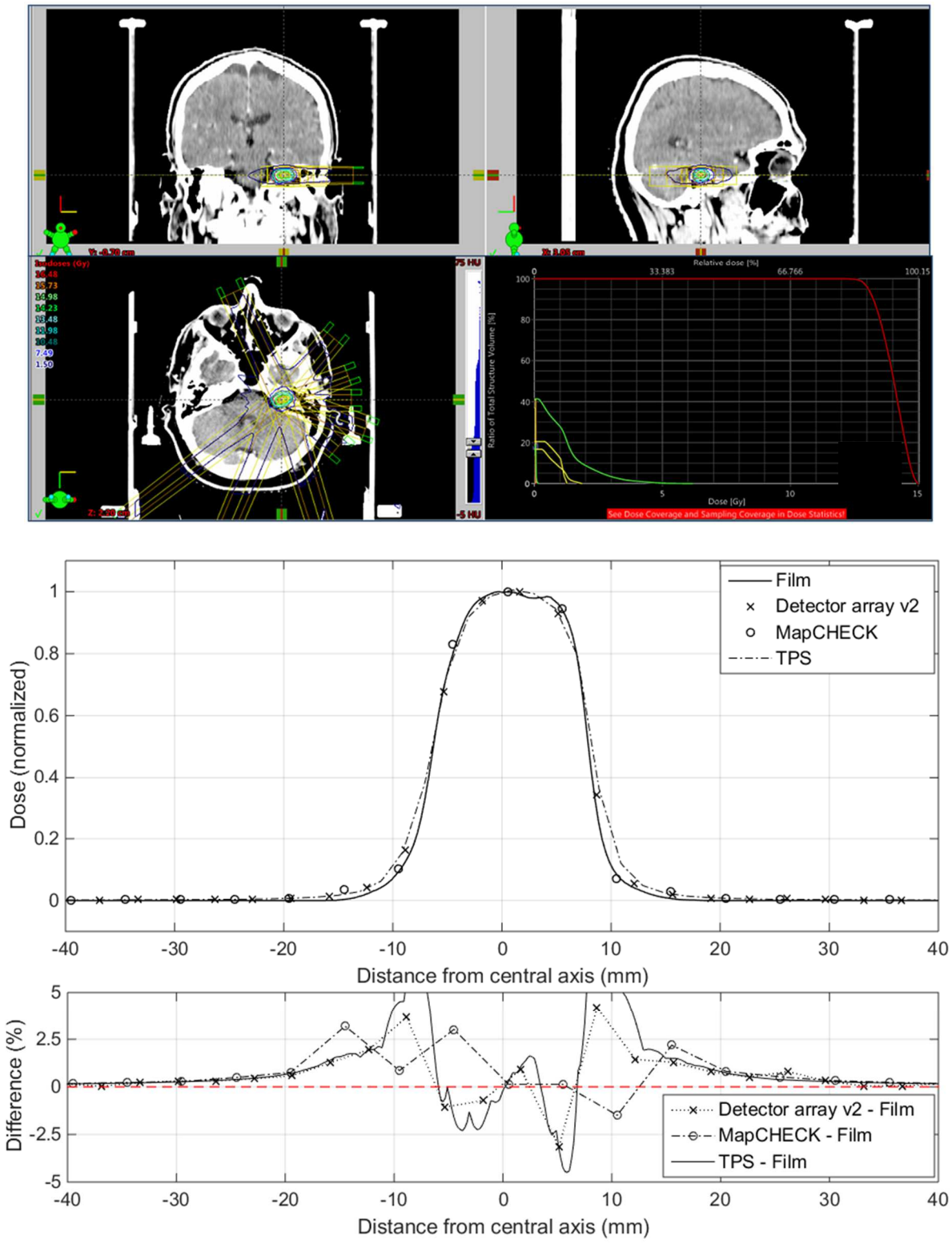

Figure 4.12. SRS head tumor plan with a fixed dose rate of 1000 MU/min and 9 radiation segments: isodose curves and dose-volume histogram from TPS (top); dose distributions and differences between detectors (bottom).

Table 4.4. Characteristics of the plans delivered and average difference between detectors, treatment planning system and EBT3 films (MapCHECK 2 is indicated as MapC. for table clarity). Films were chosen as reference due to the non-uniformity of measured dose distributions and small field sizes.

Clinical Localization	Technique	Energy (MV)	*Array v2*-TPS (%)	*Array v2*-film (%)	MapC.-TPS (%)	MapC.-film (%)
Lung	VMAT	15	2.01	1.13	2.08	1.78
Brain	SRS	6	0.77	1.19	1.49	1.10

4.2.2 Discussion

Profiles of dose distributions delivered with a variety of IMRT, VMAT, and SRS patient plans were measured with *detector array v2*.

The choice of plans and delivery techniques reflects the main features and boundaries the author sought to test and benchmark the array prototype. Based on the presented results, it is possible to conclude that the detector is generally capable of accurately verifying the dose distribution calculated by the TPS. In addition, profiles are accurately measured even when the target region is narrow and exhibits a highly heterogeneous dose coverage, or when radiation is delivered with a high dose rate and modulated fluence. This is, in many cases, the boundary for such technologies.

In the case of VMAT and SRS plans, an average (maximum) deviation of the order of 1% (4%) from films has been measured. Films were chosen as a benchmark due to their accuracy in measuring modulated dose distribution and steep dose gradients. Therefore, for radiosurgery and IMRT QA, they are generally considered to be the absolute reference. For the tests presented in Paragraph 4.2.1, uncertainties in film measurements were not evaluated. However, it is possible to find exhaustive works in literature about the estimation of uncertainties in film dosimetry. For instance, a detailed uncertainty budget has been determined in [84], resulting in a total uncertainty (inclusive of uncertainties on scanning procedure and calibration fit) within 1.5% for photons (6 MV and 18 MV) and less than 1% above ~1.5 Gy. Similar results are presented in [45], where an overall uncertainty in the order of 1.3% (1 SD) was found for film measurements. Uncertainty levels of 0.9% on absolute

dose measurements and of 0.45% on relative dose measurements were achieved in [44]. A performance comparison between EBT3 films and a 2D array based on ionization chambers for patient plan verification (VMAT SBRT lung treatment) can be found in [85].

After a comprehensive dosimetric characterization, the fact that the technology under investigation is suitable to be used in patient plan verification has been proven. In order to judge the accuracy of the performed measurements, the *detector array v2* performances have been benchmarked to reference detectors and protocols. The technology appears to be very promising for conventional, SRS/SBRT, and VMAT radiotherapy. Although it is clear that a 1D linear array is not sufficient for complete patient plan verification, this study indicates that a 2D device based on the same technology would probably be suitable for such verifications.

These statements have been confirmed and extended by the clinical partners, who participated in the clinical assessment of the technology and expect the integration of the device in a dedicated software platform and the implementation of a 2D sensor. Moreover, the results shown in this chapter have been presented at international conferences and are part of a recent publication [86].

Chapter 5 DETECTOR ARRAY V2 CLINICAL CHARACTERIZATION WITH PROTONS

In recent years, radiotherapy with charged particles (especially protons) has become increasingly important. This is a consequence of the fact that it exhibits clear benefits with respect to conventional photon radiotherapy in the treatment of some clinical localizations, and that the cost of the treatment facilities is decreasing with time. On the other hand, QA dosimetry in particle (proton) therapy can be even more challenging, especially for PBS treatment modality, where a number of parameters have to be checked and the radiation is delivered in a different way than with conventional radiotherapy (cf. Section 1.1.2.3).

For these reasons, to complete the present study, it was clear that the new ion chamber technology had to be tested in clinical proton beams in order to assess its suitability to dosimetric application in proton therapy.

This chapter summarizes the experimental campaign performed with *detector array v2* at the Proton Therapy Center Czech s.r.o. (Prague, Czech Republic) equipped with an IBA Proteus® Plus cyclotron. The machine delivers ~6 nA quasi-continuous proton current at the nozzle with a maximum proton energy of 226 MeV (corresponding to ~32 cm range in water). Measurements were carried out in a 360° gantry room equipped with a PBS-dedicated nozzle (the FWHM of the Gaussian which defines the shape of the beam is ~8.7 mm at 150 MeV in air at isocenter).

The chapter consists of three main sections. In Section 5.1, basic dosimetric properties such as charge collection efficiency and linearity with MU are investigated.

Section 5.2 deals with two machine quality assurance procedures: measurement of uniform dose distributions and measurement of pristine Bragg peak at different energies.

Section 5.3 is a summary of preliminary patient plan measurements. Results are compared with calculated dose from TPS and a commercial ion chamber 2D array. Measurements taken with the 1D array are compared with linear distributions of dose extracted from TPS and 2D array data.

Conclusions concerning the characterization of *detector array v2* with proton beams are summarized in the last part of the chapter: Section 5.4.

5.1 DOSIMETRIC CHARACTERIZATION WITH PBS PROTON BEAMS

Proton-beam dosimetry is typically carried out using different detector systems: ionization chambers, calorimeters, radiochromic films, and semiconductor dosimeters. Calorimeters and films are the reference for absolute dose determination. However, because of the complexity of measurement procedures, their use is restricted to non-routine activities. Solid-state detectors are used for relative dose measurements because of their spatial resolution, high sensitivity, and relatively low cost, but the dependence of their response on the particle energy is difficult to model. Ionization chambers are well-suited for routine measurements, and they are also considered to be the reference detectors for intercomparisons and calibration of proton beams.

In the following section, the characterization of charge collection efficiency and linearity of *detector array v2* with delivered Monitor Units is reported.

5.1.1 Charge collection efficiency

Detector array v2 was placed on the treatment couch (Figure 5.1) and irradiated with a uniform dose distribution from a 0° gantry angle at a measurement depth of 3 cm, in order to determine the optimal bias and to evaluate the charge collection efficiency.

Charge collection efficiency was measured with the highest reachable proton current and, therefore, with the highest rate of ion recombination in the sensitive volume. Moreover, in a shallow depth (3 cm), the protonic charge density is higher because the pencil proton beam is not much broadened by the multiple Coulomb scattering. Beam parameters were 226 MeV proton energy and ~6 nA proton current impinging on the detector. Signal at 100% charge collection was estimated through a linear fit of signal versus $(1/\text{bias})^2$, according to IEC 60731 radiation dosimetry protocol [33].

The bias applied to the detector was changed in the range 20 V–400 V, and the signal from the central chamber of the array was recorded. The resulting charge collection efficiency curve is shown in Figure 5.2.

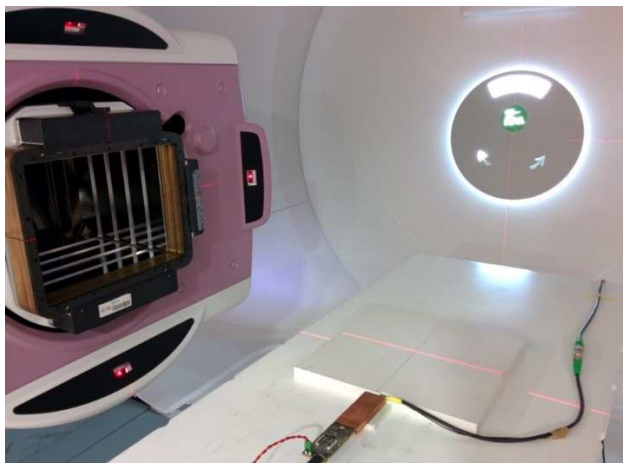

Figure 5.1. *Detector array v2* inserted in the dedicated holder and placed on the treatment couch. The nozzle was rotated to 0° position (in the figure, it is at 270°) to deliver the proton beam perpendicularly to the detector surface.

Charge collection efficiency is already higher than 99% at 100 V, reaching 99.7 %±0.3% at 250 V. Similar to measurements with MV X-rays, the operating voltage was set to 250 V for all the subsequent tests.

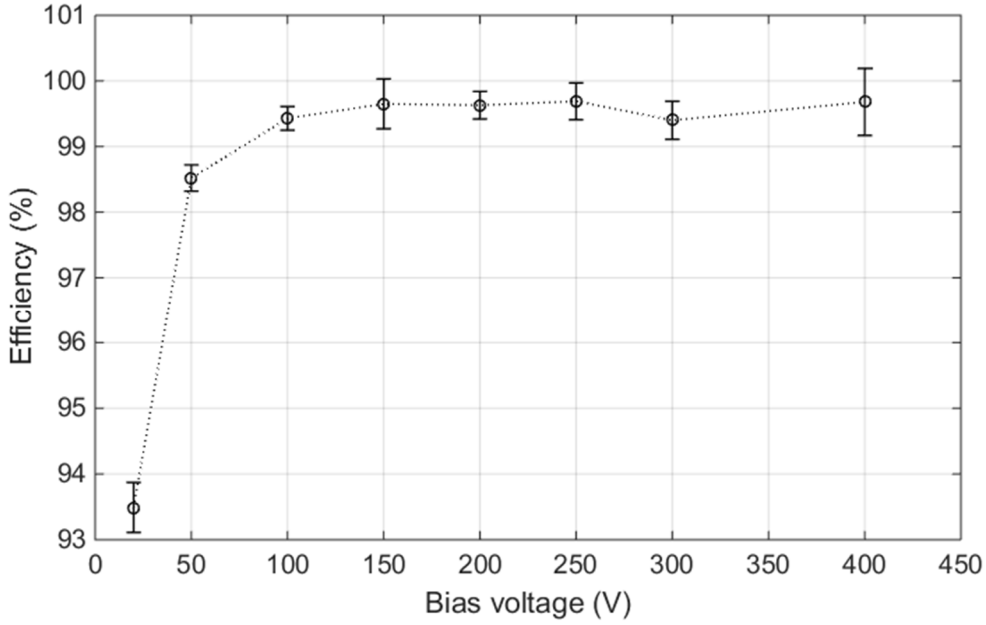

Figure 5.2. Measured efficiency curve of *detector array v2*.

It is worth mentioning that the initial or columnar recombination in proton beams has a larger effect than in photon beams because of the higher ion density generated within the single

particle track. Future studies will focus on the recombination rate of *detector array v2* with pulsed proton beams, such as those produced by a new generation of synchrocyclotrons (e.g. IBA Proteus® ONE) for proton therapy. In that case, proton pulses are delivered with a frequency of 1 kHz and charge up to about 5 pC/pulse in clinical conditions.

5.1.2 Linearity with MU

Dosimeters' linearity with dose (or MU) is typically evaluated at different beam energies in the clinical energy range (100 MeV–226 MeV in PBS modality for the IBA C230 cyclotron). In common practice, the linearity is evaluated at the lowest and the highest energies, as well as at one or two energies in between.

The *detector array v2* linearity with MU was assessed at three selected energies (100, 165, and 226 MeV), with the same measurement conditions as those reported in Paragraph 5.1.1. The number of monitor units delivered in each beam spot was changed in the range 0.02–12 MU/spot, which corresponds to an absolute dose range of 0.05–30 Gy with the present measurement conditions. The monitor chamber in the treatment nozzle was used as a reference for the measurement of the delivered integral dose. This chamber is a strip ionization chamber operating in transmission mode, which is linear with dose within ±1% at any dose rate (0.5–8 Gy/min), according to specifications [87]. Moreover, the linearity at low doses (0.02–2 MU/spot) of the monitor chamber was verified with a PPC05 ionization chamber (IBA Dosimetry GmbH, Schwarzenbruck, Germany), which features a parallel plate geometry with 0.6 mm inter-electrode distance. In addition, it is used in the clinic to routinely check the linearity of the system with dose delivered. Linearity between monitor chamber and PPC05 was found to be well within ±1% in the investigated range of MU/spot.

It should be noted that when the amount of dose delivered in a single spot is changed, the delivery system automatically adjusts the proton current up to a certain limit, and that the beam line efficiency (and therefore the proton current measured in the nozzle) is different at different energies. For instance, this delivery algorithm results in a proton current to the patient which ranges, in the case of 226 MeV protons (the energy with the highest beam line efficiency), from 0.05 nA to 6.2 nA. The value of 6.2 nA is the limit already reached at 2

MU/spot delivered; for a greater value of MU/spot, the current is fixed to this limit and the irradiation time is increased accordingly.

The linearity for *detector array v2* was evaluated in terms of residuals from linear regression; results for the investigated energies are reported in Figure 5.3, Figure 5.4, and Figure 5.5.

The detector response at 100, 165, and 226 MeV is linear within ±1.1%, with maximum deviations from linear regression that occur at the lower measurements limit (5 cGy delivered dose). It is therefore realistic to assume the detector to be linear over the entire range of clinical energies. This feature is of great importance, since, in PBS treatment modalities, the target volume is covered by radiation beams at different energies, layer after layer (an example is given in Section 5.3).

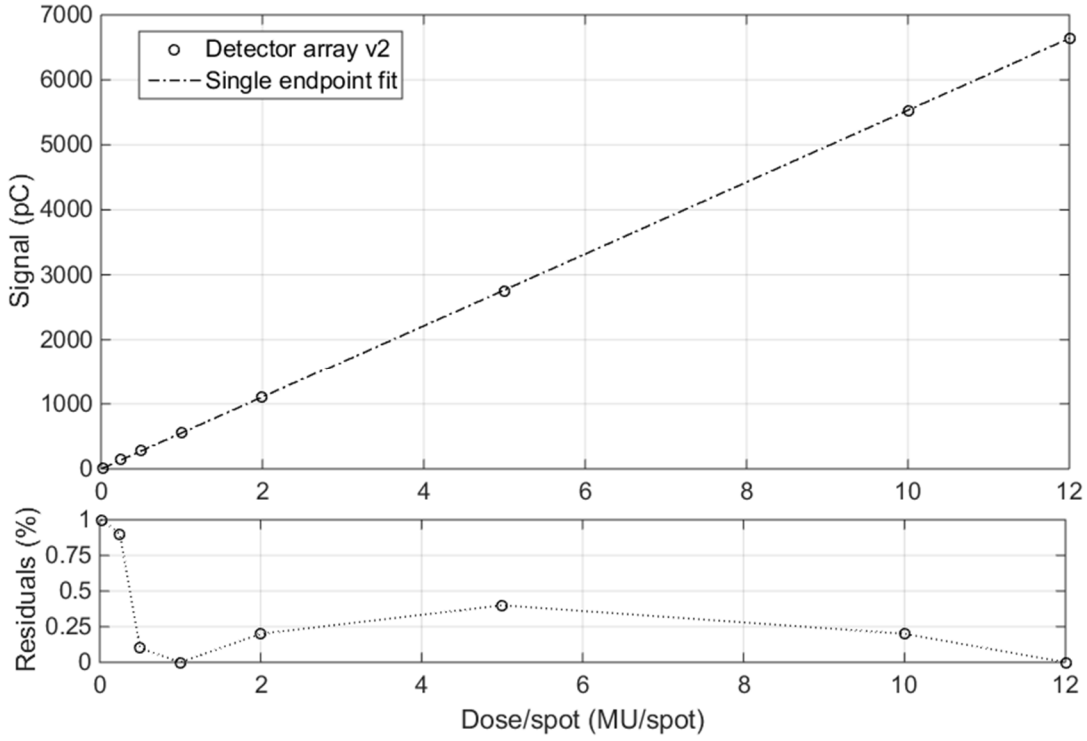

Figure 5.3. Integrated charge as a function of delivered dose for 100 MeV proton beam (top) and residuals from single end point linear regression (bottom).

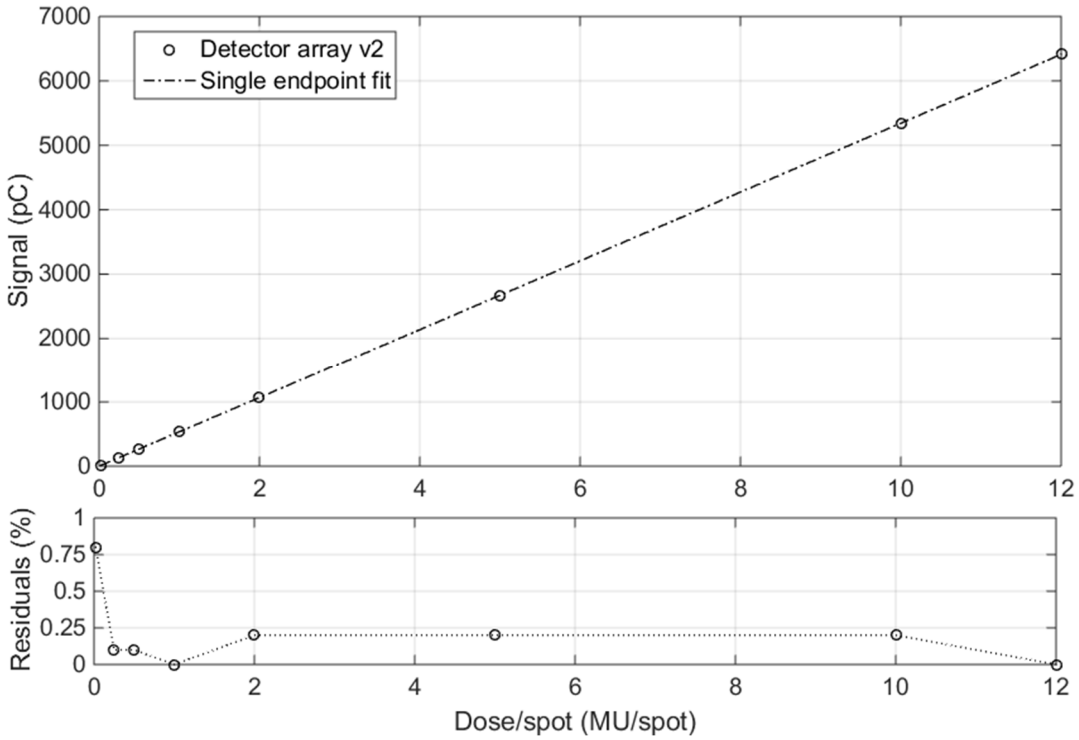

Figure 5.4. Integrated charge as a function of delivered dose for 165 MeV proton beam (top) and residuals from single end point linear regression (bottom).

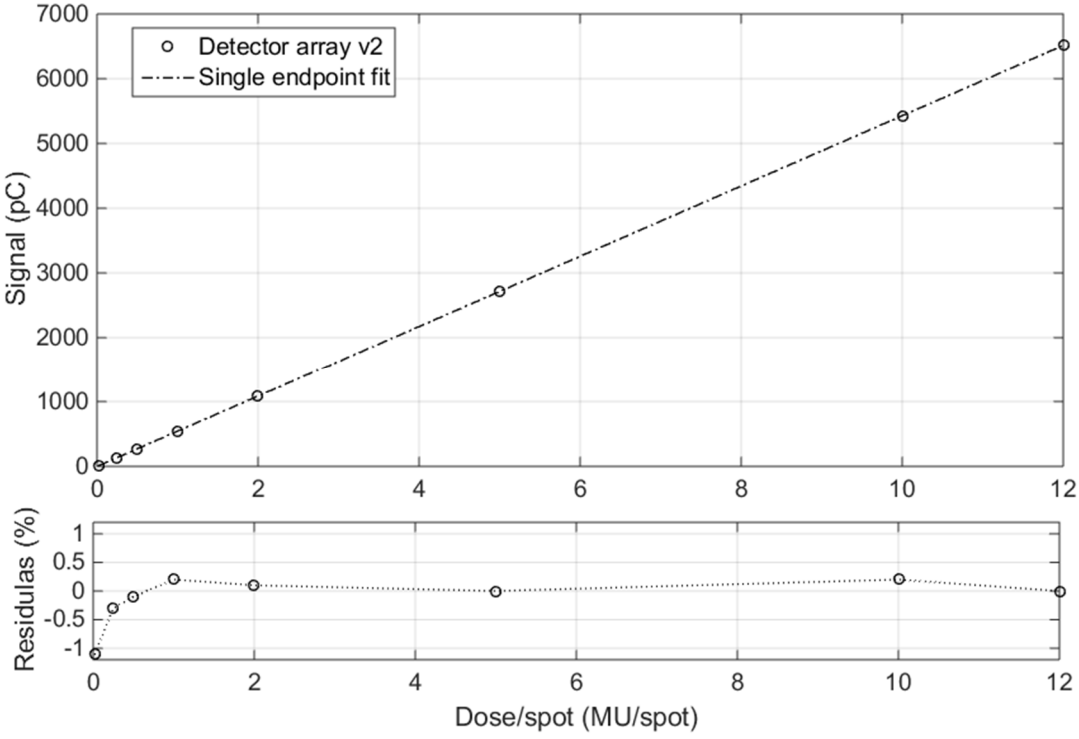

Figure 5.5. Integrated charge as a function of delivered dose for 226 MeV proton beam (top) and residuals from single end point linear regression (bottom).

5.2 MACHINE QUALITY ASSURANCE

External beam radiotherapy with proton pencil beam scanning mode is a relatively new treatment technique. The first worldwide clinical spot-scanning beam was delivered in 1996 at the Paul Scherrer Institut, Switzerland, and the first commercial PBS facility went clinical in 2008 at Massachusetts General Hospital, US. Therefore, no specific methods for machine QA have yet been suggested or introduced by AAPM or other organizations. As discussed in Paragraph 1.2.2, the AAPM TG 224 is expected to publish general guidelines in the year 2017.

The recent ICRU Report 78 [21] very briefly describes a limited number of machine QA procedures for proton therapy accelerators. The importance of machine QA checks has been described in the report, together with the major differences between QA of proton therapy machine and photon therapy LINACs, which are essentially due to parameters unique to proton therapy. For the time being, clinics have implemented their own procedures based on their experience and on the few recommendations available.

One of the major challenges in the execution of proton therapy machine QA checks is the availability of the accelerator time. The radiation beams are not as readily available as they are with conventional photon therapy machines, as proton therapy facilities typically operate with patients for 12–16 h per day. Thus, treatment rooms and beams are less accessible for QA measurements than photon machines are. Due to this fact, procedures originally based on film dosimetry and single detectors placed into a water tank become too time-consuming. Array detectors have been already introduced as a tool for machine QA [23, 88] that can guarantee the required accuracy and reduce the time dedicated to this activity. Therefore, arrays with high spatial resolution and high dosimetric properties are increasingly desired devices in proton therapy centers.

Two different tests for machine QA were performed with *detector array v2*:

- Measurement of uniform dose distributions;
- Measurement of pristine Bragg peak.

5.2.1 Measurement of uniform dose distributions

The proton beam transported from the extraction point of the accelerator to the treatment room has a narrow Gaussian transversal profile. Larger dose distributions with the required homogeneity for clinical applications can be obtained by scattering the beam or, as in the case of PBS, by scanning the beam over the target area. The lateral penumbra at the entrance of the medium is strongly dependent on the characteristics and the localization of the elements interposed in the beam. In depth, penumbra is largely determined by the multiple Coulomb scattering in the medium and thus may show large variations with depth. For these reasons, it is very important to characterize the penumbra and central beam regions of dose distributions, in a fashion similar to the procedures undertaken with MV X-rays (cf. Section 4.1.3).

Uniform dose distributions of different sizes were delivered to *detector array v2* at a 1.1 cm depth of measurement. The size of distributions was changed by changing the number of spots in each map. The sketch of spots map for the largest measured distribution is represented in Figure 5.6. The beam settings were as follows: 2.5 mm spacing between spots, 1 MU of dose delivered for each spot, and 6.2 nA treatment current at 226 MeV proton energy. Contrary to all other tests with protons reported in this thesis, the measurement of uniform dose distributions was carried out with a universal nozzle installed on the gantry. This type of nozzle allows for delivering both PBS and double scatter mode. Due to different characteristics and elements on the bream path, the size of the beam delivered through the universal nozzle is slightly larger than the sigma of the beam delivered through the PBS-dedicated nozzle. Specifically, at 226 MeV, the beam size in air increases to σ~4 mm with a universal nozzle; at the measurement conditions in other sections with a dedicated nozzle, the beam sigma is ~3 mm at 226 MeV.

Detector array v2 was benchmarked against two reference detectors: the 2D ion chamber array MatriXX PT (IBA Dosimetry GmbH, Schwarzenbruck, Germany), which features a 7.6 mm pixel spacing and a reduced volume compared to MatriXX^{Evolution} (volume[MatriXX PT]=0.4·volume[MatriXX^{Evolution}]), and the Lynx (cf. Section 2.2). Currently, the Lynx is one of the most used devices in clinics for machine QA purposes and relative dose measurements. Figure 5.7 shows the measured dose distributions along one of the spot map's main axis for four different distribution sizes.

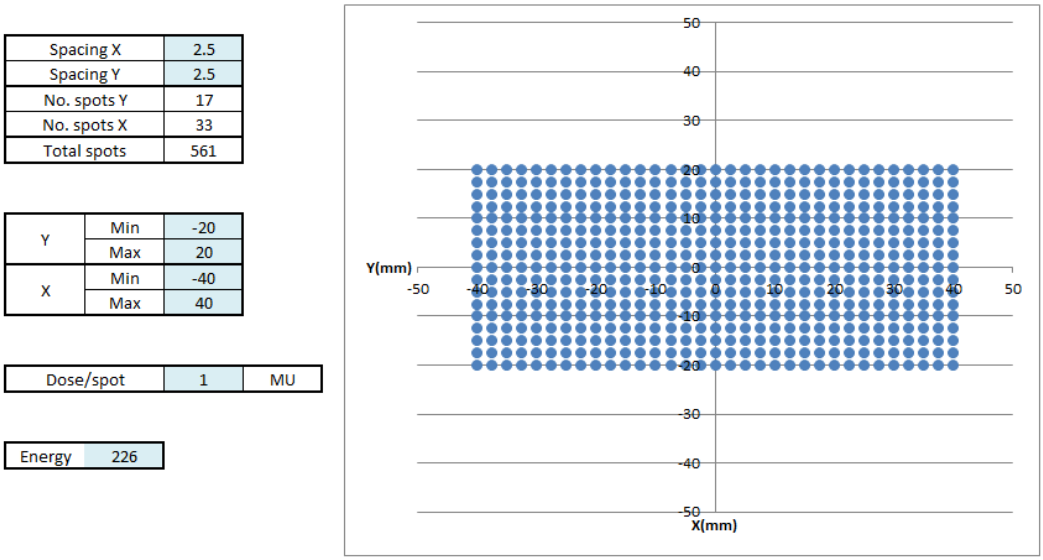

Figure 5.6. Example of PBS spots map (17x33 spots, spot spacing 2.5 mm). Each dot in the graph corresponds to a spot of 1 MU. All the information enclosed in the map are translated into a specific format file which can be read by the machine delivery system.

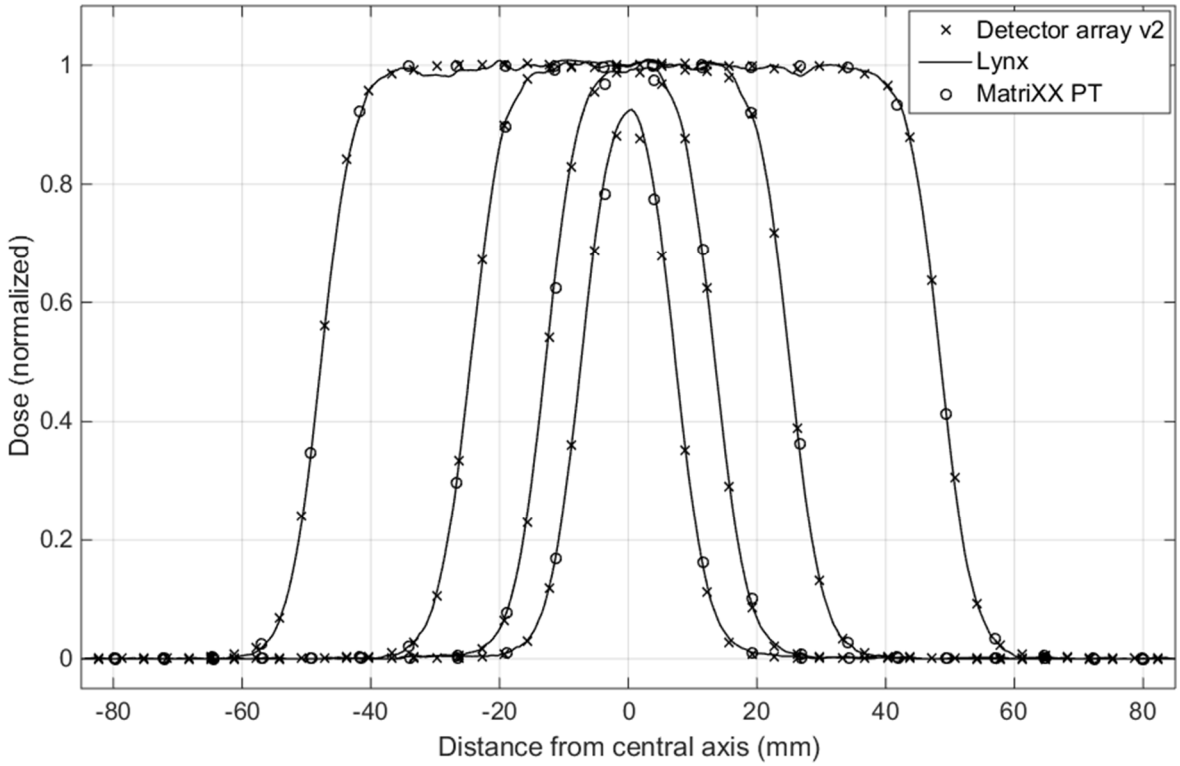

Figure 5.7. Relative dose distributions of 226 MeV proton maps delivered in PBS mode. Dimensions of delivered maps in number of spots are: 5x17, 9x17, 17x17, and 33x17. The spot spacing is 2.5 mm. Profiles are normalized to a large one to compensate for non-uniformity.

The agreement between *detector array v2* and Lynx is excellent over the entire distribution length. Penumbra are accurately defined thanks to the small inter-chamber distance. Narrow distributions made of only five spots can be measured with good accuracy.

5.2.2 Measurement of pristine Bragg peak

The measurement of pristine Bragg peak during commissioning is usually performed with a single ionization chamber inserted into a scanning water tank. In spite of its high level of accuracy, this approach is not suitable for daily QA activities. This is because of long setup and measurement times, as well as the fact that more efficient solutions have been developed. For instance, multi-layers ion chamber devices currently available on the market are able to reconstruct Bragg peak distribution in one single radiation shot [89].

On a daily basis, one of the most important checks performed in proton therapy clinics is the range verification of proton beams. This is the most sensitive measurement for monitoring the consistency of the cyclotron energy, which is a fundamental prerequisite for dose calculation by TPS. The clinical range of a beam of protons with identical (or nearly identical) energy is defined as the depth of 90% dose level at the distal edge of the pristine Bragg peak curve [11, 20]. Sometimes, the range can be also defined in literature as physical range, meaning the 80% of the distribution maximum in the distal region [90]. In QA procedures, the range is typically verified for different proton energies (e.g. the lowest available, the highest available, and one middle-range energy).

During daily range verification, the consistency of a few parameters of the pristine Bragg peak distribution (e.g. 80% proximal range and distal range at 50% dose level) can be verified with respect to baseline values. These values are determined, for instance, during commissioning or after changes in machines/beam line components (e.g. the ions source in the cyclotron, changes in the beam deflectors, etc.). Some clinics have already started to use 2D array detectors to perform range verification on a daily basis. This method consists of the use of plastic wedges of different thicknesses being placed upstream of the detector in order to reproduce different depths of measurement. Typically, the range at four energies can be verified by using the whole sensitive area (20x20 cm^2 or more) of the array. It should be noted that, with this technique, only the proximal and distal part of the Bragg peak and not

the complete dose distribution can be reconstructed, due to the limited number of sensors on the active area.

A similar approach was used for range and pristine Bragg peak measurements with *detector array v2*. Using the setups of Figure 5.8, the complete Bragg peak curve was reconstructed with two irradiations. Measurements were repeated with 100 MeV and 145 MeV proton energies. Due to setup difficulties, it was not possible to measure complete distributions for higher energies during these measurement sessions (at least 33 cm of RW3 would be required to measure the Bragg peak at 226MeV). Rectangular spots maps were delivered to cover the whole length of the detector, and a conversion factor was applied to raw data to account for RW3 to water mass stopping power ratio. This conversion factor is used to convert the RW3 thickness into water-equivalent thickness, and it has been measured in the clinic taking an average over three different energies (i.e. 100, 150 and 226 MeV) since it is energy dependent. Measured curves were compared with those from a Bragg peak chamber (PTW, Freiburg, Germany) taken in a water tank. This chamber is a parallel plate ionization chamber with a 84 mm diameter and a sensitive volume of 10.5 cm^3. Bragg peak distributions are shown in Figure 5.9.

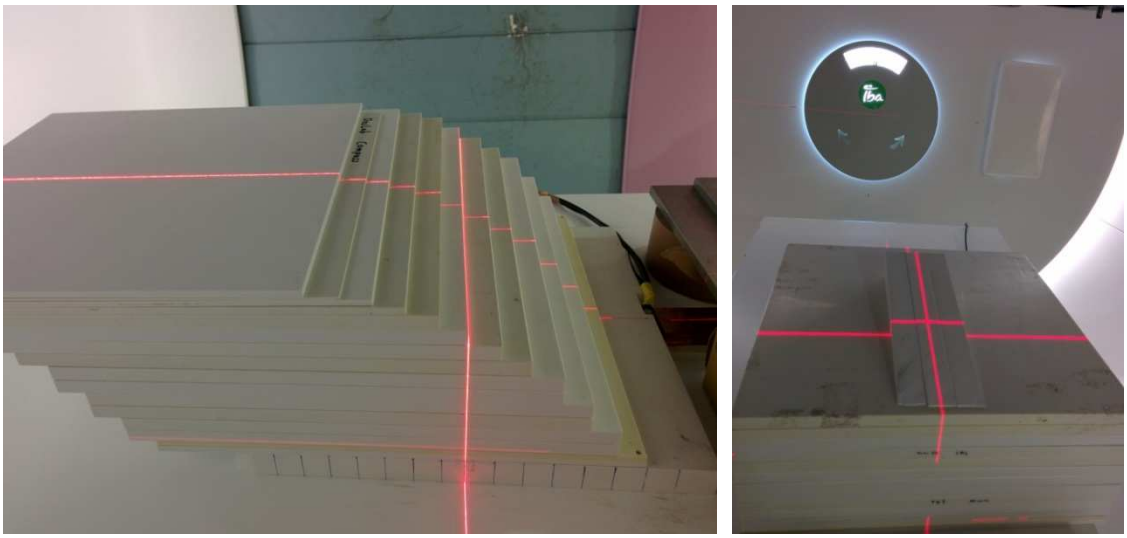

Figure 5.8. Experimental setup for measurement of pristine Bragg peak curves with *detector array v2*. RW3 slabs were piled on top of the detector to simulate different depths in the plateau region (left). A RW3 wedge with a slope of 0.5 mm/3.5 mm was used to define the Bragg peak region. RW3 water-equivalent factor is 1.022.

Measured curves for the two energies show a good agreement with the large chamber in the plateau region, in the proximal part, and in the distal part of the Bragg peak. The peak region was fitted with the analytical model developed by Bortfeld [90] (Figure 5.13), which is generally accepted as the best model with which to approximate a Bragg peak distribution and is valid for proton energies between approximately 10 and 200 MeV. Its main four constituents are: 1) a power-law relationship describing the range-energy dependency; 2) a linear model for the fluence reduction due to non-elastic nuclear interactions; 3) a Gaussian approximation of the range straggling distribution; 4) a representation of the energy spectrum of poly-energetic beams constituted by a Gaussian distribution with a linear "tail". The analytical model is thus defined by the formula:

$$D(z) = \Phi_0 \frac{e^{-(R_0-z)^2/4\sigma^2}\sigma^{0.565}}{1+0.012R_0}\left[11.26\sigma^{-1}\xi_{-0.565}\left(-\frac{R_0-z}{\sigma}\right) + \left(0.157+11.26\frac{\epsilon}{R_0}\right)\xi_{-1.565}\left(-\frac{R_0-z}{\sigma}\right)\right] \tag{5.1}$$

which is valid for $R_0 - 10\sigma \leq z \leq R_0 + 5\sigma$ (where z represents the depth in water). In Eq. (5.1), Φ_0 is the primary particle fluence, R_0 is the distal range at 80% dose level, σ represents the width of the Gaussian range spectrum, ϵ is the fraction of primary fluence contributing to the "tail" of the energy spectrum, and $\xi_y(z)$ is the parabolic cylinder function tabulated in literature [91].

The model, together with the computation of the ξ function, has been re-implemented into a MatLab routine. The parameters of the fitting function have been determined by minimizing the sum of square residuals between fit and data. In the original work by Bortfeld, the author compares the analytical model to several data measured with different probes and different proton energies. The results of this comparison show that the agreement between data and fit is always within the measurement error, thus proving the accuracy and reliability of the model.

The values extracted from the Bortfeld analytical model for both curves measured with *detector array v2* and the large ionization chamber are summarized in Table 5.1. It can be seen that *detector array v2* and the Bragg peak chamber are in agreement within sub-millimetric differences.

Table 5.2 summarizes the fit parameters calculated for interpolation of curves measured with *detector array v2*.

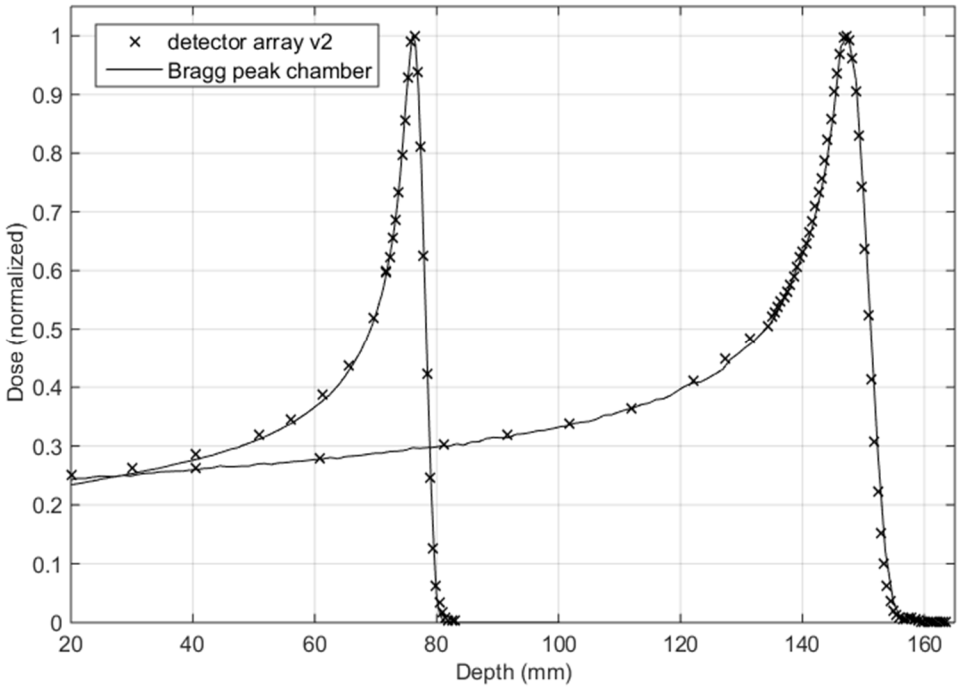

Figure 5.9. Pristine Bragg peak curves measured with *detector array v2* and with the Bragg peak chamber for 100 MeV and 145 MeV proton energies. Curves are normalized to maximum.

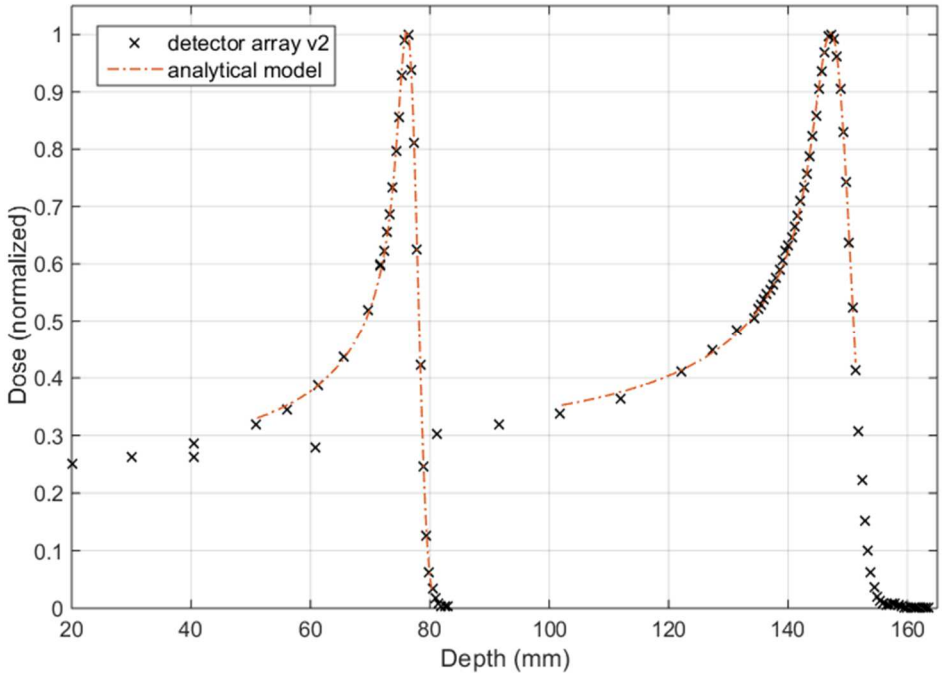

Figure 5.10. Analytical model applied to experimental data from *detector array v2*.

Table 5.1. Proximal range (80% dose level in the proximal part of the peak), distal range (80% and 50% dose level in the distal part of the peak) and peak width (difference between 80% distal and proximal range) extracted from the interpolation of measured data with the Bortfeld analytical model.

	Detector array v2		*Bragg peak chamber*	
Values (mm)	100 MeV	145 MeV	100 MeV	145 MeV
Range Proximal (80%)	74.34	143.74	74.29	143.95
Range Distal (80%)	77.36	149.40	77.39	149.63
Range Distal (50%)	78.19	150.95	78.25	151.20
Peak width	3.02	5.67	3.09	5.69

Table 5.2. Parameters of the analytical model from [90], implemented into a MatLab routine and applied to the measured data. The parameters are calculated with an end tolerance over the fitting iterations of 10^{-4}.

Free parameters of the MatLab analytical model implementation	*Detector array v2*	
	100 MeV	145 MeV
Φ_0 - primary particle fluence (mm^{-2})	0.0263	0.0365
R_0 - distal range at 80% dose level (mm)	77.3586	149.4029
ϵ - fraction of primary fluence contributing to the "tail" of the energy spectrum	0.1624	0.3944
σ - width of the Gaussian range spectrum (mm)	1.3228	2.4796

5.3 PATIENT QUALITY ASSURANCE

As briefly described in Paragraph 1.1.2.3, intensity-modulated proton therapy is performed by irradiating the tumor volume with a scanning pencil beam. The tumor volume is divided into different layers that are covered by non-uniform dose distributions one after the other. Different beam energies are selected to move between different layers. The concept of IMPT with PBS beams is visually reproduced in Figure 5.11.

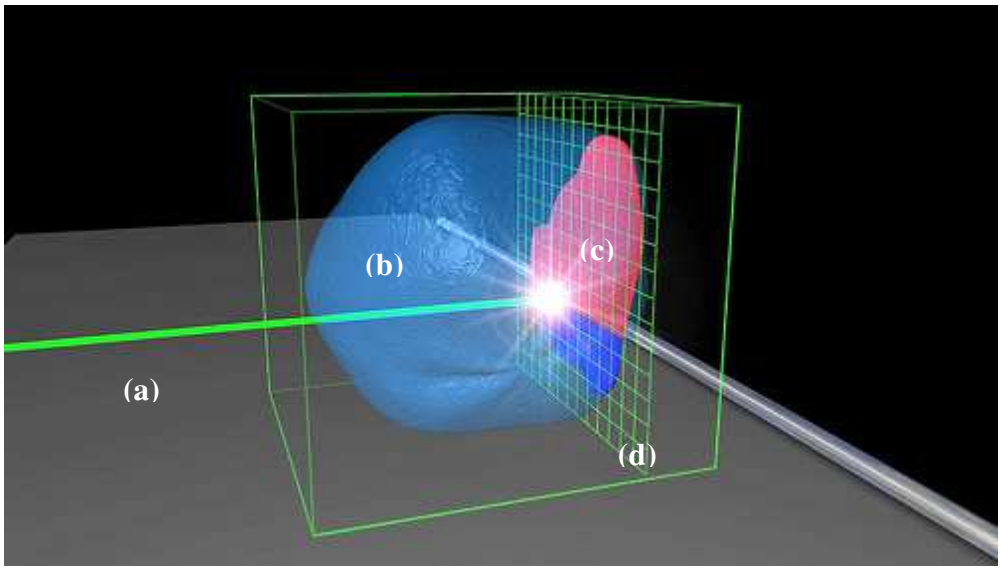

Figure 5.11. Graphical representation of PBS IMPT. A proton pencil beam scans layer by layer to cover the complete target volume with high precision. In each layer (represented by the green grid (d)), position and intensity of spots are adjusted to achieve a final uniform coverage of the tumor. Each layer is characterized by a defined proton energy (i.e. a defined range). In the picture, the beam is represented by the green pencil ray (a) impinging on the target (b); the part of the target already irradiated is represented by pink color (c).

The complexity of such delivery techniques requires accurate verification of plan delivery to ensure that the patient receives the prescribed dose and to avoid both under-dosage in the target volume and over-dosage in the surrounding healthy tissues. In clinics, it is common practice to perform specific patient plan verification for every patient being treated. This is done at the beginning of the treatment and after each re-planning.

Planar dose distributions are typically verified at selected depths, such as at the distal, middle, and proximal range in the target volume. The number of layers to be verified may vary based on the complexity of the plan, the volume and the localization of the tumor. One of the most

widely used systems for patient plan verification consists of a 2D ion chamber array placed in a scanning water tank (Figure 5.12). The detector measurement surface can be moved at different depths in water. Moreover, for each selected measurement depth, the complete plan is irradiated from a fixed incidence direction. In the TPS, the whole plan is applied to an ideal cube of water and then the computed distributions are compared to the measured ones. This system was also used to benchmark measurements of patient QA performed with *detector array v2*.

Figure 5.12. The 2D commercial ion chamber array MatriXX PT placed in the DigiPhant water tank (IBA Dosimetry GmbH, Schwarzenbruck, Germany). The detector can be shifted along the longitudinal beam axis to reproduce different depths of measurement in water.

5.3.1 Patient verification through comparison of linear dose distributions

Preliminary tests of patient plan verification were performed with *detector array v2* for an IMPT treatment of a prostate tumor, which is by far the most treated tumor in proton therapy.

To compare the measurements with the TPS and the 2D array in the water phantom, the depth of measurement was changed by adding RW3 layers upstream of the linear array (Figure 5.13). Irradiation was delivered from a 0° fixed gantry angle. The selected plan consists of two irradiations delivered from two opposite directions. The beams impinging on the target volume and the resulting isodose curves are shown in Figure 5.14. Each beam is made of more than 20 layers, with energies approximately in the interval 143–210 MeV. Measurements were performed at three different depths: 23 cm, 20 cm, and 17 cm. These

correspond to regions in the distal, middle, and proximal parts of the target volume, respectively.

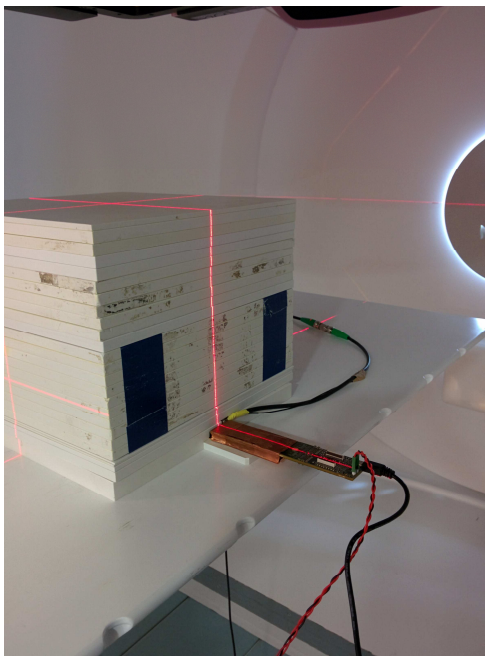

Figure 5.13. *Detector array v2* placed in the dedicated phantom on the treatment couch, with several RW3 slabs on top to adjust the depth of measurement. Both SSD and SDD was changed for each irradiation to keep the isocenter at the fixed depth of 15 cm.

Again, comparison between *detector array v2*, the 2D array MatriXX PT, and the TPS XiO (Elekta AB, Stockholm, Sweden) was based on relative differences of linear dose distributions. Both the MatriXX PT and *detector array v2* were aligned by means of the in-room laser positioning system along the main beam's central axis. Ionization chambers in the MatriXX PT are arranged in a square grid, with a distribution that is symmetric to the central axis of the detector. Thus, no ion chambers are placed on the symmetry axes, and the nearest columns (or rows) of pixels are placed 3.8 mm from the axes. Figure 5.15 shows the pixels' arrangement in the MatriXX PT detector.

Since the dose distribution can significantly change within a distance of a few mm in a layer irradiated in IMPT with PBS mode, two linear dose distributions have been extracted from the TPS data in order to match the different measurement positions of MatriXX PT and *detector array v2* pixels.

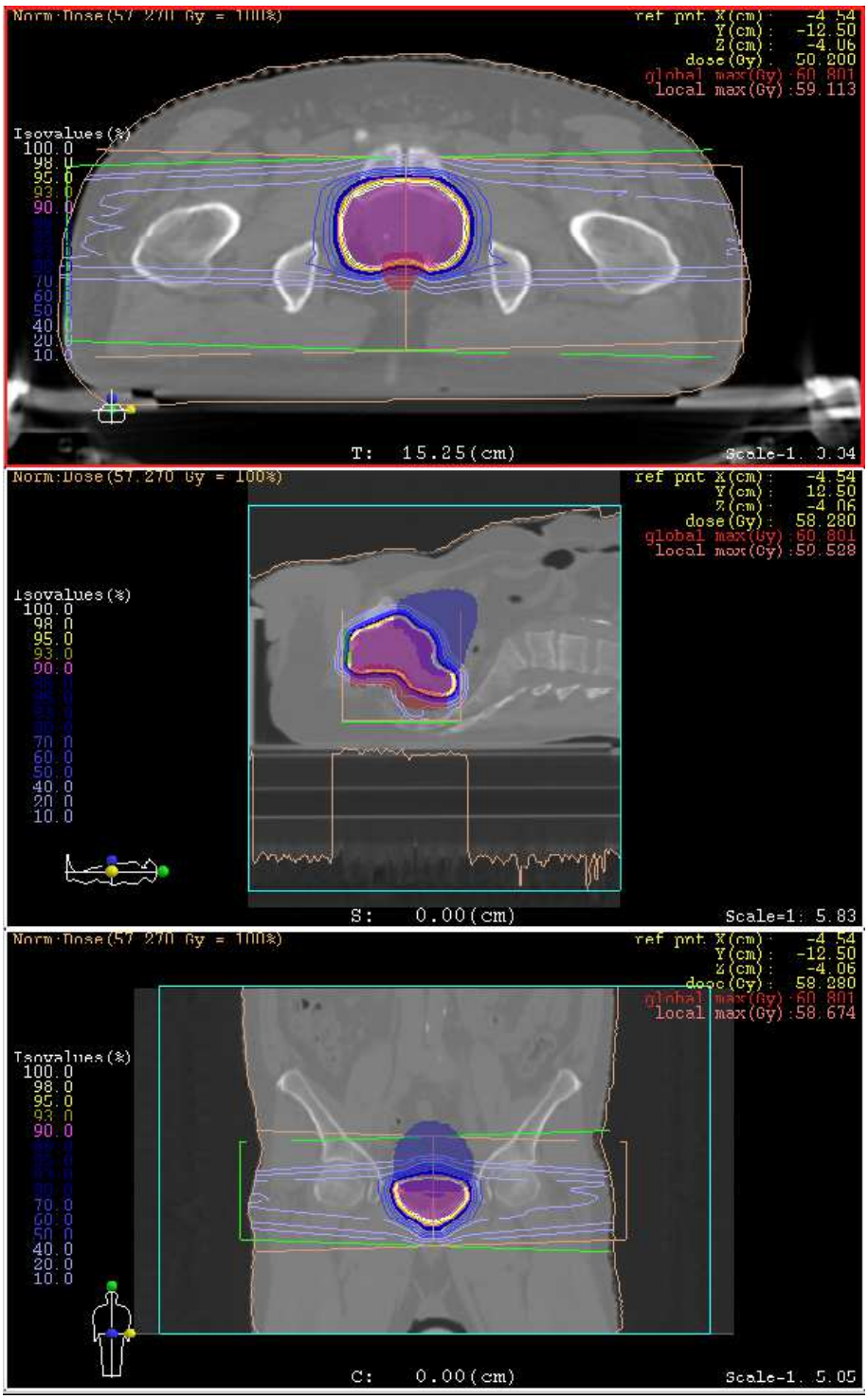

Figure 5.14. Images from XiO TPS that show the two beams applied to the patient CT and the resulting isodose curves.

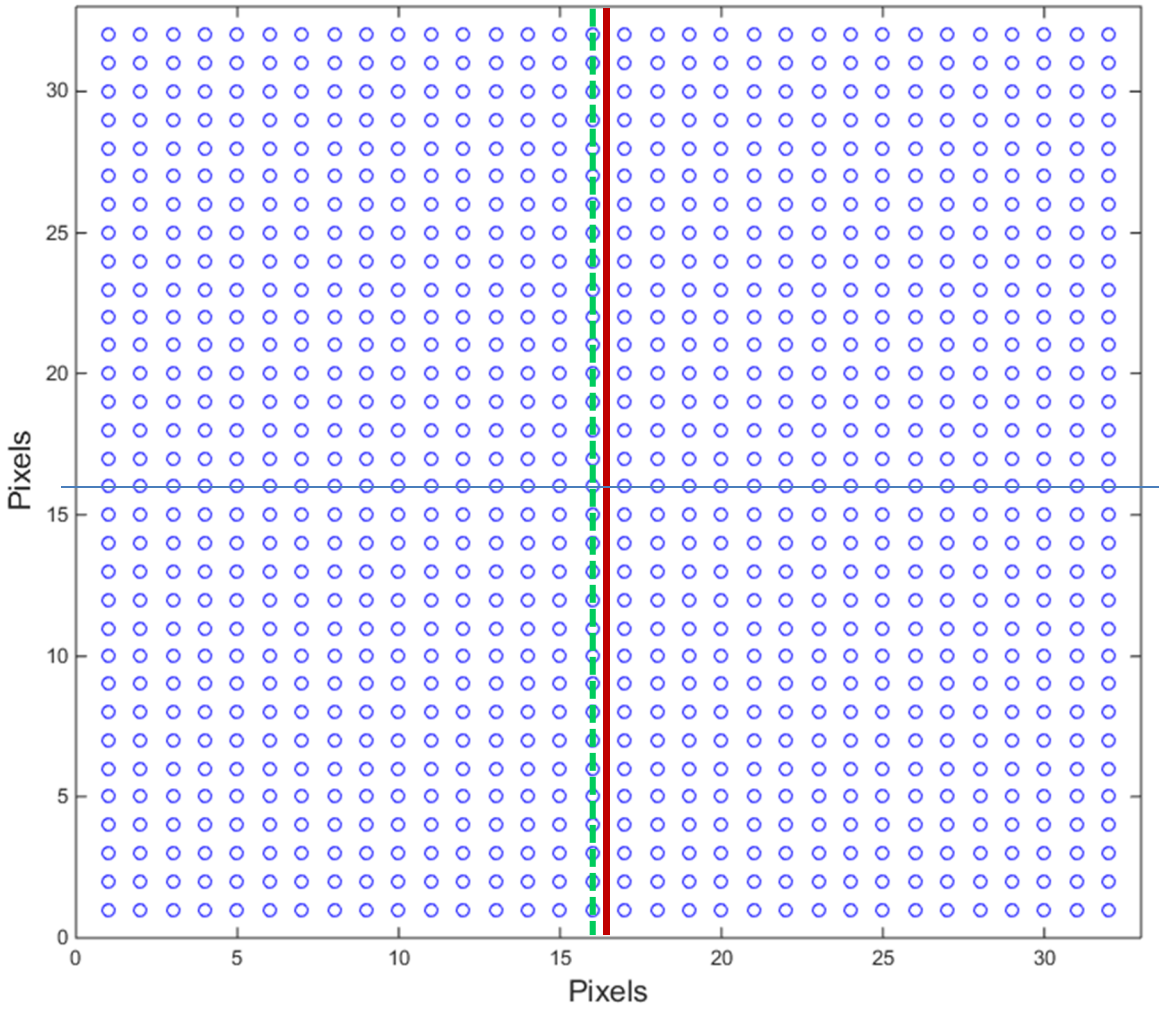

Figure 5.15. MatriXX PT pixels grid (circular markers) and symmetry axes. The laser corresponding to beam's central axis (and to measurement position of *detector array v2*) is represented with a red line. The reference TPS distributions were calculated along the red line for comparison with *detector array v2* and along the green dotted line for comparison with MatriXX PT.

The results of the patient plan evaluation are plotted in Figure 5.16 (Beam 2, middle and proximal range) and Figure 5.17 (Beam 1, distal range). The measured distributions are compared to TPS and relative deviations are calculated.

The average difference between TPS and *detector array v2* was found to always be below 1%. Detector performances are generally comparable with those of MatriXX PT, even if a better definition can be achieved when the modulation of the dose distribution is high. This effect is particularly evident in the measurements of distal distribution of Beam 1 (Figure 5.17).

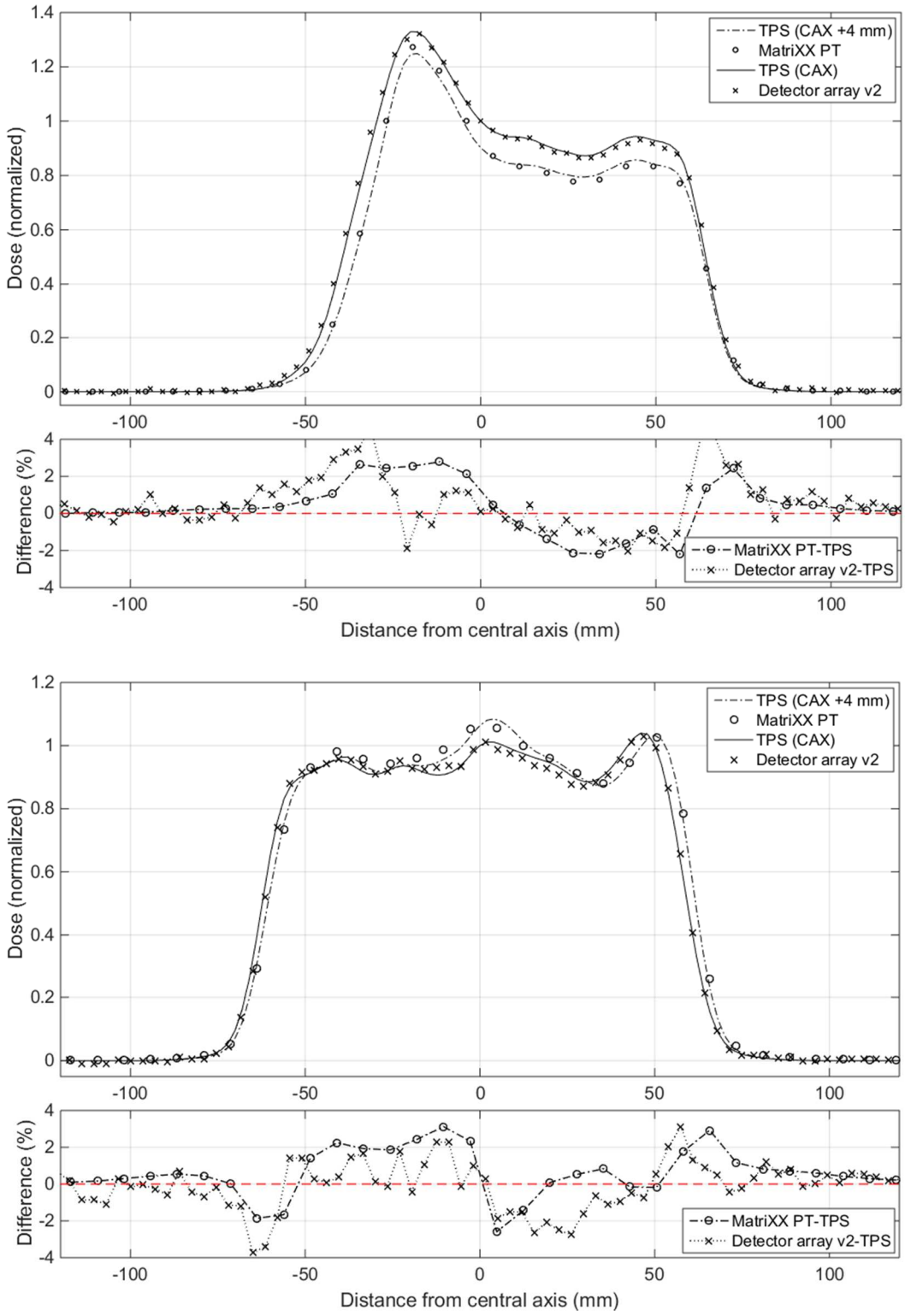

Figure 5.16. Dose distributions and relative differences between TPS and detectors in the middle region (20 cm depth, top) and the proximal region (17 cm depth, bottom) for Beam 2. *Detector array v2* and MatriXX PT show comparable performance, even though the linear array can reproduce the dose distribution with higher resolution.

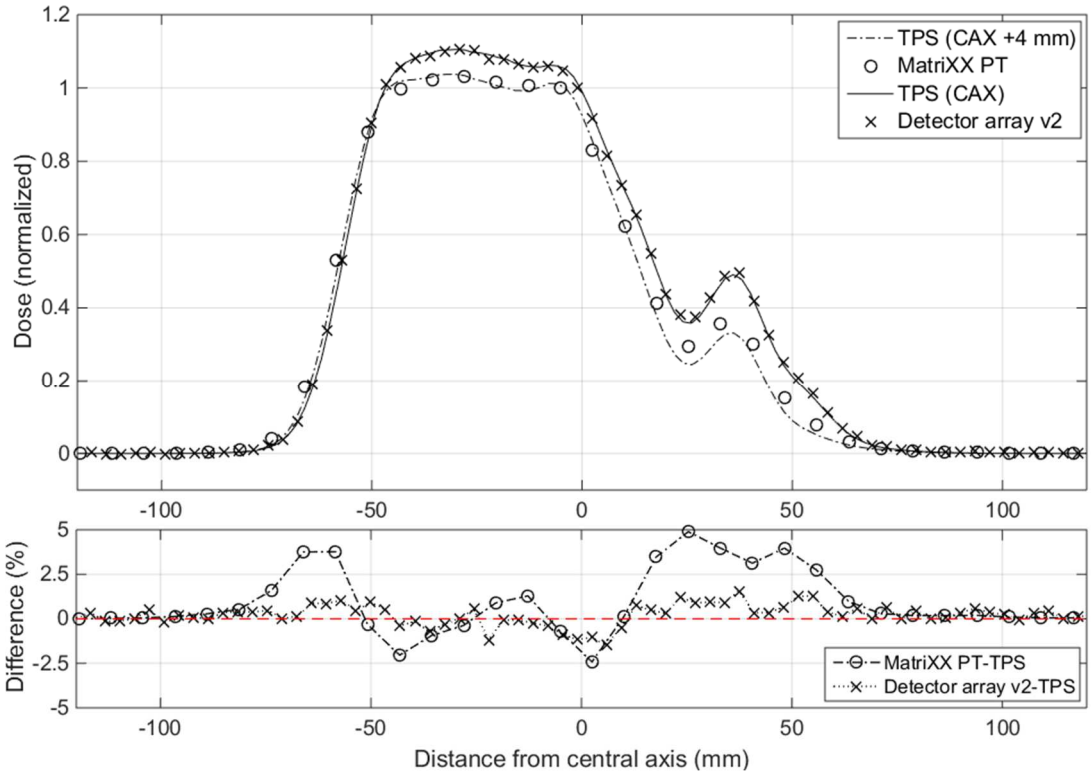

Figure 5.17. Dose distributions and relative differences between TPS and detectors in distal region (23 cm depth) for Beam 1. The capability of the linear array to reproduce the IMPT distribution with high accuracy is noticeable.

5.4 DISCUSSION

Basic dosimetric properties of the new ion chamber technology were assessed for clinical pencil beam proton beams. The absence of major ion recombination was proved in the most critical condition achievable with clinical beams generated by a cyclotron machine. The detector working point was set to a moderate bias (250 V), which ensures a collection efficiency higher than 99.4% with a 6.2 nA proton current.

The response of *detector array v2* was also proved to be linear with dose over the typical clinical range of energies. Moreover, response linearity with dose rate was assessed at the same time by increasing the beam current impinging on the detector. The overall detector linearity was found to be within 1.1% for all the energies.

The ability of *detector array v2* to accurately reproduce uniform dose distributions and depth dose curves was proved. Excellent results were achieved thanks to the high spatial resolution and the 27.6 cm active length of the detector. The quality of results was verified by comparison with reference detectors that are typically used in clinical routines. Moreover, the detector exhibited a remarkable versatility and suitability to different applications.

Profiles of dose delivered with IMPT technique in PBS mode were measured with *detector array v2*. A general agreement with the distributions computed through the TPS was found. Heterogeneous dose coverage can be reproduced thanks to the high spatial density of pixels in the detector. Other relevant features are practicality and instantaneous readings.

After a complete assessment of dosimetric properties, the new ionization chamber technology has been proven to be ideal for applications in proton therapy dosimetry. Both for machine QA and patient QA, the performances were compared to standard reference detectors and procedures typically used in clinical routines. The technology appears to be a very promising tool for routine QA applications, where fast and reliable measurements of some beam parameters (such as beam output, range, and uniformity) have to be performed. An array based on this technology could be, for instance, coupled with a plastic phantom in order to measure PBS beam parameters and range at different energies in one single irradiation.

Moreover, encouraging results were achieved in view of a possible application to patient QA in intensity modulated proton therapy. The built prototype can reconstruct dose distributions

generated through pencil beam delivery. To evaluate these performances, *detector array v2* was benchmarked to MatriXX PT, which is one of the most widely used detectors for patient QA. The *detector array v2* exhibits a better accuracy than MatriXX PT in reconstruction of steep gradient of dose thanks to the reduced pitch. To the knowledge of the author, there are only two more commercial devices based on ionization chambers that can be used for patient QA in proton therapy, and these show a pixel pitch of 10 mm and 7.1 mm, respectively [92, 93].

It is clear that more clinical cases need to be measured in order to complete the evaluation of the technology in view of patient QA applications. Additionally, as with conventional radiotherapy with MV X-rays, a 2D detector is a mandatory solution in this case.

Chapter 6 DESIGN AND IMPLEMENTATION OF A 2D DETECTOR

As already discussed in previous chapters, a detector with at least a 2D-sensitive region is necessary for machine QA and patient QA in radiation oncology. Regardless of this, linear arrays or detectors which are a 2D combination of a few linear arrays can find some applications, especially in machine QA and LINAC commissioning [94, 95].

At the end of the characterization of the prototype *detector array v2*, and considering the positive results achieved, the design and subsequent implementation of a 2D device based on the developed ionization chamber technology has been carried out. A *detector array v3* has been built featuring all the major characteristics of a possible commercial detector. The proof of concept of this 2D device is described in this chapter.

A general description of the new device is presented in Section 6.1 including the concept, the design, and the readout system.

Section 6.2 summarizes the initial testing and debug phase performed with MV X-rays radiation.

In Section 6.3, preliminary measurements with PBS proton beams are presented. These measurements consist of beam profiles measurements, linearity with MU/spot, and two initial examples of patient plan verification.

The performances and limits of the present prototype are discussed in Section 6.4.

6.1 GENERAL DESCRIPTION

The prototype named *detector array v3* was developed with the following purposes:

- to extend the technology investigated in previous sections to a 2D sensor, thus providing a high-performance alternative for existing 2D arrays;
- to prove the working principle of a modular sensor design, which could be useful in building arrays with uniform area coverage;
- to introduce a new firmware for the readout electrometer already used with *detector array v*2, in order to optimize the performances of data acquisition and to take into account the specific needs of dosimetry;
- to prove the concept of a selective readout scheme, intended to increase even further the flexibility of the technology in view of its commercial application. The concept is described in the following text.

Detector array v3 consists of four base modules. Each module is a 2D sensor itself, with 32x8 ionization chambers arranged in a uniform grid and connected to two electrometer chips (the same used to readout the *detector array v2*). A sketch of a single module is presented in Figure 6.1.

In a base module, pixels are connected to the electrometers in a 'chessboard-like' scheme: one half is connected to one electrometer, the second half to the second electrometer. If one electrometer is disconnected or turned off, the active pixels are arranged as shown in Figure 6.2. Only when both the electrometers are active the grid of ionization chambers is completely readout.

This particular pixel-electrometer connection was introduced in order to increase the flexibility for commercial implementations. The cost of a commercial detector is significantly influenced by the number of electrometers, and the final user may want to choose a less expensive solution with a lower resolution for some applications (e.g. daily machine QA), while a more expensive solution with higher resolution may be selected for specific applications (e.g. patient QA). By removing one electrometer from a base module, it is possible to reduce the number of readout channels by one half, thus reducing the spatial resolution but retaining a uniform coverage of the sensitive area. The discussed readout

modality is a general concept which can be applied to other area devices, and it has been patented by IBA Dosimetry GmbH [96].

A single base module is made using the same PCB and electrode materials used for the *detector array v2* prototype. The inter-chamber distance has been set to 4 mm (compared to the 3.5 mm of *detector array v2*) in order to increase the buildup material between each chamber. The pixels have a square cross-section of 2x2 mm^2, and the nominal active volume of each chamber is 6 mm^3 when the top electrode is coupled with the base module printed circuit board. The height of the active volume has been increased from 1 mm to 1.5 mm to increase the sensitivity at the expense of charge collection efficiency, which was excellent in *detector array v2* and is expected to remain within adequate values after this modification. When one or more modules are coupled together, the inter-chamber distance is preserved across the edges.

Figure 6.3 shows *detector array v3*, made of four base modules coupled together and inserted into a dedicated RW3 phantom.

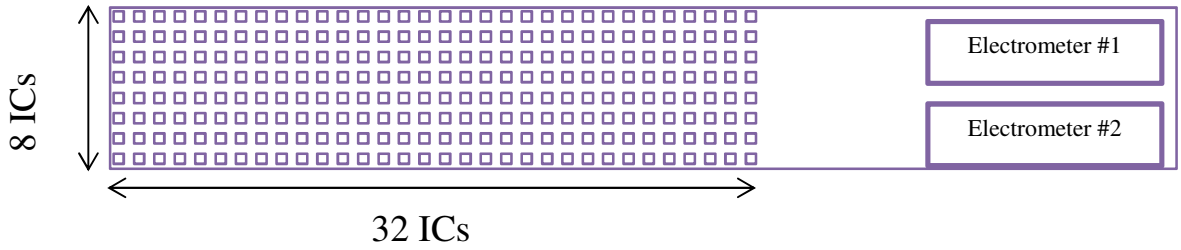

Figure 6.1. Layout of a single base module, which consists of 256 ionization chambers (ICs) that are arranged in a uniform grid of 8 rows and 32 columns, and readout by two electrometers.

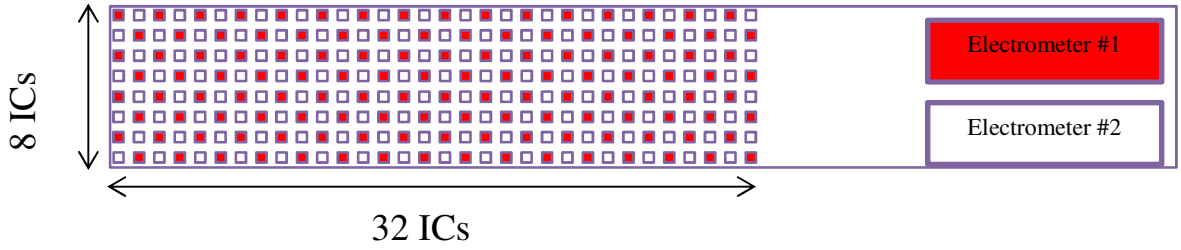

Figure 6.2. Connection between electrometers and pixels in a base module. The pixels connected to Electrometer #1 are marked in red. When both electrometers are active, the signal is collected from the whole pixel grid.

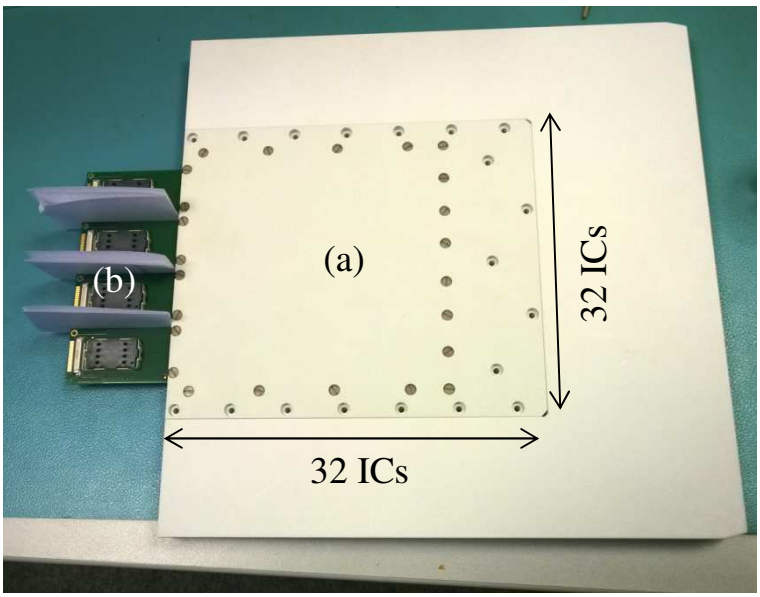

Figure 6.3. Bottom view of *detector array v3* when inserted into a RW3 phantom. The sensor consists of four modules coupled together to generate a uniform 32x32 grid of ionization chambers, thus resulting in an active area of 12.4x12.4 cm^2 (a). Each module is readout by two electrometers, connected to a firmware board through a connector placed on one side of the printed circuit board (b).

6.2 PRELIMINARY CHARACTERIZATION WITH MV X-RAYS

The preliminary dosimetric characterization of the detector began at IBA Dosimetry DosLab, with repeated irradiations under MV X-rays beams (Agility LINAC) in order to evaluate the ability of the device to measure square fields.

Detector array v3 was placed in its dedicated phantom, with a total RW3 buildup of 5 cm, at a source surface distance of 100 cm, and biased at 200 V. 6 MV photon beams of different sizes were delivered at a 300 MU/min dose rate. The measurement setup is shown in Figure 6.4.

Examples of measured beams are reported in Figure 6.5. No uniform correction was applied to these data, in order to evidence the native uniformity of the array. The standard deviation of the sensitivity normalized to its mean value over the 10x10 cm^2 field region is about 5%; variations in this order of magnitude are typically corrected through a gain calibration under continuous gamma radiation.

Beam profiles were measured at different field sizes, normalized to a larger field (12x12 cm^2) and compared with a MatriXX^{Evolution}. The analysis of beam profiles is shown in Figure 6.6.

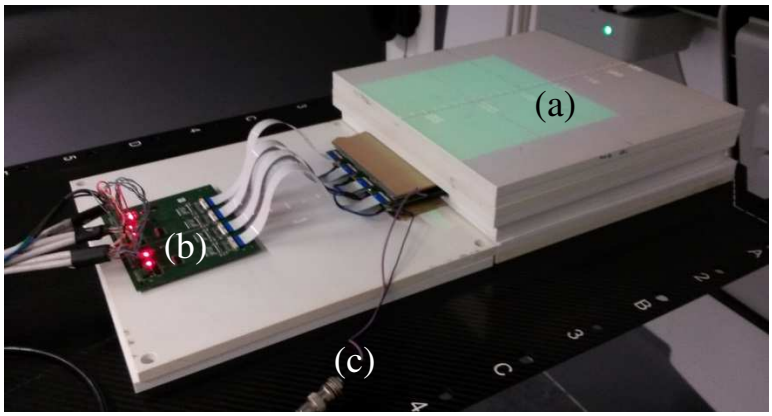

Figure 6.4. *Detector array v3* setup for measurements of uniform 6 MV photon beams. The device has 5 cm RW3 on top (a) and 3 cm RW3 of backscatter. The eight electrometers are connected to the FPGA board (b), which is placed far from the radiation field. Bias is applied through an external connection (c).

The 2x2 cm^2 dose distribution can be accurately reconstructed with *detector array v3*, whereas the MatriXX is operated at its limit due to the 7.6 mm pitch.

Profiles of unflattened beams were not acquired in this first assessment step. They have been postponed to a subsequent phase of the characterization process.

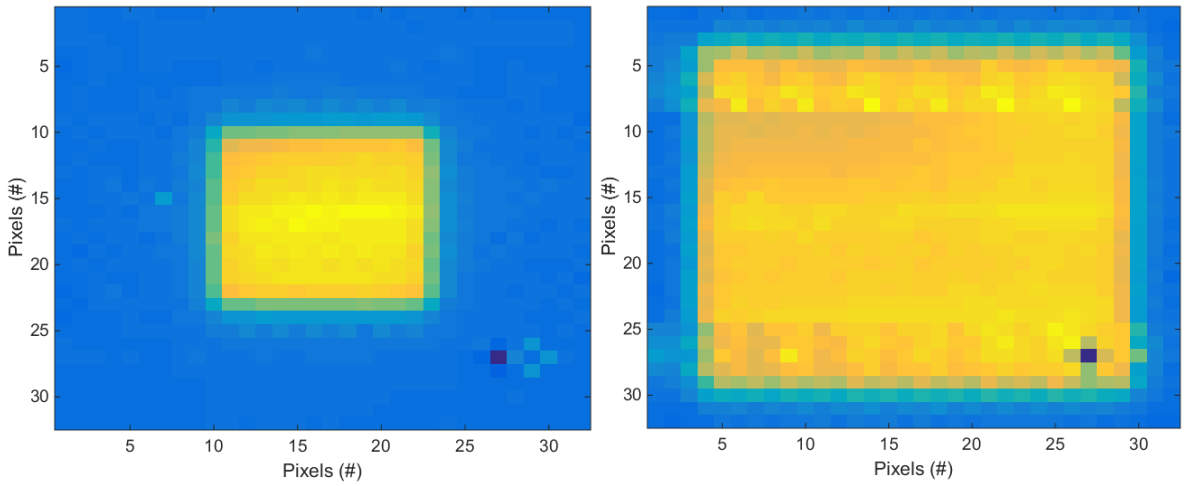

Figure 6.5. Measured 6 MV beam for 5x5 cm^2 field size (left) and 10x10 cm^2 field size (right). Uniformity correction factors are not applied to the measured data, and intensities are given in arbitrary values. There is one pixel (coordinates [27,27]) that clearly underestimates the signal and has not been taken into account in the evaluation of the sensitivity fluctuation compared to its mean value.

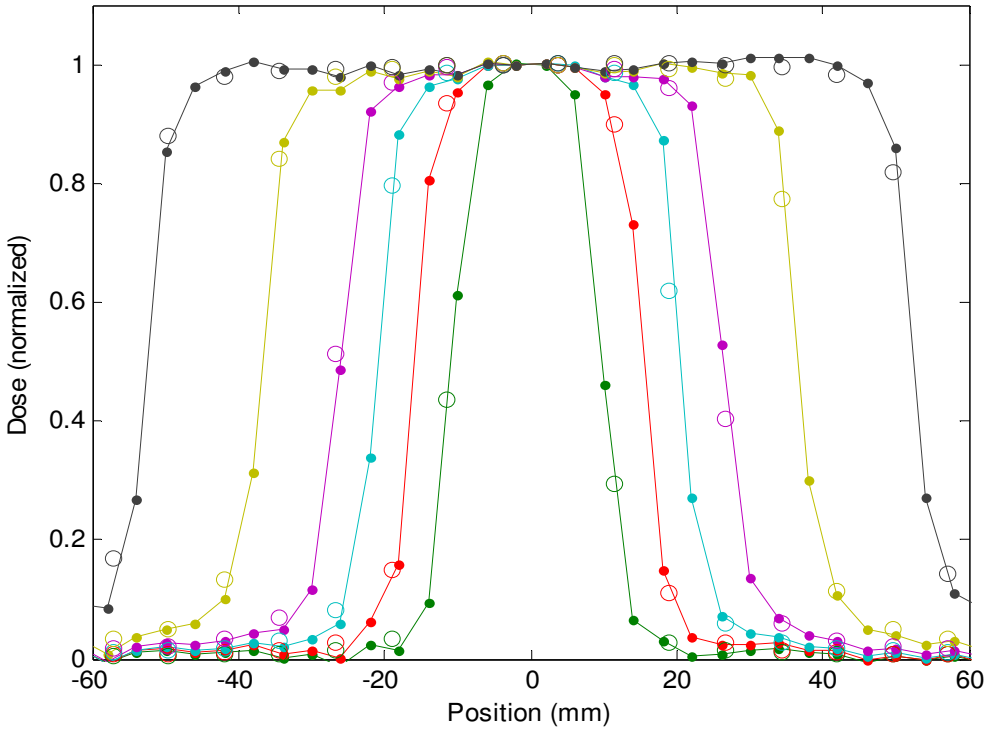

Figure 6.6. Comparison of beam profiles for 6 MV beam quality between MatriXX (open markers) and *detector array v3* (line). Profiles (2x2 cm^2, 3x3 cm^2, 4x4 cm^2, 5x5 cm^2, 7x7 cm^2, 10x10 cm^2) are normalized on the beam central axis.

6.3 PRELIMINARY CHARACTERIZATION WITH PROTON BEAMS

As explained in Chapter 5, a 2D detector might be suitable for a number of applications in quality assurance of proton therapy beams. Therefore, *detector array v3* was tested with PBS proton beams at the Proton Therapy Center Czech s.r.o. (Prague, Czech Republic), as had been done for *detector array v2*. Three different investigations were carried out:

- Measurement of detector linearity with dose (MU);
- Measurement of uniform dose distributions;
- Measurements of patient plans.

To measure linearity and uniform dose distribution, the detector was aligned at isocenter by means of the in-room laser system, and a 2-cm buildup was placed on top of it (Figure 6.7-left). To perform patient plan verification and to reproduce the measurement conditions of the reference detector (MatriXX PT with DigiPhant), the depth of measurement was adjusted each time by adding layers of RW3 upstream of the detector or by inserting the range shifter (plastic block of 7-cm water-equivalent thickness) in the beam path (Figure 6.7-right). Measurements were all performed with a PBS-dedicated nozzle, with the gantry at 0°.

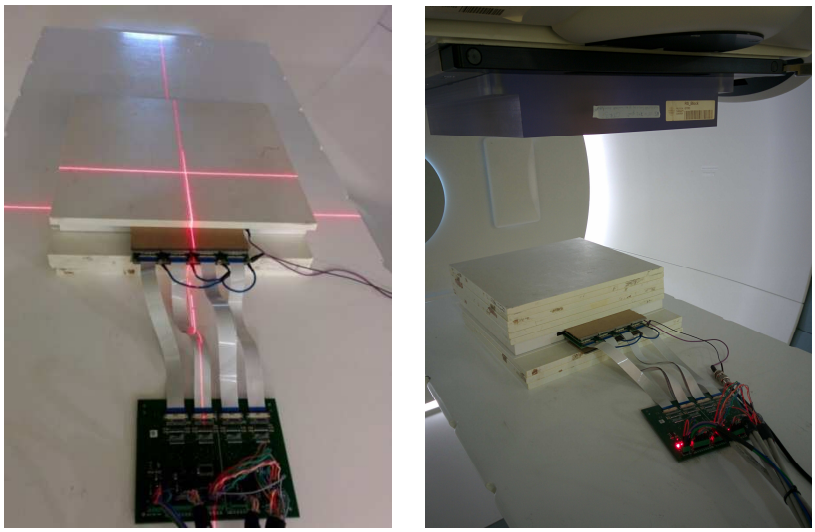

Figure 6.7. Setup of *detector array v3* on the patient positioning system, with a total of 2 cm water-equivalent buildup for linearity and beam profiling measurements (left) and with adjusted buildup and backscatter for patient plan measurements (right). In the picture on the right, one can also see the range shifter applied on the nozzle.

6.3.1 Linearity with MU

The *detector array v3* linearity with MU was assessed at three selected energies: 100, 165, and 226 MeV. Moreover, the number of monitor units delivered in each beam spot was changed in the range 0.02–12 MU/spot. For 0.02, 0.05, 0.1, and 0.25 MU/spot, measurements were repeated three times. A 10x10cm^2 field was irradiated, with spots arranged in a uniform map with 2 mm spacing.

Linearity was evaluated in terms of residuals from linear regression; results for the investigated energies are reported in Figure 6.8, Figure 6.9, and Figure 6.10.

The detector response at 100, 165, and 226 MeV is linear within ±1% for delivered dose per spot greater than 0.1 MU. Below this value, the detector showed significant deviations from linearity, especially in the lower and middle energy ranges (the same considerations of Paragraph 5.1.2 are valid here for reliability of the reference chamber). A maximum deviation from the linear regression of 6% was found for 0.02 MU/spot at 100 MeV proton energy. This limitation will be discussed in Section 6.4.

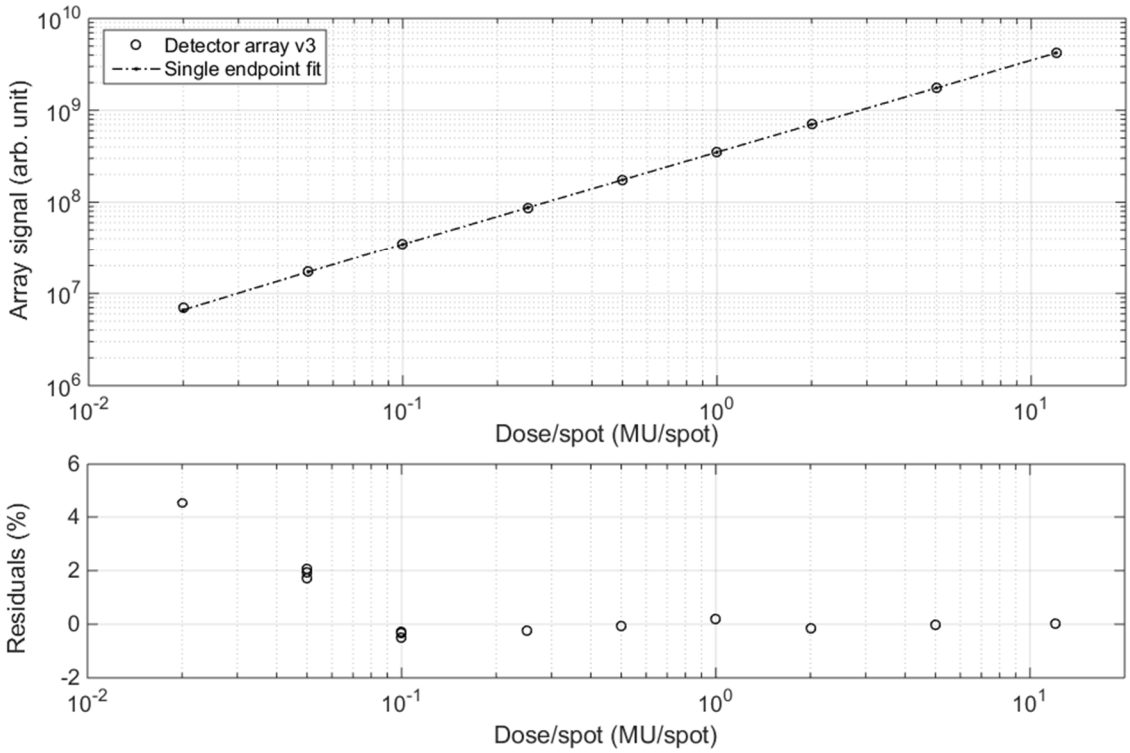

Figure 6.8. Integrated charge as a function of delivered dose for 100 MeV proton beam (top) and residuals from linear regression (bottom).

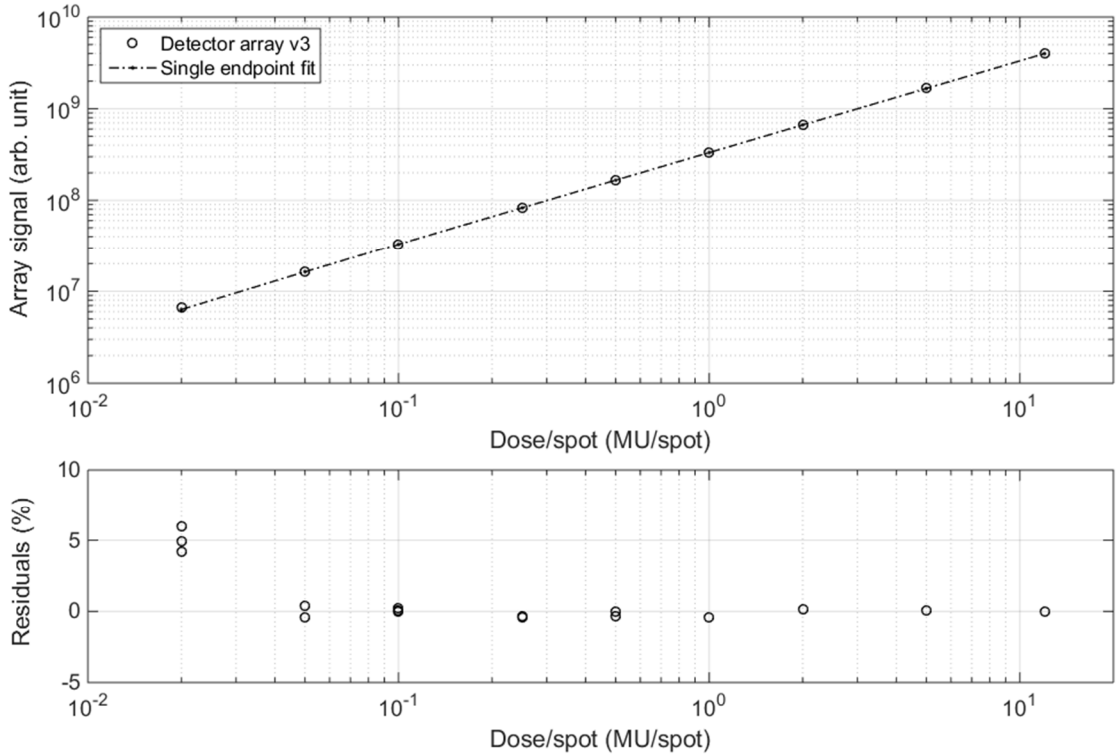

Figure 6.9. Integrated charge as a function of delivered dose for 165 MeV proton beam (top) and residuals from linear regression (bottom).

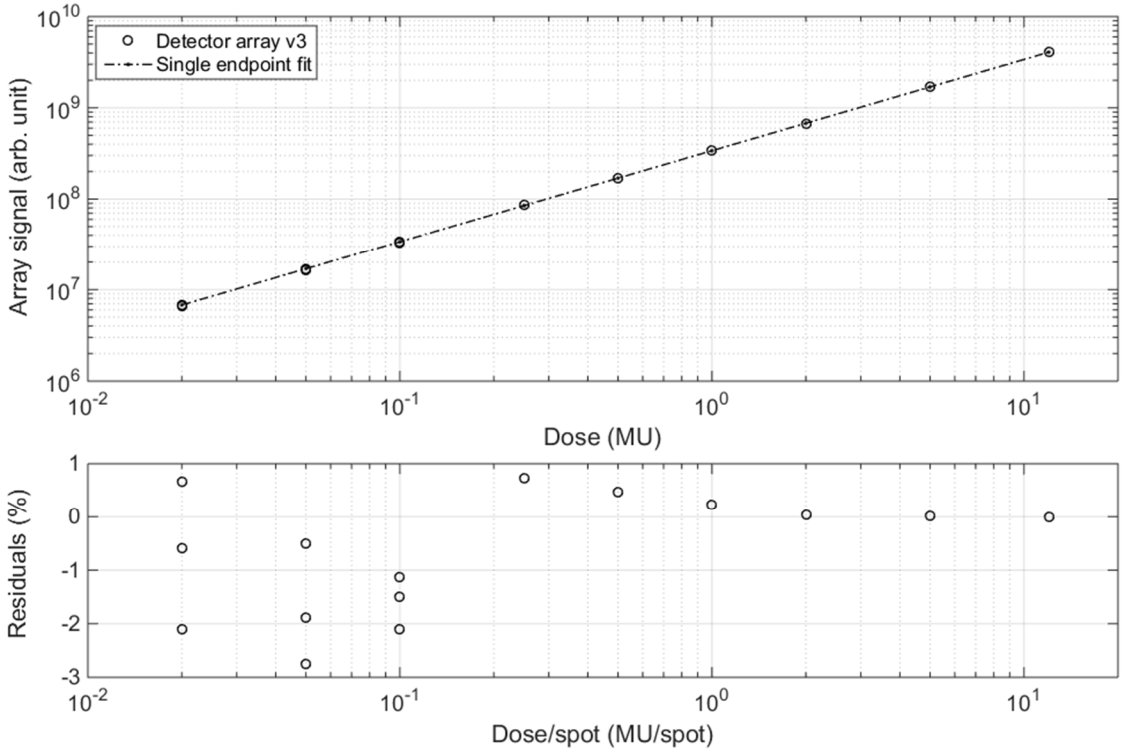

Figure 6.10. Integrated charge as a function of delivered dose for 226 MeV proton beam (top) and residuals from linear regression (bottom).

6.3.2 Measurements of uniform dose distribution

Uniform dose distributions with different sizes were delivered to *detector array v3*. The lateral size of the field was varied by changing the number of spots in each map. The beam settings were: 2 mm spacing between spots, 1 MU of dose delivered for each spot, and ~6 nA treatment current at 226 MeV proton energy. For example, a 10x10cm^2 dose distribution was delivered with a 51x51 spots map, resulting in a total delivered dose of 2601 MU. Following the same procedure described in Section 5.2.1, *detector array v3* was benchmarked against the Lynx as the reference detector. Few examples of raw data not corrected for uniformity are shown in Figure 6.11, and the inline axis is indicated in the bottom-right picture.

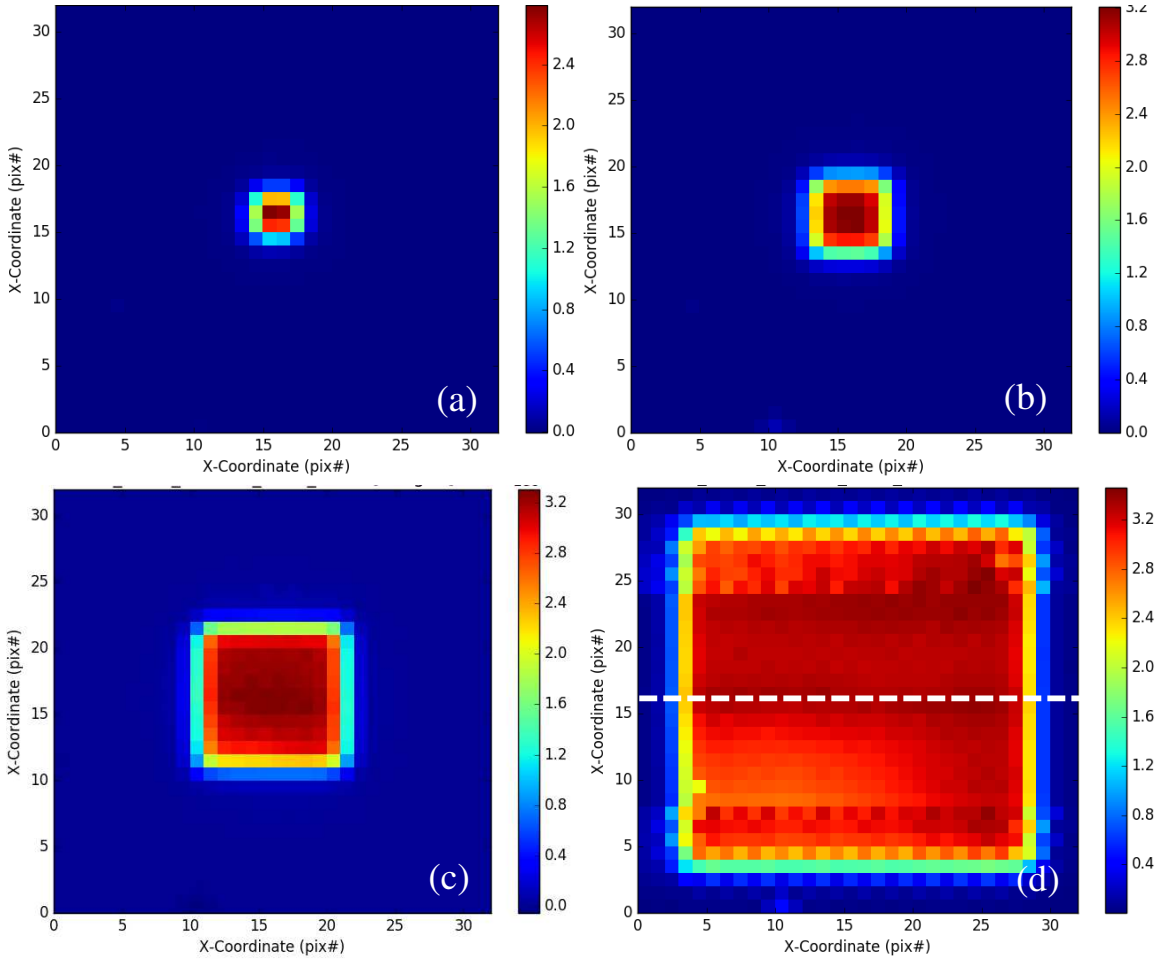

Figure 6.11. Raw measurements of 226 MeV proton maps delivered in PBS. Map sizes are: 1x1 cm^2 (a), 2x2 cm^2 (b), 4x4 cm^2 (c), 10x10 cm^2 (d). In (d), the inline axis along which the profiles are evaluated is indicated with a dashed white line.

Profiles measured along this axis are then normalized to a large field (12x12 cm^2). Figure 6.12 shows the inline dose distributions for six different field sizes, compared to the Lynx.

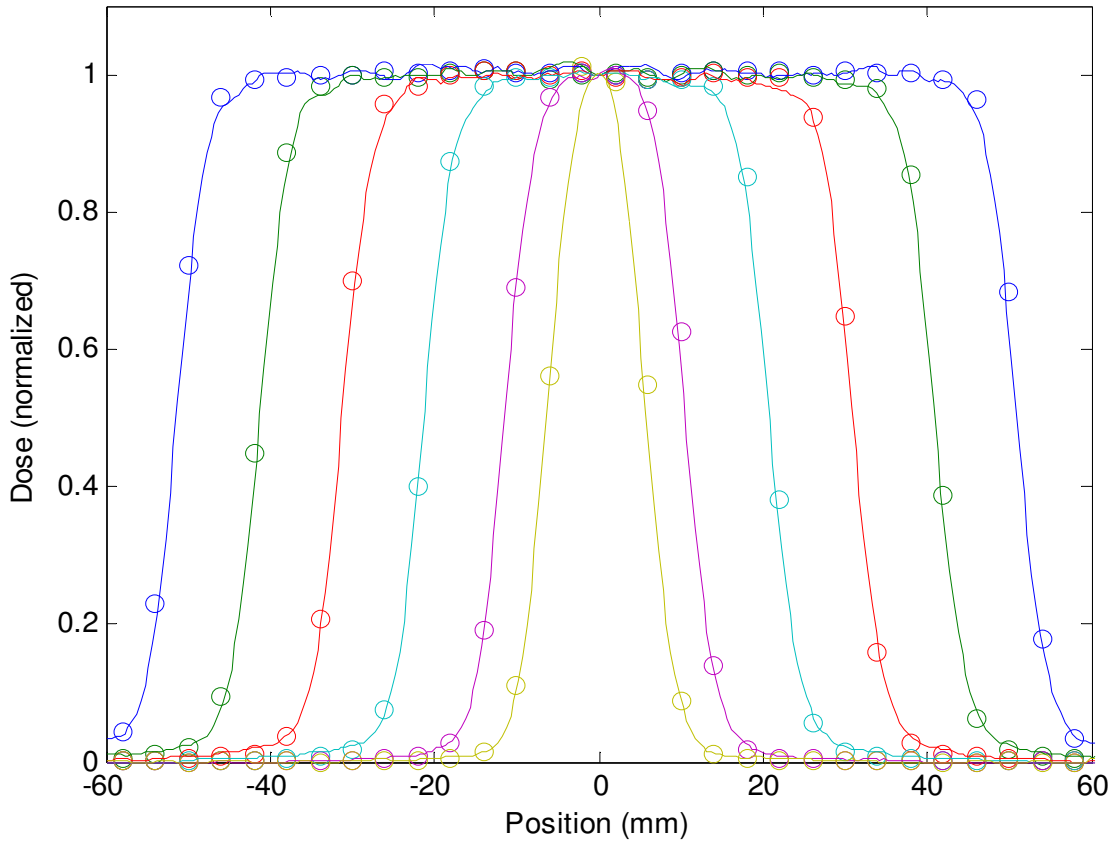

Figure 6.12. Dose distributions of 226 MeV proton maps delivered in PBS mode, normalized to central axis. Dimensions of delivered maps are: 1x1, 2x2, 4x4, 6x6, 8x8, and 10x10 cm^2. *Detector array v3* is represented with open markers, the Lynx with a continuous line.

6.3.3 Patient verification through comparison of 2D dose distributions

Preliminary tests of patient plan verification were performed with *detector array v3* for two selected IMPT treatments of brain tumors. The two cases were chosen because of the relative small size of the tumor (the size of the prototype active area is 12.4x12.4 cm^2, and it is thus especially suited to measuring small dose distributions).

IMPT plans characteristics are summarized in Table 6.1. The beams delivered to the target volume and the resulting isodose curves for Plan 1 and Plan 2 are shown in Figure 6.13 and Figure 6.14, respectively.

Table 6.1. Characteristics of the two IMPT-selected plans for patient QA measurements. For Plan 1, Beam #1 and Beam #2 show similar dose distributions. Therefore, only Beam #1 was measured.

	PLAN 1	PLAN 2
Clinical localization	Brain	Brain
Number of beams	2 (only beam #1 was measured)	1
Energy range (MeV)	116–164	130–160
Depth of measurement with *detector array v3* (cm)	7	7

TPS dose distributions were verified through a 2D gamma analysis (cf. Paragraph 1.2.2) with both *detector array v3* and the MatriXX PT. As described in Chapter 5, MatriXX PT in the DigiPhant water tank is typically used in the clinic to perform pre-treatment patient QA and was therefore taken as a reference for this evaluation. Criteria adopted for gamma analysis were: $\Delta D_M = 3\%$, $\Delta D_M = 3\ mm$.

The results of the patient plan evaluation are plotted in Figure 6.15 (Plan 1, Beam 1) and Figure 6.16 (Plan 2). The measured dose distributions are shown, together with the TPS-calculated dose at the chosen depth of measurement. In general, it can be clearly seen even from the 2D dose map that the spatial definition achieved with *detector array v3* is much higher than that of MatriXX PT thanks to the 4-mm pixel pitch.

For *detector array v3,* the gamma analysis shows a pass rate (i.e. the percentage of points with gamma index <1) of 98.5% and 98.9% for Plan 1 and Plan 2, respectively. Measured pass rates for the MatriXX PT are 99.6% and 99.8%. Correction factors for uniformity (calculated from the response of the detector to a uniform 14x14 cm^2 ^{60}Co beam) were applied to the *detector array v3* raw data.

The gamma analysis was performed without rescaling the dose grids but keeping the original resolution from the MatriXX PT and *detector array v3* measurements.

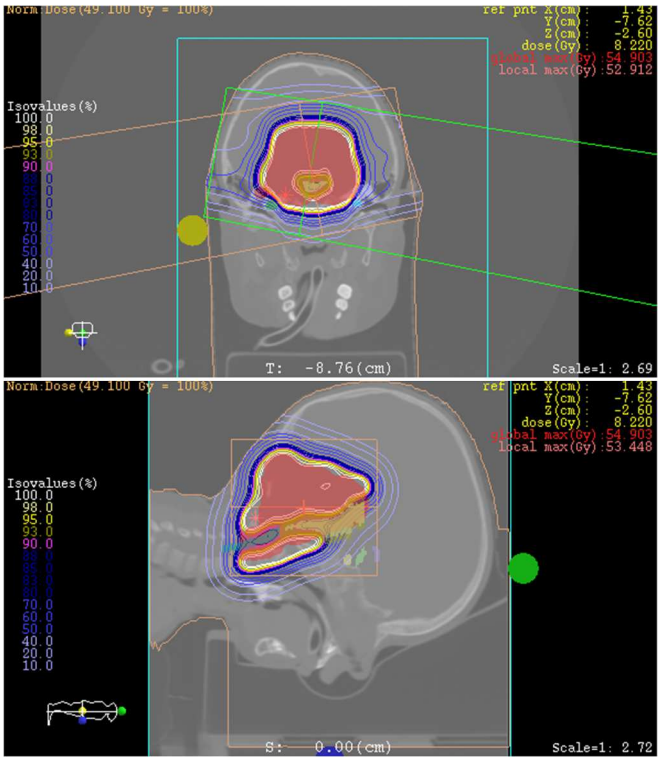

Figure 6.13. Images from XiO TPS that show the two beams applied to the patient CT and the resulting isodose curves for Plan 1.

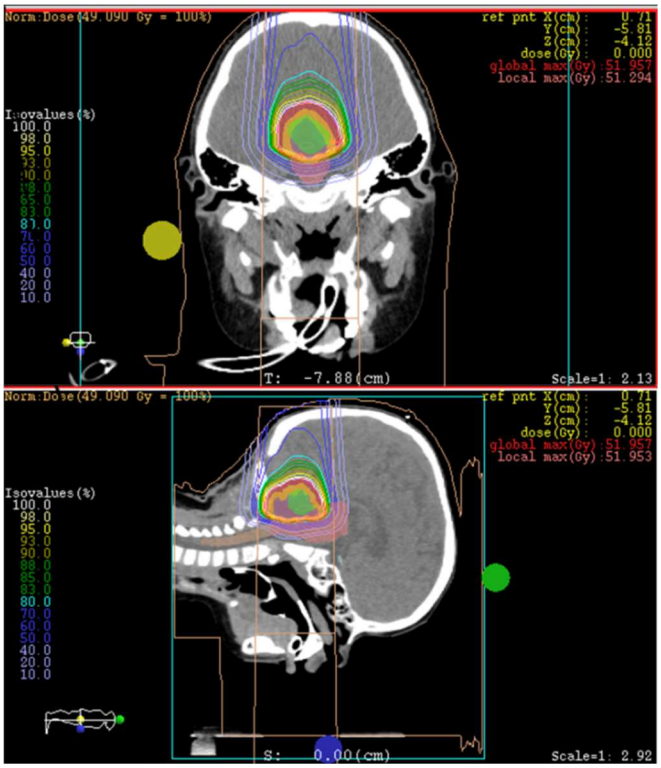

Figure 6.14. Images from XiO TPS which show the two beams applied to the patient CT and the resulting isodose curves for Plan 2.

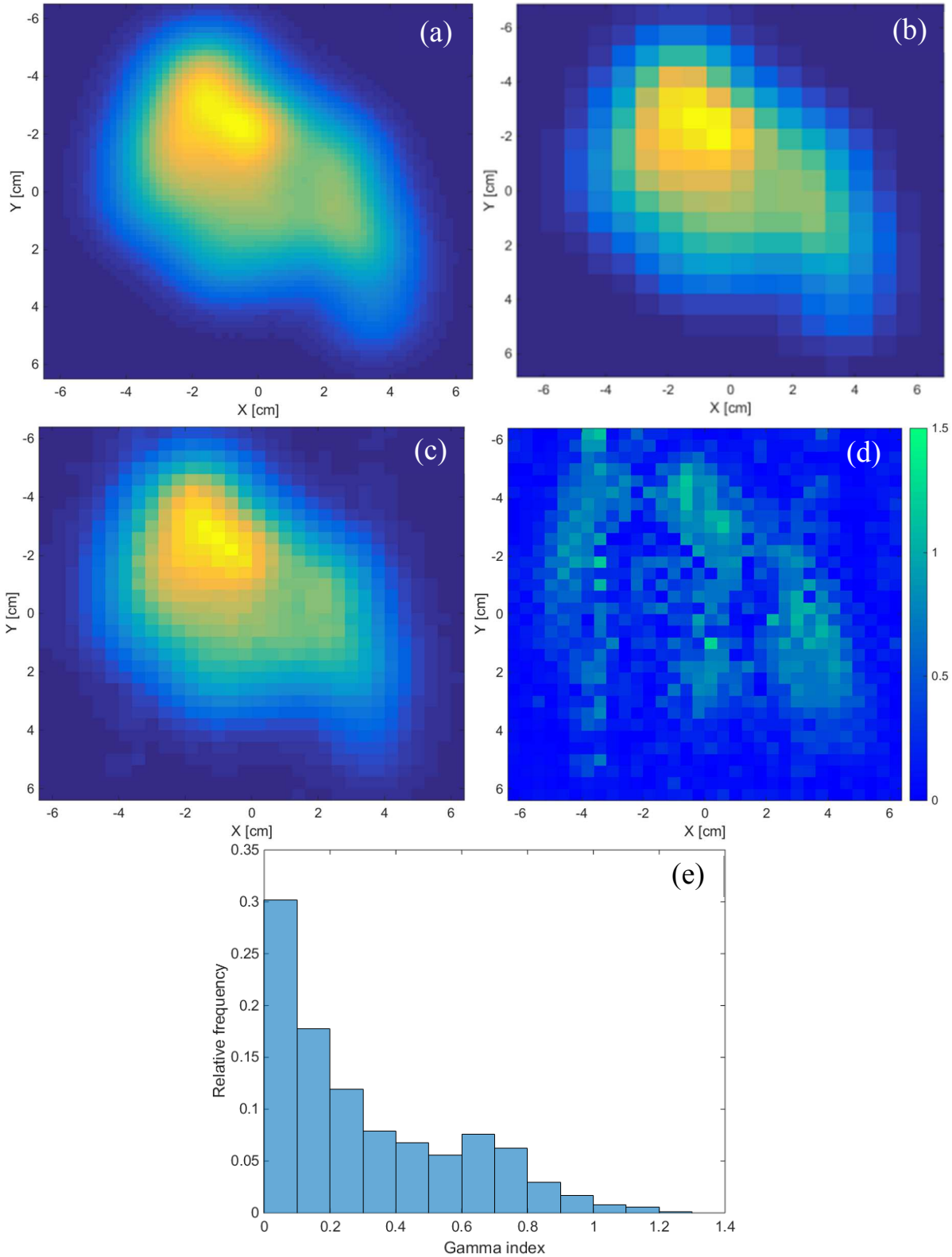

Figure 6.15. Plan 1 dose distributions: from TPS (a), measured with MatriXX PT (b), measured with *detector array v3* (c). Gamma analysis between TPS and *detector array v3* (d) shows a pass rate of 98.5%. A frequency histogram of gamma index is reported in (e).

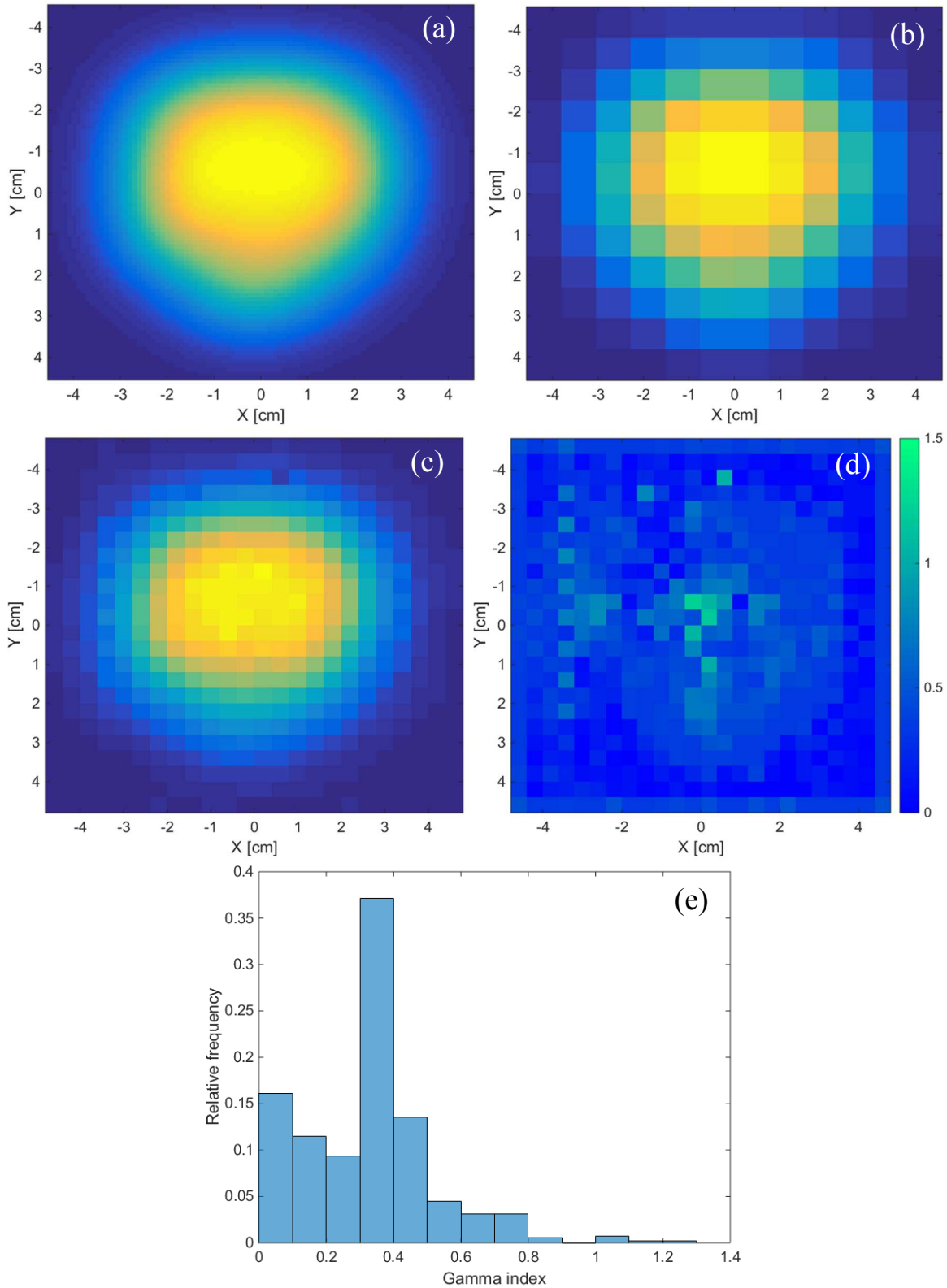

Figure 6.16. Plan 2 dose distributions: from TPS (a), measured with MatriXX PT (b), measured with *detector array v3* (c). Gamma analysis between TPS and *detector array v3* (d) shows a pass rate of 98.9%. A frequency histogram of gamma index is reported in (e).

6.4 DISCUSSION

Preliminary dosimetric characterization was performed for *detector array v3* in photon and proton beams. The ability of the prototype to accurately measure beam profiles was proven, and results were compared to reference detectors such as MatriXX^{Evolution} (MV X-rays) and Lynx (protons).

The detector response was proved to be linear with dose from PBS proton beams above 0.1MU/spot for all the energies. Below this value, linearity was still limited by noise and reproducibility issues, which are discussed in the following text.

Encouraging results were achieved in view of a possible application to patient QA in intensity-modulated proton therapy. Two selected patient plans were measured and verified with *detector array v3*, and results from gamma analysis were benchmarked to the reference system MatriXX PT+DigiPhant. Similar pass rates were found for the two measurement systems, but the definition of the dose map is much higher with *detector array v3* thanks to better spatial resolution.

A working 2D prototype was successfully built and tested. The new firmware associated with the frontend electronics and the readout scheme was demonstrated to be appropriate for such application. However, some aspects still require improvements. For instance, initial measurements suffer from poor repeatability and non-negligible levels of noise. An example is given in Figure 6.17, where six subsequent measurements of proton beam profiles (PBS maps) are shown. The data show a poor repeatability of the signal, and a non-negligible noise is furthermore superimposed on the measurements. The repeatability of the beam itself was checked with an independent measurement, and it was found to be in the order of 0.1–0.2%.

Noise and limited repeatability are responsible for deviations from linearity at low doses, as already pointed out throughout the presented results. Uniformity in crossline (transversal to the main axis of the electronic boards) direction (Figure 6.18) is moreover affected by the mechanical assembly of the detector modules. As a consequence, correction factors for uniformity were difficult to determine, as they are not constant in time and because deviations to be corrected in the crossline direction are large.

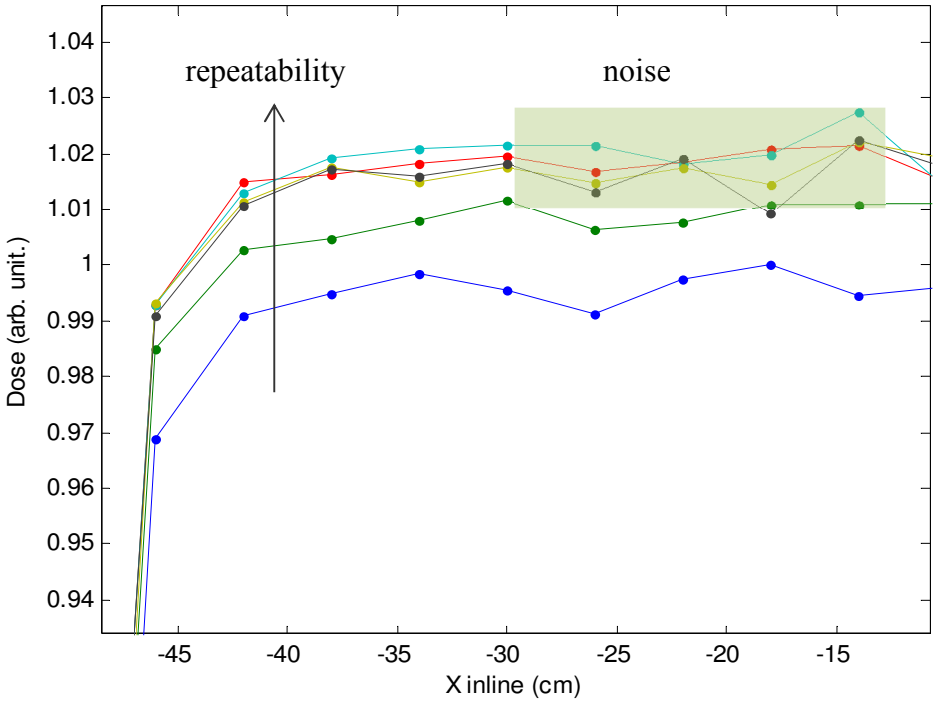

Figure 6.17. Raw data from subsequent measurements of beam profiles generated from PBS proton maps, 10x10 cm^2, 1 MU/spot.

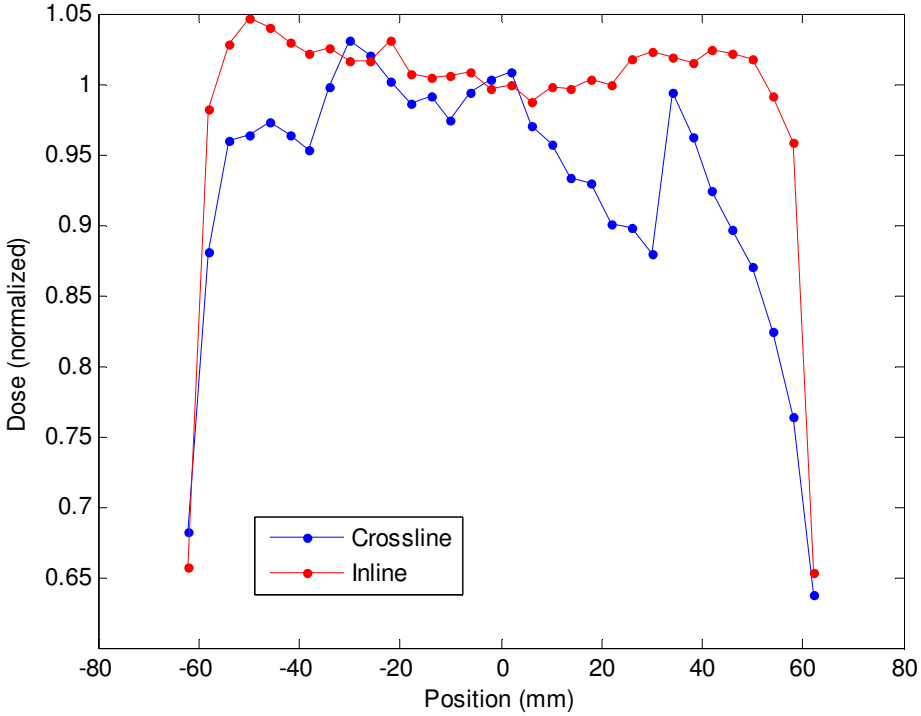

Figure 6.18. Crossline and inline profile of a proton PBS map. The poor uniformity of the crossline profile can be explained by low signal reproducibility and superimposed noise, as well as by poor mechanical assembly of detector modules.

To further improve signal repeatability and increase the signal to noise ratio, the guarding of the detector was improved and additional shielding (consisting of an aluminum foil connected to ground) from electromagnetic interferences (EMI) was adopted.

Figure 6.19 shows the signal noise density measured for different shielding and guard configurations. In former measurements, without additional shielding, a strong component of 50 Hz noise was superimposed to the signal and a high frequency noise contribution was measured. After the improvements against EMI, the noise density spectrum is close to a white spectrum, and the 50 Hz component completely disappeared.

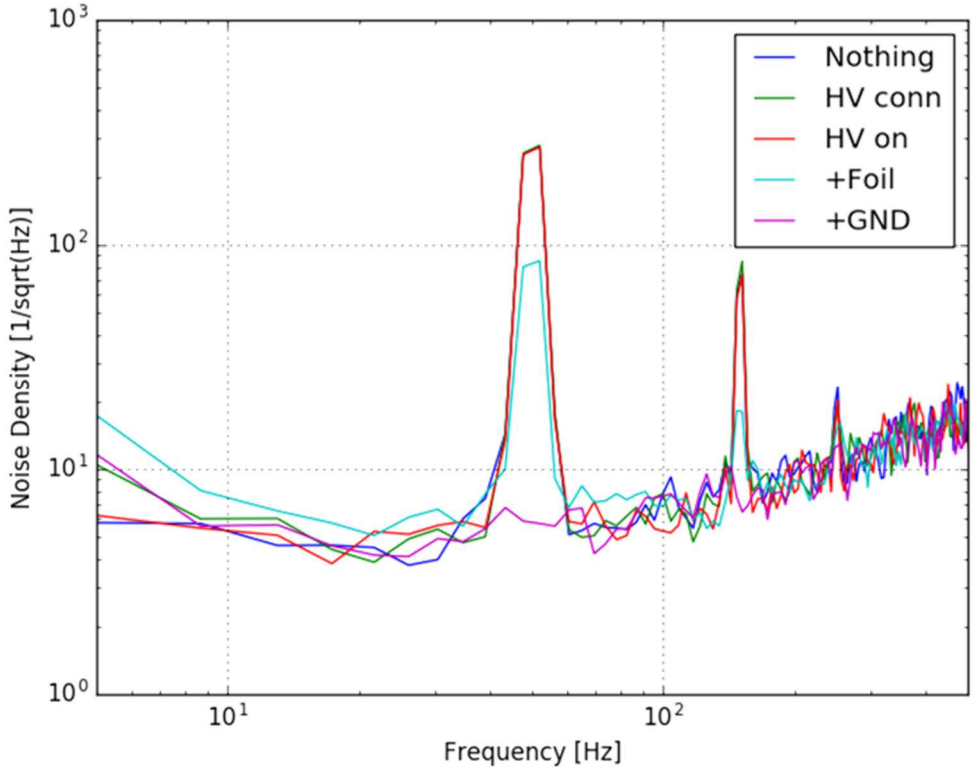

Figure 6.19. Noise density spectrum for different shielding configurations: without shielding, as in former measurements (blue, green and red lines), with shielding to EMI (light blue curve), and with grounded shielding (pink curve).

Moreover, after the upgraded guard connection, a better repeatability of the signal was achieved. For instance, the right graph in Figure 6.20 represents the repeatability evaluated as a standard deviation of 10 subsequent measurements of a 12x12 cm^2 ^{60}Co beam. Apart from some pixels outside the field region, the reproducibility is better than 0.4% over the complete sensitive area. An example of single acquisition of a 12x12 cm^2 ^{60}Co beam is shown in the

left graph of Figure 6.20. Despite the improved repeatability, *detector array v3* still shows a non-uniform response over the sensitive area.

The measured cobalt field, neither corrected for uniformity nor normalized to a larger field, presents deviations in uniformity of ±25%. Even though corrections can be applied, as explained above, such deviations are too large to be accepted in a commercial product and are a potential source of stability issues.

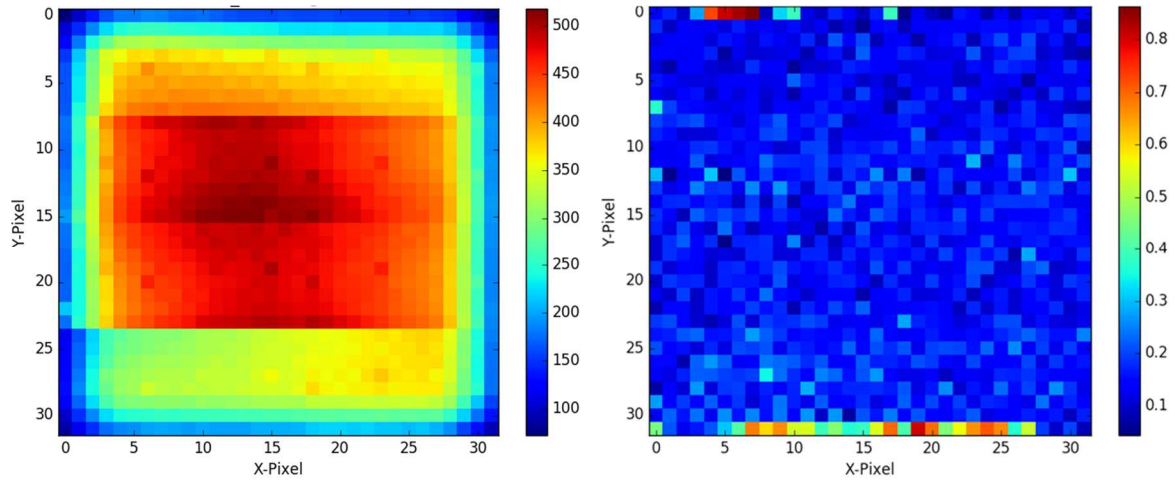

Figure 6.20. Example of raw measurement of 12x12 cm^2 cobalt beam (left, intensity in arbitrary unit). Different sensitivity regions can be linked to different detector modules, thus denoting a poor mechanical coupling of the modules. Chamber sensitivity is in fact proportional to chamber active volume. Despite non-uniform response, the detector shows a better repeatability after guard and shielding improvements (right, intensity in percentage of maximum value).

Different regions of sensitivity correspond to different base modules in *detector array v3*, and non-uniformity is probably related to a wrong module positioning (such as wrong parallelism between the electrode and a module, or misalignment between collecting electrodes on the PCB and cavities in the top electrode). Thus, the mechanical assembly of the different modules to create a single measuring device shall be improved further. By fixing the mechanical stability of the base modules, an improvement in both the repeatability and the uniformity of the detector response is expected.

Additional studies and a new hardware development (which is beyond the scope of this work) are therefore required in order to:

- complete the dosimetric characterization with both protons and MV photons by measuring the long-term stability and charge collection efficiency of the detector;
- build a detector with a larger sensitive area, comparable with general purpose plan-verification detectors (i.e. with a sensitive surface of at least 20x20 cm^2). The present size is already comparable to that of arrays for specific applications, such as patient QA for small-field IMRT and SRS/SBRT [69].

Chapter 7 CONCLUSIONS AND OUTLOOK

Nowadays, radiotherapy with external radiation beams is one of the most used practices to fight cancer, together with surgery and chemotherapy. Many cancer patients can benefit from radiation treatments with different types of radiations thanks to the high level of accuracy and precision achieved in radiation therapy techniques. In the coming years, the number of patients that could benefit from a radiation treatment is expected to increase as new treatment techniques, such as intensity-modulated proton therapy and stereotactic radiosurgery, allow for the treatment of complex clinical cases with improved outcomes. However, the complexity associated with these treatment techniques is increasing as well, thus requiring a continuous development of detectors dedicated to quality assurance purposes.

The aim of this thesis was to investigate the suitability of an innovative array technology to quality assurance applications in external beam radiotherapy. This study was motivated by the fact that modern radiation delivery techniques feature a high level of complexity and that therefore an accurate quality assurance is required to ensure the consistency of medical prescription to the patient. For instance, intensity-modulated radiation therapy and stereotactic radiosurgery with high-energy photons are characterized by dose distributions to the target with steep gradients, elevated dose rates and dose per single pulse, and time-varying parameters (e.g. dose rate, position of the gantry, dose). In particle therapy, additional challenges to quality assurance procedures were introduced with pencil beam scanning delivery techniques, where the dose is delivered to the tumor through several high-intensity narrow particle beams. Together with irradiation techniques, the complexity of machines used for radiation delivery has increased as well. Thus, machine routine controls shall be performed with high accuracy in order to ensure the reproducibility and reliability of the system.

Considering this, and taking into account the recommendations for quality assurance procedures from different international protocols, this thesis was dedicated to the development and characterization process of a technology based on ionization chambers. The main goal of the development was to achieve a higher spatial resolution than currently available devices that are based on the same sensor technology, as well as a low sensitivity on dose delivered per single radiation pulse. The choice of an ion chamber-based technology for dosimetric measurements relies on the fact that ionization chambers are widely considered the gold reference for such applications due to their low energy-dependence, high reproducibility, and the possibility of measuring absolute dose. A major challenge was to combine all the above-mentioned properties in the construction of 2D arrays, which are invaluable tools for QA purposes due to their versatility and ease of use.

Following the major steps of the technology characterization process, this thesis summarizes a three-year work which has been carried out at IBA Dosimetry GmbH in collaboration with three partner institutions: the Klinikum rechts der Isar (Munich, Germany), the University of California San Francisco (San Francisco, CA, US), and the Proton Therapy Center Czech s.r.o. (Prague, Czech Republic). To assess the technology's suitability to building detectors for dosimetric measurements, a first prototype was built at IBA based on the consolidated experience of the company in manufacturing such devices. An initial testing phase was performed at the IBA Secondary Standard Dosimetry Laboratory (SSDL DosLab) with a cobalt source, which provides an isotropic field of gamma radiation with a well-known energy, intensity, and dose rate. Cobalt radiation is typically used as a reference radiation in calibration procedures of dosimeters dedicated to radiation therapy.

The investigation focused mainly on the dynamic response of a single ionization chamber to delivered radiation. Thus, the integrated current from the chamber was monitored with different settings. Furthermore, a first attempt to measure a beam profile was made. This initial stage in the characterization of the detector was carried out by incrementally improving the design of the first 1D detector prototype (*detector array v1*), making assumptions which have been experimentally tested. The outcome was a list of "design rules" that led to a reproducible and stable ionization current. This achievement was essential in order to move forward and begin the conceptualization of a new prototype.

Detector array v2 was built based on the experience gained with the characterization of *detector array v1*. The main purposes behind the detector concept were:

- to consolidate the achievements reached with *detector array v1* and implement a 1D detector able to perform reproducible measurements;
- to introduce a new multi-channel low-noise front end electronics;
- to produce a device that can be used for independent tests in partner clinics.

The dosimetric characterization of *detector array v2* again started with the assessment of the dynamic response of each chamber under continuous gamma radiation. The excellent stability of the signal despite the small sensitive chamber's volume proved the effectiveness of the modifications introduced in the detector design. Once the reproducibility of the measurements was assessed, basic dosimetric properties such as linearity with dose, directional dependence of detector response, charge collection efficiency, and sensitivity dependence on dose per pulse were evaluated. After this characterization step, *detector array v2* provided performances reliable enough to be considered ready for extensive clinical tests.

Several measurement campaigns were carried out with clinical MV X-rays, performing both machine quality assurance controls and preliminary pre-treatment patient plan verifications.

The machine QA measurements consisted of:

- tissue to phantom ratio (TPR) – the *detector array v2* has been benchmarked to a compact ionization chamber;
- output factors – the array has been benchmarked to a compact ionization chamber for field sizes greater than 5x5 cm^2 and to a stereotactic diode for field sizes of less than 5x5 cm^2;
- beam profiling at different beam quality – the array has been compared to a commercial ionization chamber array, to a silicon flat panel, and to Gafchromic® films (because of their superior spatial resolution) in the case of a 1x1 cm^2 irradiation field.

The suitability of the array for use in patient QA was assessed through comparison of measured linear dose distributions with the TPS for different clinical localizations. The detector has also been benchmarked to Gafchromic® films for two specific cases:

- a VMAT lung irradiation;

- an SRS head tumor irradiation.

Once the characterization with clinical photons was competed, an extensive measurement campaign was carried out with clinical proton beams. This involved performing basic dosimetric evaluation, machine QA tests, and preliminary patient QA measurements. Detector linearity with dose and dose rate was evaluated over the whole clinical range of dose and proton current. The charge collection efficiency was evaluated with the highest reachable dose rate. Two machine QA checks were performed:

- beam profiling – *detector array v2* has been compared to a commercial ionization chamber array and benchmarked to a scintillating based detector;
- pristine Bragg peak distributions – the detector has been benchmarked to a commercial ionization chamber inserted into a water tank for range verification measurements.

Pre-treatment patient plan verification measurements were performed for a prostate case irradiated with two beams in pencil beam scanning mode. They were then compared with both the TPS and a commercial ionization chamber array.

Once *detector array v2* was fully tested with both high-energy photons and particles, the technology under investigation was extended to a 2D device with the design of *detector array v3*. This detector is innovative in both its assembly and its readout system. The proof of concept has been started with preliminary validation in clinical proton beams, providing the basis for the upcoming complete characterization of the device.

At the end of this work, the technical feasibility of this innovative technology based on ionization chambers and designed for radiotherapy application is proved. The design of the chambers and the assembly of the detector guarantee an excellent time stability of ionization current despite the 4 mm^3 sensitive volume.

The detector's long-term stability (0.5%) and reproducibility (0.3%) are those typical of ionization chambers. Deviations from dose linearity are below 1.0% for doses higher than 20 cGy and no larger than 1.5% down to 5 cGy. With *detector array* v2, the dose linearity was limited by the performance of the readout electronics, which was suboptimal for

measurements at low doses with small chambers. An improved version of the acquisition system has been implemented in *detector array v3*. The measured charge collection efficiency of the ion chamber technology at 2.7 mGy/pulse is 99.5 % ±0.3%, which is achieved with a bias of 250 V (maximum bias applicable is 500 V). The fact that almost full charge collection efficiency can be reached at any dose per pulse determines a low dose per pulse dependence of detector's sensitivity, which is better than 0.3% in the range 0.1–1.0 mGy per pulse and never exceeds 0.9% up to 2.7 mGy per pulse.

The technology shows similar performances in PBS proton beams. Linearity is within 1.1% over the whole range of clinical energy and dose rate. Charge collection efficiency is already higher than 99% at 100 V, reaching 99.7 % ±0.3% at 250 V.

All the mentioned properties, together with the small distance between pixels and a directional dependence that is consistent with other commercial detectors based on ionization chambers, make this technology suitable to building detectors designed for machine QA and patient plan verification in high-energy photon beams and PBS proton beams.

Depth dose curves can be measured with good agreement to reference detectors. In particular, the range of pristine Bragg peak distributions can in principle be determined with a single irradiation and with a sub-millimeter precision. This property is valuable for routine controls such as those typically adopted in clinics for daily range verification.

Beam profiles (and spot maps in the case of protons) can be reconstructed with high accuracy and in a fast mode for different beam sizes and energies. *Detector array v2* exhibits the capability to measure profiles of even 1x1 cm^2, with maximum deviations from reference (Gafchromic® films) that are comparable to those between the reference and an amorphous silicon flat panel. The ability to measure narrow dose distributions and accurately define penumbra regions is essential in modern radiotherapy treatments such as IMRT and SBRT/SRS.

A limitation of the present technology configuration is the underestimation of LINACs output factors for large fields (4% deviation with 25x25 cm^2 beam size). Although a possible explanation of the phenomenon has been postulated, the problem is currently not completely understood. A more detailed investigation of the phenomenon with Monte Carlo simulations

has been started. Although it is possible to employ correction factors to compensate field size dependence, these effects shall firstly be minimized by optimizing detector design.

Even though some issues still need to be addressed, from the outcomes of this assessment, it can be concluded that a detector array based on the investigated technology is a valuable device for machine QA controls, with performances that are comparable or higher than those of detectors typically used in clinics. Furthermore, it represents a versatile, fast, and easy-to-use tool.

The results from preliminary measurements of patient QA show a general agreement with benchmarks (typically Gafchromic® films) and enhanced performances compared to other commercial detectors when the dose rate is elevated and the target is covered by highly modulated dose distribution. This can be observed from the performed evaluation of two specific cases with MV X-rays and one intensity-modulated treatment with proton beams.

These encouraging results allow this thesis to conclude that, thanks to the high spatial resolution and the insensitivity on dose delivered per pulse, the technology is optimal for patient QA of VMAT, SBRT/SRS, and IMPT treatments. This assessment has been confirmed and extended by the partner institutions during the above-mentioned experimental campaign and the complete characterization process. Although the evaluation of *detector array v2* for patient QA shows that the technology is very promising for such application, it is clear that a 2D detector is essential.

Preliminary evaluations with *detector array v3* confirm the potentiality of the technology. Basic dosimetric properties have been checked under clinical proton beams. An initial 2D gamma analysis was also performed on a measured IMPT plan and compared with TPS and a commercial detector. Results of the gamma analysis exhibit a pass-rate comparable to the one from the reference system, but the dose distribution is better defined in terms of spatial definition. Further investigations were performed to address a few aspects which need improvements, and will continue in a future work.

The complete work has been carried out in the framework of the ARDENT project, which is a European scientific collaboration on advanced radiation dosimetry that was founded by the Marie Curie Project. The results of the characterizations described above have been presented at various major international conferences and congresses, such as AAPM,

ESTRO, PTCOG and MMND-ITRO. Additionally, a manuscript has been published in the Medical Physics journal.

At the end of the assessment process, the author is firmly convinced that the technology has great potential for applications in radiation dosimetry. Its features were thought to address the requirements of modern radiotherapy techniques and to simultaneously fulfill the recommendations of international dosimetric protocols. The outlook for such a technology application in clinical devices can be viewed by tracing the history of its development. Even though the achievements described in this work are remarkable, further improvements and investigations are needed. In particular, three main research branches are here identified.

- The study of the underestimation of signal for large field sizes compared to a single thimble ionization chamber. The hypothesis which has been proposed is that the amount of lateral scattering of radiation in a volume with many air cavities at short distance is smaller than in a homogeneous volume without cavities. Therefore, the collected signal is lower. Other possible explanations which have been found in literature seem to not be realistic, considering the geometry and the materials of the detector.

  The author is also convinced that the problem can be well-investigated through Monte Carlo simulations. As discussed in this thesis, the geometry of the detector has already been implemented in EGSnrc in order to evaluate the detector sensitivity to scattered radiation and field size. However, the Monte Carlo detector model and the simulation conditions need to be further refined to obtain reliable results.

- The assessment of feasibility of a modular-array concept, implemented for the first time with *detector array v3*. Preliminary results of 2D measurements of uniform dose distributions and patient plan with proton beams illustrate the capability of the technology to reconstruct the dose with accuracy and high resolution. Nevertheless, some issues related to the mechanical stability of the detector are not completely solved, thus affecting the measurement reproducibility. New mechanical solutions are already under evaluation to address these matters, and it is likely that they will be implemented shortly. Once this issue is fixed and the concept of modular-array is

proven to be feasible, the technology will acquire even more versatility. For instance, one can think about building 3D detectors by covering a cylindrical phantom with several modules, or making patient-specific QA with different modules inserted into a 3D-printed and CT-based patient phantom.

- The evaluation of the performances of the technology in high-intensity pulsed proton beams, such as those produced by the new S250i accelerator (MEVION Medical Systems, Littleton, MA US) or by the new super-synchrocyclotron S2C2 (IBA Particle Therapy, Louvain la Neuve, Belgium). Such beams feature a pulse frequency of about 1 kHz and values of charge per pulse in clinical delivery of up to 5 pC. In these conditions, the main challenge for a gas detector is the ion recombination rate within the sensitive volume. Commercial arrays such as the MatriXX PT (IBA Dosimetry GmbH, Schwarzenbruck, Germany) have been proven to undergo noticeable recombination with S2C2 beams. With the technology under investigation, the author is confident of keeping ion recombination within clinical recommendation even in such beams, due to the small inter-electrode distance and the possibility to increase the bias up to 500 V.

Bibliography

[1] International Agency for Research on Cancer, World cancer factsheet (2012).

[2] R. Twombly, “Cancer surpasses heart disease as leading cause of death for all but the very elderly”, J. Natl. Cancer I., 97(5):330–331, 2005.

[3] P. Boyle and B. E. Levin (editors), IARC, World Cancer Report, 2008, Lyon.

[4] B. W. Stewart and C. P. Wild (editors), IARC, World Cancer Report, 2014, Lyon.

[5] American Cancer Society, Cancer Facts & Figures 2012, Atlanta, GA, 2012.

[6] American Medical Association, Physician Characteristics and Distribution in the United States, Atlanta, GA, 2008.

[7] M. Zaider and L. Hanin, “Tumor control probability in radiation treatment”, Med. Phys., 38(2):574–583, 2011.

[8] E. Hall and A. Giaccia, Radiobiology For The Radiologist, Lippincott Williams & Wilkins, 6th edition, 2006.

[9] P. Mayles, A. Nahum and J. C. Rosenwald, Handbook of Radiotherapy Physics: Theory and Practice, Taylor & Francis Group, 2007.

[10] E. B. Podgorsak, Radiation Oncology Physics: A Handbook for Teachers and Students, IAEA, 2005.

[11] H. Paganetti, T. Bortfeld and H. Kooy, “Proton Beam Radiotherapy – The State of the Art”, Med. Phys., 32, 2048 (2005).

[12] N. Sheets, G. Goldin, A.-M. Meyer, Y. Wu, Y. Chang, T. Stürmer, J. Holmes, B. Reeve, P. Godley, W. Carpenter, and R. Chen, “Intensity-modulated radiation

therapy, proton therapy, or conformal radiation therapy and morbidity and disease control in localized prostate cancer", JAMA-J, Am. Med. Assoc., 307(15):1611–1620, 2012.

[13] A. Brahme, "Optimization of stationary and moving beam radiation therapy techniques", Radiother.Oncol., 12(2):129–40, 1988.

[14] T. Bortfeld, "IMRT: a review and preview", Phys. Med. Biol., 51, 2006.

[15] C. Yu and G. Tang, "Intensity-modulated arc therapy: principles, technologies and clinical implementation", Phys. Med. Biol., 56(5):31–54, 2011.

[16] F. Deodato, S. Cilla, G. Macchia, G. Torre, L. Caravatta, G. Mariano, S. Mignogna, M. Ferro, G. C. Mattiucci, M. Balducci, V. Frascino, A. Piermattei, G. Ferrandina, V. Valentini and A.G. Morganti, "Stereotactic radiosurgery (SRS) with volumetric modulated arc therapy (VMAT): interim results of a multi-arm phase I trial (DESTROY-2)", Clin. Oncol., 26(12):748-56, 2004.

[17] A. Lomax, "Intensity modulation methods for proton radiotherapy", Phys. Med. Biol., 44(1):185–205, 1999.

[18] ICRU Report 24, "Determination of absorbed dose in a patient irradiated by beams of X or gamma rays in radiotherapy procedures", International Commission on Radiation Units and Measurement, 1976.

[19] E. E. Klein, J. Hanley, J. Bayouth, F.-F. Yin, W. Simon, S. Dresser, C. Serago, F. Aguirre, L. Ma, B. Arjomandy, C. Liu, C. Sandin and T. Holmes, "Task Group 142 report: Quality assurance of medical accelerators", Med. Phys., 36(9), 2009.

[20] B. Arjomandy, E. Klein, P. Taylor, C. Ainsley, S. Safai, N. Sahoo, M. Pankuch, S. Park, J. Farr, Y. Kase, J. Flanz, E. Yorke and D. Followill, "SU-E-T-649: Quality assurance for Proton Therapy Delivery Equipment", Med. Phys., 42:3485, 2015.

[21] ICRU Report 78, "Prescribing, recording and reporting proton beam therapy", International Commission on Radiation Units and Measurement, 2007.

[22] G. J. Kutcher, L. Coia, M. Gillin, W. F. Hanson, S. Leibel, R. J. Morton, J. R. Palta, J. A. Purdy, L. E. Reinstein, G. K. Svensson, M. Weller and L. Wingfield, "Task Group 40 report: Comprehensive QA for radiation oncology", Med. Phys., 21(4), 1994.

[23] B. Arjomandy, N. Sahoo, X. R. Zhu, J. R. Zullo, R. Y. Wu, M. Zhu, X. Ding, C. Martin, G. Ciangaru and M. T. Gillin, "An overview of the comprehensive proton therapy machine quality assurance procedures implemented at The University of Texas M. D. Anderson Cancer Center Proton Therapy Center–Houston", Med. Phys., 36(6):2269-82, 2009.

[24] E. van der Wal, T.W.M. Grimbergen, J. de Pooter, J. M. J. Hermans, A. van der Plaetsen, A. Spilt, F. W. Wittkämper, D. Zweers, A. A. Lammertsma, P. Sminia and K. Franken, "Code of Practice for the Quality Assurance and Control for Intensity-Modulated Radiotherapy", Netherlands Commission on Radiation Dosimetry, Report 22, 2013.

[25] D. A. Low, W. B. Harms, S. Mutic and J. A. Purdy, "A technique for the quantitative evaluation of dose distributions", Med. Phys., 25(5):656-61, 1998.

[26] C. Wu, K. E. Hosier, K. E. Beck, M. B. Radevic, J. Lehmann, H. H. Zhang, A. Kroner, S. C. Dutton, S. A. Rosenthal, J. K. Bareng, M. D. Logsdon and D. R. Asche, "On using 3D γ-analysis for IMRT and VMAT pretreatment plan QA", Med. Phys, 39(6), 3051-9, 2012.

[27] K. B. Pulliam, J. Y. Huang, R. M. Howell and D. Followill, "Comparison of 2D and 3D gamma analysis", Med. Phys., 41(2): 021710, 2014.

[28] ICRU Report 33, "Radiation Quantities and Units", International Commission on Radiation Units and Measurement, 1980.

[29] J. T. Lyman, M. Awschalom, P. Berardo, H. Bicchsel, G. T. Y. Chen, J. Dicello, P. Fessenden, M. Goitein, G. Lam, J. C. McDonald, A. Ft. Smith, R. Ten Haken, L. Verhey and S. Zink, "Task Group 20 report: Protocol for heavy charged-particle therapy beam dosimetry", Med. Phys., AAPM Report No 016, 1986.

[30] W. H. Bragg, “Consequences of the corpuscular hypothesis of the gamma and x rays, and the ranges of beta rays”, Phil. Mag., 20:385, 1910.

[31] L. H. Gray, “Absorption of penetrating radiation”, Proc. Roy. Soc., A122:647, 1929.

[32] L. H. Gray, “Ionization method for the absolute measurement of gamma-ray energy”, Proc. Roy. Soc., A156:578, 1936.

[33] IEC 60731, “Medical electrical equipment – dosimeters with ionization chambers as used in radiotherapy”, edition 3.0, 2011.

[34] F. H. Attix, “Introduction to Radiological Physics and Radiation Dosimetry”, John Wiley & Sons, 1986.

[35] S. Russo, D. Boi, A. Mirandola, S. Molinelli, A. Mairani, E. Mastella, G. Magro, S. Giordanengo and M. Ciocca, “Dosimetric characterization of a commercial 2-D scintillation detector for quality assurance tests in scanned proton and carbon ion beams”, Physica Medica, 3:199, 2016.

[36] F. M. Khan, “The Physics of Radiation Therapy”, Lippincott Williams & Williams, 3rd ed., 2003.

[37] H. Condé, W. Cross, A. Deruytter, A. Ferguson, S. Kapoor, H. Lemmel, A. Lorenz, A. Michaudon, J. Schmidt, A. Smith and G. Yankov, “Absorbed Dose Determination in Photon and Electron Beams: An International Code of Practice”, IAEA TRS-227, 1987.

[38] P. Andreo, P. R. Almond, O. Mattsson, A. E. Nahum and M. Roos, “The Use of Plane Parallel Ionization Chambers in High Energy Electron and Photon Beams: An International Code of Practice for Dosimetry”, IAEA TRS-381, 1997.

[39] P. Andreo, D. T. Burns, K. Hohlfeld, M. S. Huq, T. Kanai, F. Laitano, V. Smyth and S. Vynckier, “Absorbed Dose Determination in External Beam Radiotherapy: An International Code of Practice for Dosimetry based on Standards of Absorbed Dose to Water”, IAEA TRS-398, 2000.

[40] P. R. Almond, P. J. Biggs, B. M. Coursey, W. F. Hanson, M. S. Huq, R. Nath and D. W. O. Rogers, “Task Group 51 report: AAPM’s TG-51 protocol for clinical reference dosimetry of high-energy photon and electron beams”, Med. Phys., 26:1847, 1999.

[41] J. W. Boag, “The Saturation Curve for Ionization Measurements in Pulsed Radiation Beams,” Br. J. Radiol., 25: 649–650, 1952.

[42] ICRU report 34, “The dosimetry of pulsed radiation”, International Commission on Radiation Units and Measurement, 1984.

[43] E. Yorke, R. Alecu, L. Ding, D. Fontenla, A. Kalend, D. Kaurin, M. E. Masterson-McGary, G. Marinello, T. Matzen, A. Saini, J. Shi, W. Simon, T. C. Zhu and X. R. Zhu, “Task Group 62 report: Diode in vico dosimetry for patient receiving external beam radiation therapy”, Med. Phys., AAPM report No. 87, 2005.

[44] H. Bouchard, F. Lacroix, G. Beaudoin, J. F. Carrier and I Kawrakow, “On the characterization and uncertainty analysis of radiochromic film dosimetry”, Med. Phys., 36(6):1931-46, 2009.

[45] L. J. van Battum, D. Hoffmans, H. Piersma and S. Heukelom, “Accurate dosimetry with GafChromic™ EBT film of a 6 MV photon beam in water: What level is achievable?”, Med. Phys., 35:704, 2008.

[46] G. S. Ibbott, “Applications of Gel Dosimetry”, J. Phys.: Conf. Ser., 3:58, 2004.

[47] S. Babic, A. McNiven, J. Battista and K. Jordan, “Three-dimensional dosimetry of small megavoltage radiation fields using radiochromic gels and optical CT scanning”, Phys. Med. Biol., 54(8):2463-81, 2009.

[48] L. Zhao and I. J. Das, “Gafchromic EBT film dosimetry in proton beams”, Phys. Med. Biol., 55:291-301, 2010.

[49] A. L. Palmer, A. Dimitriadis, A. Nisbet and C. H. Clark, “Evaluation of Gafchromic EBT-XD film, with comparison to EBT3 film, and application in high dose radiotherapy verification”, Phys. Med. Biol., 60:8741-8752, 2015.

[50] C. Baldock, Y. De Deene, S. Doran, G. Ibbott, A. Jirasek, M. Lepage, K. B. McAuley, M. Oldham and L. J. Schreiner, "Polymer gel dosimetry", Phys. Med. Biol., 55(5):1-63, 2010.

[51] J. Adamovicsand and M. J. Maryanski, "Characterisation of PRESAGE: a new 3-D radiochromic solid polymer dosemeter for ionising radiation", Radiat. Prot. Dosim., 120:107-12, 2006.

[52] D. Letourneau, M. Gulam, D. Yan, M. Oldham and J. W. Wong, "Evaluation of a 2D diode array for IMRT quality assurance", Radiother. Oncol., 70(2):199-206, 2004.

[53] J. Herzen, M. Todorovic, F. Cremers, V. Platz, D. Albers, A. Bartels and R. Schmidt, "Dosimetric evaluation of a 2D pixel ionization chamber for implementation in clinical routine", Phys. Med. Biol., 52(4):1197-1208, 2007.

[54] T. S. Stelljes, A. Harmeyer, J. Reuter, H. K. Looe, N. Chofor, D. Harder and B. Poppe, "Dosimetric characteristics of the novel 2D ionization chamber array OCTAVIUS Detector 1500", Med. Phys., 42(4):1528-37, 2015.

[55] B. Poppe, A. Blechschmidt, A. Djouguela, R. Kollhoff, A. Rubach, K. C. Willborn and D. Harder, "Two-dimensional ionization chamber arrays for IMRT plan verification", Med. Phys., 33(4):1005-1015, 2006.

[56] J. G. Li, G. Yan and C. Liu, "Comparison of two commercial detector arrays for IMRT quality assurance", J. Appl. Clin. Med. Phys., 10(2):62-74, 2009.

[57] P. A. Jursinic, R. Sharma and J. Reuter, "MapCHECK used for rotational IMRT measurements: Step-and-shoot, Tomotherapy, RapidArc", Med. Phys., 37(6):2837-2846, 2010.

[58] A. Van Esch, K. Basta, M. Evrard, M. Ghislain, F. Sergent and D. P. Huyskens, "The Octavius1500 2D ion chamber array and its associated phantoms: dosimetric characterization of a new prototype", Med. Phys., 41(9):091708, 2014.

[59] A. Magnelli, L. Bloe, S. Gajdos and T. Djemil, "SU-FF-T-215: Evaluation of a Planar Ion Chamber array for Patient Specific IMRT QA", Med. Phys., 36(6):2750, 2009.

[60] B. Poppe, H. Looe, A. Ruehmann, D Harder and K. Willborn, “SU-GG-T-144: IMRT Pre-Treatment Plan and In-Vivo Verification with 2D-ARRAYs and Multi-Wire Ionisation Chambers”, Med. Phys., 35:2759, 2008.

[61] M. K. Islam, B. D. Norrlinger, J. R. Smale, R. K. Heaton, D. Galbraith, C. Fan and D. A. Jaffray, “An integral quality monitoring system for real-time verification of intensity modulated radiation therapy”, Med. Phys., 36(12):5420-8, 2009.

[62] J. Thoelking, J. Fleckenstein, Y. Sekar, R. Boggula, F. Lohr, F. Wenz and H. Wertz, “Patient-specific online dose verification based on transmission detector measurements”, Radiother. Oncol., 119(2):351-6, 2016.

[63] D. Hoffman, E. Chung, C. Hess, R. Stern and S. Benedict, “SU-E-T-571: Newly Emerging Integrated Transmission Detector Systems Provide Online Quality Assurance of External Beam Radiation Therapy”, Med. Phys., 42:3467, 2015.

[64] T. Eckhause, H. Al-Hallaq, T. Ritter, J. DeMarco, K. Farrey, T. Pawlicki, G.Y. Kim, R. Popple, V. Sharma, M. Perez, S.Y. Park, J. T. Booth, R. Thorwarth and J. M. Moran, “Automating linear accelerator quality assurance”, Med. Phys., 42(10):6074-83, 2015.

[65] E. Van Uytven, T. Van Beek, P. M. McCowan, K. Chytyk-Praznik, P. B. Greer and B. M. C. McCurdy, “Validation of a method for in vivo 3D dose reconstruction for IMRT and VMAT treatments using on-treatment EPID images and a model-based forward-calculation algorithm”, Med. Phys., 42(12):6945-54, 2015.

[66] W. U. Laub and T. Wong, “The volume effect of detectors in the dosimetry of small fields used in IMRT”, Med. Phys., 30(3):341-347, 2003.

[67] E. Pappas, T. G. Maris, A. Papadakis, F. Zacharopoulou, J. Damilakis, N. Papanikolaou and N. Gourtsoyiannis, “Experimental determination of the effect of detector size on profile measurements in narrow photon beams”, Med. Phys., 33(10):3700–3710, 2006.

[68] L. Lin, M. Kang, T. D. Solberg, T. Mertens, C. Baumer, C. G. Ainsley and J. E. McDonough, "Use of a novel two-dimensional ionization chamber array for pencil beam scanning proton therapy beam quality assurance", J. Appl. Clin. Med. Phys., 16(3):5323, 2015.

[69] B. Poppe, T. S. Stelljes, H. K. Looe, N. Chofor, D. Harder and K. Willborn, "Performance parameters of a liquid filled ionization chamber array," Med. Phys., 40(8):082106, 2013.

[70] G. Wickman, "A liquid ionization chamber with high spatial resolution," Phys. Med. Biol., 19(1):66–72, 1974.

[71] E. Ching, S. Davis and J. Seuntjens, "Experimental analysis of general ion recombination in a liquid-filled ionization chamber in high-energy photon beams", Med. Phys., 40(6):062104, 2013.

[72] C. Knill, M. Snyder, J. T. Rakowski, L. Zhuang, M. Matuszak and J. Burmeister, "Investigating ion recombination effects in a liquid-filled ionization chamber array used for IMRT QA measurements", Med. Phys., 43(5):2476, 2016.

[73] A. Djouguela, I. Grießbach, D. Harder, R. Kollhoff, N. Chofor, A. Rühmann, K. Willborn and B. Poppe, "Dosimetric characteristics of an unshielded p-type Si diode: Linearity, photon energy dependence and spatial resolution", Z. Med. Phys., 18(4):301–306, 2008.

[74] P. A. Jursinic, "Dependence of diode sensitivity on the pulse rate of delivered radiation", Med. Phys., 40(2):021720, 2013.

[75] A. J. Scott, S. Kumar, A. E. Nahum and J. D. Fenwick, "Characterizing the influence of detector density on dosimeter response in non-equilibrium small photon fields", Phys. Med. Biol., 57(14):4461-76, 2012.

[76] A. H. Aldosari, A. Espinoza, D. Robinson, I. Fuduli, C. Porumb, S. Alshaikh, M. Carolan, M. L. F. Lerch, V. Perevertaylo, A. B. Rosenfeld and M. Petasecca,

"Characterization of an Innovative p-type Epitaxial Diode for Dosimetry in Modern External Beam Radiotherapy", IEEE Trans. on Nucl. Sc., 60(6):4705-12, 2013.

[77] IBA Dosimetry GmbH, "OmniPro I'mRT User's Guide", version 2.0. 2014.

[78] R. Boggula, M. Birkner, F. Lohr, V. Steil, F. Wenz and H. Wertz, "Evaluation of a 2D array for patient-specific VMAT QA with different setups", Phys. Med. Biol., 56(22): 7163-7177, 2011.

[79] J. E. Burns, "Conversion of PDD for photon beams from one SSD to another and calculation of TAR, TMR and TPR", BJR Suppl, 25:153-157, 1996.

[80] G. Narayanasamy, W. Cruz, N. Papanikolaou and S. Stathakis, "Comparison between measured tissue phantom ratio values and calculated from percent depth doses with and without peak scatter correction factor in a 6 MV beam", IJCTO, 3(2), 2015.

[81] R. Nath, P. J. Biggs, F. J. Bova, C. C. Ling, J. A. Purdy, J. van de Geijn and M. S. Weinhous, "AAPM code of practice for radiotherapy accelerators: report of AAPM Radiation Therapy Task Group No. 45", Med. Phys., 21(7):1093-121, 1994.

[82] J. L. Bedford, Y. K. Lee, P. Wai, C. P. South and A. P. Warrington, "Evaluation of the Delta^4 phantom for IMRT and VMAT verification", Phys. Med. Biol., 54(9):167-76, 2009.

[83] J. Kozelka, J. Robinson, B. Nelms, G. Zhang, D. Savitskij and V. Feygelman, "Optimizing the accuracy of a helical diode array dosimeter: a comprehensive calibration methodology coupled with a novel virtual inclinometer", Med. Phys., 38(9):5021-32, 2011.

[84] J. Sorriaux, A. Kacperek, S. Rossomme, J.A. Lee, D. Bertrand, S. Vynckier and E. Sterpin, "Evaluation of Gafchromic (R) EBT3 films characteristics in therapy photon, electron and proton beams", Phys. Med., 29(6):599-606, 2013.

[85] J.F. Mata-Colodro, A. Serna, V. Puchades-Puchades, D. Ramos-Amores, J.A. Vera-Sanchez and M. Alcaraz-Banos, "Multichannel film dosimetry vs 2D-array seven29 for vmat lung sbrt", Physica Medica, 32(3):246-247, 2016.

[86] M. Togno, J. J. Wilkens, D. Menichelli, M. Oechsner, A. Perez-Andujar and O. Morin, “Development and clinical evaluation of an ionization chamber array with 3.5 mm pixel pitch for quality assurance in advanced radiotherapy techniques”, Med. Phys., 43(5):2283-94, 2016.

[87] C. Courtois, G. Boissonnat, C. Brusasco, J. Colin, D. Cussol, J.M. Fontbonne, B. Marchand, T. Mertens, S. de Neuter and J. Peronnel, “Characterization and performances of a monitoring ionization chamber dedicated to IBA-universal irradiation head for Pencil Beam Scanning”, Nuclear Instruments and Methods, 736:112-117, 2014.

[88] N. Sahoo, X.R. Zhu, B. Arjomandy, G. Ciangaru, X. Ding and M. Gillin, “Feasibility Study of a Set of Quality Assurance Checks for Spot Scanning Proton Therapy Beams by using a 2-D Ion Chamber Array”, International Journal of Radiation Oncology, 75(3):698-699, 2009.

[89] C. Bäumer, B. Koska, J. Lambert, B. Timmermann, T. Mertens, P. T. Talla, “Evaluation of detectors for acquisition of pristine depth-dose curves in pencil beam scanning”, Journal of Applied Clinical Medical Physics, 16(6):151-163, 2015.

[90] T. Bortfeld, “An analytical approximation of the Bragg curve for therapeutic proton beams”, Med. Phys., 24(12):2024-33, 1998.

[91] M. Abramowitz and I. A. Stegun, “Handbook of Mathematical Functions”, National Bureau of Standards Applied Mathematics, Series 55, Dover, New York, 1972.

[92] K. Yasui, T. Toshito, C. Omachi, Y. Kibe, K. Hayashi, H. Shibata, K. Tanaka, E. Nikawa, K. Asai, A. Shimomura, H. Kinou, S. Isoyama, Y. Fujii, T. Akayanagi, S. Hirayama, Y. Nagamine, Y. Shibamoto, M. Komori and Jun-etsu Mizoe, “A patient-specific aperture system with an energy absorber for spot scanning proton beams: Verification for clinical application”, Med. Phys., 42(12):6999-7010, 2015.

[93] OCTAVIUS DETECTOR 1500 XDR, PTW particle therapy QA brochure (https://www.ptw.de).

[94] J. A. Gersh, S. Lovell and M. Deweese, “SU-E-T-125: High resolution linear diode array for use in stereotactic beam commissioning”, Med. Phys., 39(6):3731-3732, 2012.

[95] M. G. Bortolo and L. April, “Machine QC using omni-pro advance and StarTrack™”, Physica Medica, 31:S15, 2015.

[96] M. Togno, D. Menichelli, F. Friedl, reference number: WO2016102360 (A1)– RADIATION SENSOR, 2016-06-30.

List of Publications

PAPERS IN JOURNALS

First Author

M. Togno, J. J. Wilkens, D. Menichelli, M. Oechsner, A. Perez-Andujar and O. Morin, "Development and clinical evaluation of an ionization chamber array with 3.5 mm pixel pitch for quality assurance in advanced radiotherapy techniques", Med. Phys., 43(5):2283-94, 2016.

PAPERS IN BOOKS AND CONFERENCE ABSTRACTS

First Author

M. Togno, J. J. Wilkens and D. Menichelli, "SU-E-T-415: An ionization chamber array with high spatial resolution for external beam radiotherapy", Med. Phys., 41(6):321-321, 2014 (poster).

M. Togno, D. Menichelli, O. Morin, M. Oechsner and J. J. Wilkens, "PD-0443: Clinical evaluation of an innovative ionization chamber technology for patient quality assurance", Radiotherapy & Oncology, 115(1):216-217, 2015 (poster discussion young scientists).

M. Togno, A. Michaelidesova, D. Menichelli, J. J. Wilkens and V. Vondracek, "Characterization of a high resolution air filled ion chamber array technology for proton therapy QA", PTCOG 54 Annual Conference, 2015 (poster).

M. Togno, A. Michaelidesova, J. C. Celi, S. Marcelis, D. Menichelli, C. Vogel, J. J. Wilkens and V. Vondracek, "Characterization of novel solutions for daily QA and patient plan verification in pencil beam proton beams", MMND-ITRO Conference, 2016 (oral presentation).

Coauthor

L. Placidi, J. Hrbacek, M. Togno, A. J. Lomax and D. C. Weber, "Range resolution and reproducibility of a dedicated phantom for proton PBS daily quality assurance", submitted to Radiotherapy and Oncology (April, 2017).

PATENTS

M. Togno, D. Menichelli, F. Friedl, reference number: WO2016102360 (A1)–RADIATION SENSOR, 2016-06-30.

Acknowledgements

First of all, I would like to thank Prof. Dr. Jan Wilkens for giving me the opportunity to carry out my doctorate at the TUM, and for the continuous support from the beginning to the end of this personal objective. Thank you Jan for your patience, especially during the editing phase of this manuscript. I am also thankful to Prof. Dr. Pfeiffer for agreeing to be the second referee.

FROM THE FUNDING PROJECT *ARDENT* This work has been supported by the ARDENT Marie Curie ITN project, which gave me the opportunity to broaden my horizons beyond medical physics. I would like to thanks Dr. Marco Silari for the great coordination of the project, and the ARDENT crew for the inspiring time spent together. To the other 14 fellows, I wish the very best for their professional future.

FROM THE HOST INSTITUTE *IBA* I am very much indebted with my supervisor and colleague Dr. David Menichelli, for guiding me throughout the research work and for always being available for advice and consultation, despite his tight schedule. Without the perseverance of Dr. Juan Carlos Celi, most likely this manuscript would still be a draft. Thank you JC, also for giving me the opportunity to join IBA afterwards.

I also would like to thank Dr. Christian Vogel for the data on the 2D array and Friedrich Friedl for his valuable contribution in solving any question related to hardware.

Furthermore, I am thankful to all the people from the physics group for being great colleagues and friends, and for the support during the last year. You guys make the life at work nicer.

FROM THE PARTNER CLINICS I am thankful to Dr. Markus Oechsner from the Klinikum rechts der Isar, for giving me valuable insights on medical physics and for helping me in collecting part of the clinical data presented in this work. I am grateful to Dr. Olivier Morin for welcoming me to the UCSF and for the chats on the beautiful California, and to Dr.

Anna Michaelidesová and Dr. Vladimír Vondráček for the intensive measurement sessions at the PTC Prague.

FROM MICHELE'S WORLD My gratitude goes to all my 'old' friends, who are always a major source of support and fun despite the distances, and to all the people who became a significant part of my life during this journey. Among them, I thank Francesca for teaching me how beautiful a different point of view can be.

Last, but not least, I would like to thank my parents Marina and Mauro, my sister Silvia and my family for the continuous support to get me to this point, and Irene for always being able to smile even when the circumstances were tough.